Electrochemistry of Monolayer Mediated Redox-Active Species with Ultrafast Voltammetry

Md. Sazzad Hossain

Doctor of Philosophy

Mining and Materials Engineering

Faculty of Engineering
McGill University

Montreal, Quebec

October, 2017

A thesis submitted to McGill University in partial fulfilment of the requirements of the degree of Doctor of Philosophy

Acknowledgements

I begin by thanking *Allah*, the most gracious and the most merciful.

First and foremost, I would like to express my heartiest gratitude to my dear supervisor Professor Kirk H. Bevan. I consider myself very fortunate to have an amazing mentor in Professor Bevan from the very beginning of this journey, who guided and supported my development as a researcher with an extraordinary show of patience and kindness. He is a true inspiration for me to grow, and I could never ask for a better human being to learn from.

I would like to thank the Mining and Materials Engineering department and McGill University for providing a world-class environment and the facilities for graduate research.

I would also like to express my gratitude to Prof. Manuel Smeu and Dr. Vladimir Timoshevskii for their valuable guidance and brilliant support during my time as an intern at Institut de recherche d'Hydro-Qubec (IREQ). I would also like to thank Prof. Peter Grutter for valuable discussions on many occasions throughout this PhD.

I would like to thank in no particular order my group members Zi, Asif, Julien, Salvador, Shuaishuai and Botong for their support and feedback over the years.

Last but not the least, I am eternally grateful to my parents, who made their lifelong sacrifices to see me happy and successful. I thank my wife Nusrat, who has been on my side with her gracious support and encouragement.

Abstract

The work presents a theoretical framework to analyze and capture the role of energetics and electrochemical environment on electrochemistry of redox-active species in solution. The model system utilized in this study consists mainly of an ensemble of redox molecules/ nanoparticles in an aqueous solution each connected to a metal electrode by a bridging monolayer. In this configuration, redox processes are mostly outer-sphere in nature and are dictated by electron tunnelling across the metal-liquid interface. The transfer processes are simulated via voltammetry with a recently developed model based on quantum transport, which shows excellent agreement with the typically utilized Marcus-Gerischer rate picture in electrochemistry. Using this theory, a distinct connection between interfacial coupling and applied scan rate has been established. This connection reveals that by applying ultrafast scan rates, the active transfer rate can be forced to closely follow the ideal rate constants defined by the governing rate equations. This effectively leads to a significant suppression of electrode kinetics that broadens the resulting current peak towards infinity. Firstly, the peak potential of the derivative of this plateaued current response shows a good agreement with the effective redox-energy level of the reactants and the reorganization energy of the system. Secondly, the percent amount of redox conversions calculated from the current profiles at different scan rates show a consistent evolutionary pattern. This pattern is utilized to extract the effective coupling strength of the metal-monolayer-particle interface. This formulation is then implemented in a model redox system represented by armchair Carbon nanotubes to characterize its energy level structure near the Fermi level. In a solvated environment the key energetic contributions to such a level arise from the discrete electron-kinetic levels spacing $\delta\varepsilon_N^T$ and the Coulomb

charging energy U of a redox-species, and the nuclear reorganization energy λ of the overall system. Because of nuclear reorganization, a current peak in voltammetry that usually marks the access of an electron to a redox electronic level tends to occur at a potential that underestimates that electronic level. The proposed theory in this work presents a method to overcome this limitation by combining slow and ultrafast scan rates in voltammetry. The method correlates the resulting current-peak potentials to each of the above fundamental energetics consumed during the associated electron transfer. In slow scan rate regime, successive peak separations mainly represent the alternate consumption of $\delta\varepsilon_N^T + U$ and U. The influence of reorganization energy λ on a current profile is captured by ultrafast scan rates. Based on this formation, the technique is used to extract the electronic structure of the model armchair carbon nanotube system. Calculations at the ultrafast regime capture the inevitable interference from the non-faradaic charging current. Analyses show that nanoelectrodes should be preferred over planar electrodes to overcome this interference, as well as a highly mobile supporting ion system is required as an electrolyte to capture characterizable faradaic response. Since these energies have a universal presence in materials, the method is expected to be generally applicable in characterizing molecular and nanoparticle systems.

Résumé

Ce travail représente un cadre théorique pour l'analyse et la capture du rôle de l'environnement énergtique et électrochimique dans l'électrochimie des espèces redox actives en solution. Le système modèle utilisé dans ce projet consiste principalement d'un ensemble de molécules redox/ nanoparticules dans une solution aqueuse, connectées chacune à une électrode métallique par une monocouche faisant le pont. Dans cette configuration, les procédés redox sont majoritairement hors sphères dans la nature et sont dictés par la formation de tunnels par les électrons è travers l'interface métal-liquide. Les procédés de transfert sont simulés par voltamétrie a l'aide d'un modèle récemment développé basé sur le transport quantique. Ce modèle montre une excellente concordance avec le scenario de taux Marcus-Gerisher typiquement utilisé en électrochimie. Adoptant cette théorie, une connexion distincte entre le couplage interfaciale et la fréquence de balayage appliquée a été établie. Cette connexion révle qu'en appliquant une fréquence de balayage ultra rapide, le taux de transfert actif peut être forcé à suivre de près les constantes de fréquence idéale définies par les équations de fréquence gouvernantes. Ceci abouti efficacement à une suppression significative des cinétiques d?électrode qui élargissent vers l'infini les pics de courant résultants. Premièrement, le potentiel du pic de la dérivée correspondant à la réponse du courant plateau montre une bonne concordance avec le niveau d'énergie redox effective des réactifs ainsi qu'avec l'énergie de réorganisation du système. Deuxièmement, le pourcentage du nombre de réactions redox calculé à partir du profil de courant pour différentes fréquences de balayage montre un modèle évolutif consistant. Ce modèle est utilisé pour extraire la force de couplage effective de l'interface métal-monocouche-particule. Cette formulation est ensuite implémente dans un système de modèle redox représenté par des nanotubes

de carbone de type fauteuil afin de caractériser sa structure de niveau d'énergie au voisinage du niveau de Fermi. Dans un environnement solvaté, les contributions énergétiques clés à un tel niveau sont dues à l'espacement des niveaux d'électron discret- cinétique $\delta\varepsilon_N^T$ et Columb l'énergie de charge U des espèces redox, ainsi qu'à l'énergie de réorganisation nucléaire λ de tout le système. A cause de la réorganisation nucléaire, un pic de courant en voltamétrie qui marque généralement l'accès d'un électron à un niveau électronique redox, tend à se produire à un potentiel qui sous-estime ce niveau électronique. La théorie proposée dans ce travail présente une méthode pour surmonter cette limitation en combinant des fréquences de balayage lente et ultrarapide en voltamétrie. La méthode corrèle les potentiels pics-courant à chacune des énergétiques fondamentales, déj abordées, consommées durant le transfert d'électrons associé. Dans un régime de lentes fréquences de balayage, les séparations de pics successives représentent principalement la consommation alternative de $\delta\varepsilon_N^T + U$ et U. L'influence de l'énergie de réorganisation λ sur le profil de courant est capturée par des fréquences de balayages ultra rapides. En se basant sur cette information, la technique est utilisée pour extraire la structure électronique du système du modle de nanotube de carbone de type fauteuil. Les calculs en régime ultrarapide capturent l'inévitable interférence provenant du courant de charge non-faradique. Les analyses montrent que les nanoélectrodes devraient être préfrées au électrodes planaires pour surmonter cette interférence, et un systéme d'ion support à haute mobilité est requis comme électrolyte pour capturer une réponse faradique caractérisable. Etant donné que ces énergies ont une présence universelle dans les matériaux, cette méthode devrait être appliquée généralement dans la caractérisation des systèmes moléculaires et de nanoparticules.

Table of Contents

List of Figures

List of Symbols

$[H]$	Hamiltonian matrix
$[S]$	overlapping matrix
α	normalized scan rate
α_{tc}	heterogenous transfer coefficient
$\delta\varepsilon^T$	molecular energy level spacing, eV
$\Delta G_b^{\ddagger}$	activation energy for backward/oxidation step, eV
$\Delta G_f^{\ddagger}$	activation energy for forward/reduction step, eV
$\Delta G_{0a}^{\ddagger}$	activation energy of oxidation in heterogenous process, eV
$\Delta G_{0c}^{\ddagger}$	activation energy of reduction in heterogenous process, eV
$\Delta G_a^{\ddagger}$	required energy for oxidation under overpotential in heterogenous process, eV
$\Delta G_c^{\ddagger}$	required energy for reduction under overpotential in heterogenous process, eV
δt	length of time step, s
δ	monolayer length, nm
$\Delta\phi_p$	excess potential dropped in solution due to planar electrode, V
$\Delta\phi_s$	excess potential dropped in solution due to spherical electorde, V
ϵ_0	permittivity of vacuum, F/m
ϵ_∞	optical dielectric constant
ϵ_r	dielectric constant of solution
ϵ_s	static dielectric constant
η	overpotential, V
η_P	peak potential in a current profile, V
η_{max}	maximum overpotential, V
η_{peak}	peak potential, V
η_{step}	size of a single overpotential step, V
Γ_R	reactant broadening matrix
Γ_S	product broadening matrix
$\hbar$	reduced Planck's constant, $eV \cdot s$
κ	homogenous transmission coefficient
λ	reorganization energy, eV
λ_i	inner reorganization energy, eV

λ_o	outer reorganization energy, eV
$\|M\|$	electronic coupling, $eV/\sqrt{s}$
$\mathcal{A}$	frequency factor in transfer attempt, $1/s$
$\mathcal{C}_{edl}$	capacitance of electric double layer, F
$\mathcal{N}$	number of atoms
$\mathcal{R}_{si}$	resistance of solution, Ω
$\mathcal{T}$	temperature, K
$\mathtt{E}$	total energy, eV
μ_{eq}	equilibrium electrochemical potential, V
ϕ	potential distribution across system, V
Σ_R	Green's function self-energy for reactants
Σ_S	Green's function self-energy for substrate
τ_R	reactant-monolayer coupling, eV
τ_S	substrate-monolayer coupling, eV
τ_p	planar RC time constant, s
τ_s	spherical RC time constant, s
θ	reactant occupation factor
ε	energy, eV
ε^T	quantized electron kinetic levels, eV
ε_F	fermi level, eV
ε_N	single particle energy, eV
ε_N^T	N^{th} molecular energy level, eV
ε_{ox}	oxidized energy level, eV
ε_{red}	reduced energy level, eV
ξ_z	integer index to define nanotube length
A_b	proportionality constant in heterogenous oxidation rate, $1/s$
A_f	proportionality constant in heterogenous reduction rate, $1/s$
A_R	reactant spectral function
A_S	substrate spectral function
b	width of a single armchair nanoring, nm
C^+	concentration of positive supporting ions in solution, $1/cm^3$
C^-	concentration of negative supporting ions in solution, $1/cm^3$
C_N^{acc}	acceptor state concentration awaiting arrival of N^{th} electron, $1/cm^2$
C_N^{don}	donor state concentration ready to donate N^{th} electron, $1/cm^2$
C_{ox}	concentration of oxidized reactants, $1/cm^2$
C_{ox}^*	equilibrium concentration of oxidized reactants, $1/cm^2$
C_{red}	concentration of reduced reactants, $1/cm^2$
C_{red}^*	equilibrium concentration of reduced reactants, $1/cm^2$
d	separation between neighbouring packing layers, nm
D^+	diffusivity of positive supporting ions in solution, cm^2/s
D^-	diffusivity of negative supporting ions in solution, cm^2/s

D^{acc}	probability of acceptor/absorption states, $1/eV$
D_N^{acc}	probability of N^{th} acceptor/absorption states, $1/eV$
D^{don}	probability of donor/emission states, $1/eV$
D_N^{don}	probability of N^{th} donor/emission states, $1/eV$
D_R	reactant density of states, $1/eV$
D_S	density of electrode states, $1/eV$
d_{mr}	distance from electrode surface into solution, nm
D_{ox}	Gerischer's density of oxidized states, $1/eV$
D_{red}	Gerischer's density of reduced states, $1/eV$
E_A	activation energy in homogenous reaction
f	Fermi distribution
G	partitioned Green's function
G^n	monolayer electron correlation function
h	Planck's constant, $eV \cdot s$
j	current density (general), A/cm^2
J_N^{acc}	acceptor diffusion current (N^{th} electron state), A/cm^2
J_{C^+}	ionic current density of positive supporting ions, A/cm^2
J_{C^-}	ionic current density of negative supporting ions, A/cm^2
j_c	charging current density, A/cm^2
j_{et}	faradaic current density, A/cm^2
k^0	standard rate constant, $1/s$
k_B	Boltzmann constant, eV/K
k_b	rate of heterogenous oxidation, $1/s$
k_f	rate of heterogenous reduction, $1/s$
$k_{b,hm}$	rate of backward transfer in homogenous reaction $1/s$
$k_{f,hm}$	rate of forward transfer in homogenous reaction, $1/s$
k_{hm}	homogenous rate constant (general), $1/s$
k_{max}	maximum rate, $1/s$
k_{ox}	same as k_b, the rate of oxidation, $1/s$
k_{red}	same as k_f, the rate of reduction, $1/s$
L	nanotube length, nm
m	EDL active layer index
N	occupation number of electrons
n	concentration of electrons, $1/cm^3$
n_i	phenomenological concentration of electrons in metal, $1/cm^3$
n_f	concentration of localized electronic charge in solution, $1/cm^2$
N_{ic}	concentration of metal-ion cores, $1/cm^3$
N_{ox}	concentration of electrons transferred from redox group, $1/cm^2$
N_{red}	concentration of electrons transferred to redox group, $1/cm^2$
q	charge of electron, C
q_P	minimum energy coordinate for reduced reactant, Å(only in this work)

q_R	minimum energy coordinate for oxidized reactant, Å(only in this work)
R	applied scan rate, V/s
R	nanotube radius, nm
r	distance of ion from spherical surface, nm
r_0	radius of spherical electrode, nm
r_s	radius of electroactive molecules, nm
R_{ult}	ultimate scan rate, V/s
T	transmission probability
t	time, s
T_e	kinetic energy of electrons, eV
t_{min}	shortest time required for electron transfer, s
t_{scan}	time period for scanning, s
U	single-electron Coulomb charging energy, eV
u^+	mobility of positive supporting ions in solution, cm^2/s
u^-	mobility of negative supporting ions in solution, cm^2/s
U_∞	Coulomb charging energy due to fast polarization, eV
$U_{\mathcal{NN}}$	nuclear-nuclear interaction energy, eV
$U_{e\mathcal{N}}$	electron-nuclear interaction energy, eV
U_{ee}	electron-electron interaction energy, eV
U_s	Coulomb charging energy of spherical particles, eV
x	defines a point along the length of a nanotube, nm

Contribution of Authors

The work presented in this thesis has been published in the following journals. The discussion in Chapter 3, 4 and 5 have been reproduced from these publications.

- Hossain, M. S., Bevan, K. H., Exploring Bridges between Quantum Transport and Electrochemistry. II. A Theoretical Study of Redox-Active Monolayers, *J. Phys. Chem. C*, 2016, 120, 188–194.
- Hossain, M. S., Iqbal, A., Bevan, K. H., Interfacial Screening in Ultrafast Voltammetry: A Theoretical Study of Redox-Active Monolayers, *Anal. Chem.*, 2016, 88, 9062–9070
- Hossain, M. S., Muralidharan, B., Bevan, K. H., A General Theoretical Framework for Characterizing Solvated Electronic Structure via Voltammetry: Applied to Carbon Nanotubes, *J. Phys. Chem. C*, 2017, 121, 18288–18298.

In the first work, the simulations were performed by M. S. Hossain with guidance and supervision from K. H. Bevan. Both authors contributed to the writing of the paper.

In the second work, the simulations were performed by M. S. Hossain, A. Iqbal assisted in coding. The work was guided and supervised by K. H. Bevan. All authors contributed to the writing of the paper.

In the third paper, the simulations were performed by M. S. Hossain. B. Muralidharan provided guidance on implementing Coulomb blockade to electron transfer in calculations. The project was further guided and supervised by K. H. Bevan. All authors contributed to the writing of the paper.

Original Contribution to Knowledge

The work performed in this thesis makes several key contributions in the fields of physical and analytical electrochemistry.

Firstly, The work presents a technique to identify an electroactive redox energy level in solution and the coupling strength of an electrochemical interface using voltammetric methods. Typical current responses in voltammetry show a remarkable reaction-kinetic dependence, which sever any identifiable correlation between a redox level and the resulting potential of a current peak. The first part of this study shows that this kinetic dependence can be suppressed by applying ultrafast scan rates. It is this regime of kinetic independence where an active redox level is likely to reveal its energetic structure directly in a voltammetric current plot. In addition to a detailed formulation of this technique, the work further predicts a possible pattern in the percentage amount of reactant conversion at different scan rates. This pattern lays an easy path to derive the coupling strength of an interface during redox processes.

Following these formulations, the work then develops an elaborate correlation among the various non-faradaic factors that accompany a redox process. These factors are mostly based upon the transport of supporting ions in a solution and include charging current, interfacial screening, formation of double layer and the extent of electrode surface coverage by monolayer bridges. The work shows that in the ultrafast scanning regime, the required interfacial screening in order to extract an analyzable faradaic response would require nanoelectrodes and the presence of highly mobile supporting ion system such as the aqueous solution of NaCl etc. The nanoelectrode is aimed to induce radial diffusion of supporting ions for faster screening. Moreover, counter intuitive to our current understanding, the calculations predict that the time dependent interfacial screening can be faster if the

monolayer coverage on electrode surface is increased, given that the bridging monolayer is longer than $\sim$1 nm.

Finally, this work proposes an electrochemical technique based on voltammetry to characterize the electronic structure of a solvated molecular/nanoparticle system. The technique connects some specific properties of voltamemtric current *i.e.* peak potential and width at various scan rates to electron-kinetic energy, Coulomb charging energy and nuclear reorganization energy. Using this connection, the work shows that one may be able to extract the electronic levels near the Fermi level of a solvated redox-active species. During this development, the study revealed that contributions of both electron-kinetic energy and Coulomb charging energy to the total energy required for an electron transfer have equivalent quantitative significance at all dimensions of a solvated nanoparticle. In contrast, presently these two contributions define electron transfer in a rather distinct redox charging at molecular length-scales and Coulomb charging regime at larger, nanoparticle dimensions.

CHAPTER 1
Introduction

The field of molecular transport has drawn significant attention since its birth in the early 70's. Current researches in many scientific and engineering disciplines, especially those devoted in the fields of electronics engineering and medical sciences are effectively laying the foundation for a molecular future. This upsurge of interest in molecule based systems can partly be attributed to their ability to demonstrate a broad range of electronic conductivity in interfacial transport processes. Implementation of molecular entities has enormous versatility across different systems. We see molecules functioning as electroactive redox groups, which can charge and discharge electrons in a storage device, as found in organic radical batteries and devices.[20] We find molecules or nanoparticles of larger dimension such as Carbon nanotubes being functionalized by smaller redox groups that only serve to donate or withdraw electrons to or from the larger species.[28,29] Such modifications impact the electronic structure and therefore the conductivity of the larger base molecule/nanoparticle. With the advent of self-assembled monolayers, molecular species are now being regularly incorporated as a bridge to facilitate electron tunnelling between a metal and a redox group. Depending on the chemical nature, these molecular bridges can provide an excellent control over the extent of interfacial conduction.

These features draw an exciting prospect regarding the appeal of redox-molecular systems. A number of major technological interests in today world such as batteries, semiconductors, optoelectronics, sensors etc are being heavily investigated on various molecular

platform. One may wonder about the specific advantages that a molecule based system may offer. To address this, we can closely examine the recent developments in organic radical batteries (ORB) having a radical-molecule based cathode system with respect to the currently popular $LiFePO_4$ and other transition metal based cathodes. $LiFePO_4$ and other cathodes in this class based on Mn, Ni etc offer a high energy density.[30,31] However, because of high band gap of these materials, they tend to be poor conductors and thus have intrinsically low power densities. A partial solution comes from carbon coating of these particles to ease electron transport within the cathode terminal. Organic radical batteries (ORB) at its current state lag behind these technologies on energy density, primarily due to the loose and flexible nature of assembly of an ensemble of molecules. However, they have significantly higher power densities which is an important requirement in the batteries intended for electric vehicles. This high power density in ORBs arise from their faster electron transfer rates by several orders of magnitudes than that in the present $LiFePO_4$ cathode systems.[32,33] In addition to these high and low points, cost of fabrication is a major challenge towards implementing this technology. A hybrid $LiFePO_4$–ORB battery has been proposed to combine the individual superiority in energy and power densities of the two phases.[32,34] The exciting potentials of molecular devices will continue to drive the advances in this field, and only time will tell whether molecular systems can be implemented in a mass scale for everyday applications.

It is common to find electron transfer in molecule based system *e.g.* self-assembled monolayers (SAM) taking place via outer-sphere interaction between donor and acceptor states. The theories in this transfer regime are well developed as opposed to the more complicated realm of inner-sphere interactions. This can be attributed partly to the certainty of pinpointing the position of an electron either on a metal-state or on a redox-state across the interface during an outer-sphere reaction. In an inner-sphere process however,

it is challenging to locate an electrons' position as it is shared by both states across an interface. Chemisorption of an element on a metal surface during an electrocatalytic process is an example of an inner-sphere interaction. In this work, the studied interactions were limited within the outer-sphere regime. In developing such a system, a major point of consideration is the selection of redox groups and the associated monolayer bridge. The geometry and the electronic structure of a redox group primarily decide the energetic cost of an electron transfer. The monolayer usually provides coupling that tells how fast electrons can tunnel. It is therefore, easy to see that characterization of these components are integral steps in device design.

A major challenge arises when a metal-monolayer-redox group configuration is exposed into an electrolyte solution. A solution typically enforces major modifications to the electronic structure of redox reactants, which gives rise to an apparent independence of electrochemical response to the associated redox-active energy level. In other words, isolated (non-solvated) characterization of various electroactive components *i.e.* redox-group and monolayer bridge are not likely to allow a straightforward correlation to the ultimate faradaic response. To obtain a better and sensible connection, it would therefore be more appropriate to perform in-situ characterization of the above mentioned configuration in the presence of a solution. Here, the key components from a solvent that enter into the transfer picture are charging and potential screening at an interface via ionic transport in solution.

In this work, these major electrochemical components in a "metal-monolayer-redox reactant" system have been combined into a single framework within the outer-sphere regime of interaction, which allows in-situ characterization of system energetics under solvated conditions. In this framework, first a comprehensive analysis of faradaic processes has been performed to understand the relation between an electrochemical current and

the associated redox energetics. The analysis reveals that the strength of electrode kinetics that typically dictates the properties of a voltammetric current can be controlled by faster overpotential scanning. Under the ultra/fast-scan regime, majority of electron transfers are forced to occur at an ideal rate defined by a governing equation such as the Marcus-Gerischer formulation[1] that has been adopted in this work. The structure of such a current response shows a direct agreement to the participating redox-active level and the reorganization energy in solution. This study is followed by a detailed evaluation and the subsequent incorporation of the impact of supporting ions on electron transfer in the presence of a solution. Primary attention was given to interfacial screening which is critical at ultrafast scan regime and may require fast mobile ions. The evolution of screening in time and overpotential shows that monolayer mediated systems are capable of undergoing faster potential screening than that with a less populated (by monolayers) electrode surface. This invokes the possibility of reaching faster scan rates in voltammetry.

Finally, this picture has been implemented in a model solvated electrochemical system to extract the various energetic components of its redox-active levels with linear sweep voltammetry. The model system was represented by the semiconducting lengths of an armchair nanotube. In this regard, the position and structure of redox levels in energy have been constructed with contributions from electron-kinetic energy (via solution of Schrodinger's equation) ε_N^T, Coulomb charging energy for the addition or removal of a single electron U and the total reorganization energy λ of the system. The description represents an equitable contribution of both ε_N^T and U to a redox-level position at all dimensions of a nanoparticle. The solvated-energy-level structure has then been combined with the Marcus-Gerischer rate picture to simulate multiple electron transfer voltammetry. The resulting current profiles generated from a combination of slow and ultrafast scan rates show a good agreement with the constructed redox-energy-level picture. Based on

this agreement, a detailed formulation has been presented to extract ε_N^T, U and λ. We show that these energies can be extracted for electron's access into successive redox levels. From an experimental point of view, extraction of these successive levels using voltammetry can lead to the electronic structure of nanomaterials near the Fermi level. Based on the wide and easy accessibility of voltammetric techniques, the suggested characterization method can be a useful compliment to more sophisticated spectroscopic techniques.

CHAPTER 2
Literature Review

2.1 Charge Transfer

Charge transfer refers to an electronic transition event from a donor species to another acceptor species. A donor-acceptor couple can both be a part of a single-phase environment where transition from one charged state to another can occur uniformly across the system. Such transition events are classified as homogenous electron transfer (ET). A well understood reaction in this category is the transfer of electron between Fe^{3+} (acceptor) and Fe^{2+} (donor) couple in an electrolyte. Combustion of gaseous hydrocarbons in the presence of air to produce flame is an example of homogenous electron transfer reaction that we encounter in our daily life. The digestive mechanism in human body is heavily based on ET processes during homogenous oxidation of ingested food that produces the energy we need to run and sustain our various organisms. While the media surrounding a donor and a receiver state is uniform in such homogenous processes, it is also very common for an electron to make a transition between two redox-active states across an interface between two phases. This type of transitions are classified as heterogenous or interfacial transfer processes which are observed in significant majority of electronic devices and energy-storage systems as well as in many biological processes and applications. Portable devices are powered by both primary and rechargeable batteries on a daily basis where chemical energy of a redox reaction is transformed into electrical energy at an electrode-electrolyte interface. Rust formation on metal surfaces is another familiar instance of heterogenous electron transfer,

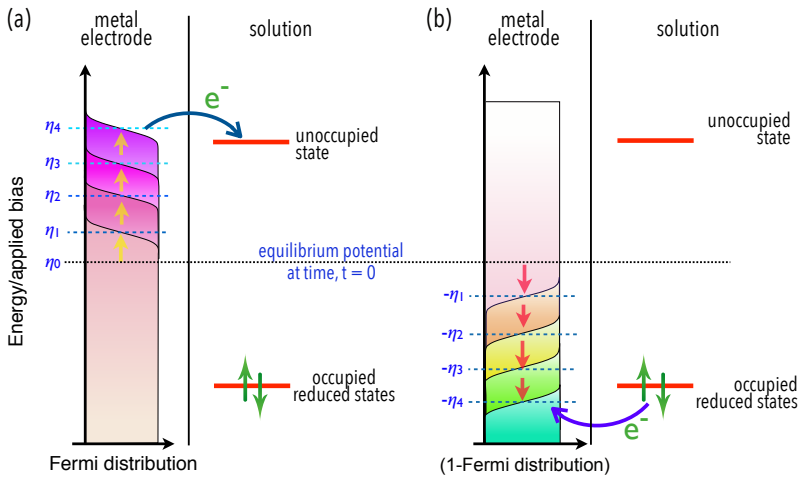

Figure 2.1: Electron transfer between delocalized electronic states in metal and localized molecular states in solution across the interface. A reduction transfer (a) only takes place when the energy of electrons in metal is raised from equilibrium (η_0) to equal or higher than the energy of the unoccupied state in solution, *i.e.* $\sim \eta_4$. Similarly, the energy needs to be lowered to $\sim -\eta_4$ in electrode to oxidize from an occupied state (b).

where metal ions at the surface of Iron are oxidized in the presence of water molecules in the environment. From a technological perspective, heterogenous processes carry great significance as they determine the efficiency of current flow in many device systems. Maximization of efficiency in such systems in terms of current and energy output depends on our ability to understand and engineer the structure and energetics of interface between two phases. Therefore, it becomes essential for us to correlate charge transfer with the various interfacial characteristics.

When dealing with heterogenous ET, one starts by looking into the active energy levels of donor and acceptor states across an interface. In solid state systems such as a *p*-*n* diode or a metal-semiconductor junction, these electronic levels represent the respective delocalized sea of conducting states on either side of interface. The delocalized states allow electrons to flow through the device across that interface to generate current flow. In contrast, high electron mobility in a solid-liquid configuration is usually limited inside

the solid phase only, since an electron is likely to localize on a redox molecular state upon making the transition into the liquid phase, as shown in Figure 2.1. In these cases, the gain in current/energy becomes limited by the rate at which electrons can make the transition across that interface. Building a comprehensive rate picture is thus a key to understanding the output from electrochemical events. There are several factors that typically control the rate of electron transfer. For example, it depends on the electronic structure of the metal-electrolyte interface, which tells us the relative energetics of donor and acceptor states and the associated energy requirements for a successful ET. The transfer process further relies upon the extent of electronic coupling between a donor-acceptor couple across their interface, which quadratically influences the transfer rate. Then one needs to consider how concentration of electroactive species evolve under nonequilibrium conditions and their mobility in solvent/electrolyte; both of which are important determinants in the overall electrochemical kinetics. While typical electrochemical systems represent a solid-liquid interface, fully solid state configurations implemented for batteries have been reported with interesting transport characteristics.[35]

2.1.1 Kinetics

It is well known that as potential is applied to an electrode to induce an electron transfer to/from a localized state in a molecular species in electrolyte, the rate of transfer as a response is significant only around a given potential, while it is negligible in the others (as suggested in Figure 2.1). Energetic position of an electroactive molecular level directly involved in such a transfer process depends firstly on the chemical and geometric makeup of the molecule/particle itself. Secondly, it depends on the extent of structural reorganization of both redox reactant and the surrounding electrolyte environment in response to a change in the number of localized charge upon the loss or gain of an electron. The energy levels

structure of a molecule/particle participating in an exchange processes remain fixed in a given electrolyte. However, it is quite challenging to correlate the exchange overpotential with the participating energy level. On the course to establish this connection, this review discusses and analyses some key background theories. These theories lay a foundation for the work done in this thesis that would hopefully advance the current state of nanoparticle/molecular electrochemistry. Before heading into heterogenous kinetics, which is the focus of this work we begin with a short discussion of a homogenous transfer scenario as it would provide some useful basis towards the understanding of electron transfer.

2.1.2 Homogeneous kinetics

Arrhenius was the first to recognize the generality in the variation of rate constants with temperature in most solution-phase charge transfer reactions, which gives us the expression for homogeneous rate constant in the following form

$$k_{hm} = \mathcal{A}\ exp(-E_A/k_B\mathcal{T}) \tag{2.1}$$

where, E_A is the activation energy barrier in electron-volts (eV) that an electron must overcome to make a transition from an initial state to the final state. The exponential term here expresses the probability of making this transition using thermal energy from the surrounding environment, which is given by $k_B\mathcal{T}$, where $\mathcal{T}$ is the temperature in Kelvin (K) and k_B is Boltzmann constant in eV/K. The pre-exponential term $\mathcal{A}$ is known as the frequency factor relating to the number of attempts made per second towards making a transition. While the expression itself turned out to be an oversimplification of a much complicated rate picture, the idea of activation energy emerged to be very useful and important ever since in the study of charge transfer.

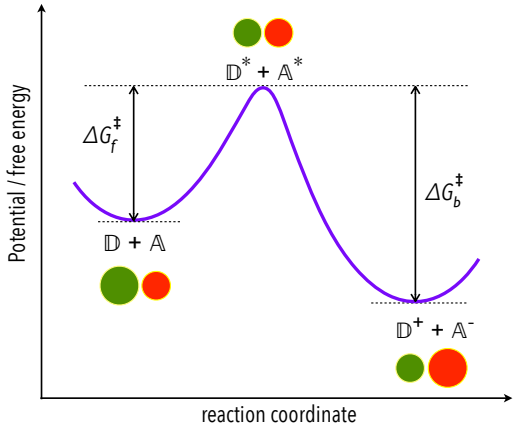

Figure 2.2: Homogenous transfer with a transition state. Forward and backward processes pass through an activated complex where reactant and product share their active electron and thus have a common, intermediate molecular structure.

An important consequence of the activation energy picture is the emergence of *reaction path* in terms of variation in potential energy along a reaction coordinate. This coordinate depicts progress of reaction along a favoured path on a multidimensional potential energy surface that represents the structural/geometric changes of electroactive species on the course of loosing or accepting an electron. To visualize this picture, we consider a simple homogeneous reaction between a donor and an acceptor couple $\mathbb{D}$ and $\mathbb{A}$ respectively, between which a single electron exchange can be described via $\mathbb{D} + \mathbb{A} \longleftrightarrow \mathbb{D}^* + \mathbb{A}^* \longleftrightarrow \mathbb{D}^+ + \mathbb{A}^-$. In this reaction, $\mathbb{D}$ donates its electron and becomes $\mathbb{D}^+$ whereas $\mathbb{A}$ takes the electron to become $\mathbb{A}^-$. Figure 2.2 illustrates a schematic of the reaction path for this exchange process. The two wells on this path represent the reaction coordinates and the associated energies before (reactant) and after (product) the electron transfer. The coordinate may represent geometric parameters such as the twist angle between a central bond, or just the bond length. To understand a reaction through this representation, let us simplify the coordinate system such that it only describes the bond length of a molecule. The two minima in energy on this profile thus correspond to the equilibrium bond lengths in

the respective reactant and product states, shown by the representative spheres in Figure 2.2. The equilibrium bond lengths of the reactant states $\mathbb{D}$ and $\mathbb{A}$ oscillate around the reactant minimum (on the left) along the energy surface due to thermal energy $k_B\mathcal{T}$ in solution. With sufficient energy, the bond can stretch to an extent such that the energy of reactant couple $\mathbb{D} + \mathbb{A}$ reaches the maximum in the path (shown by two equal spheres in the middle). This maximum defines an excited state for the reactant couple $\mathbb{D}^* + \mathbb{A}^*$ where the electron can swing back and forth between $\mathbb{D}$ and $\mathbb{A}$. From this stage, there is a finite probability that the excited couple may slide down into the product realm of the reaction path (to the right) and eventually settle into the new minima for the $\mathbb{D}^+ + \mathbb{A}^-$ couple with a new bond configuration. Assuming it to be the forward process, the rate of this transition can be written as[1]

$$k_{f,hm} = \kappa \frac{k_B\mathcal{T}}{h}\ exp(-\Delta G_f^{\ddagger}/k_B\mathcal{T}) \tag{2.2}$$

where $\Delta G_f^{\ddagger}$ is the standard free energy change in going from the reactants $\mathbb{D} + \mathbb{A}$ to the activated complex $\mathbb{D}^* + \mathbb{A}^*$. The prefactor contains the coefficient of transmission, κ capable of taking values between 0 and 1, which couples with $k_B\mathcal{T}/h$ to give the frequency of attempt towards a successful transition. Similarly, we can express the rate of backward process to capture the transition $\mathbb{D} + \mathbb{A} \longleftarrow \mathbb{D}^+ + \mathbb{A}^-$ as

$$k_{b,hm} = \kappa \frac{k_B\mathcal{T}}{h}\ exp(-\Delta G_b^{\ddagger}/k_B\mathcal{T}) \tag{2.3}$$

Just as before, $\Delta G_b^{\ddagger}$ here is the standard free energy for the transition $\mathbb{D}^* + \mathbb{A}^* \longleftarrow \mathbb{D}^+ + \mathbb{A}^-$. This first order expression is expanded in practice to include reactant concentrations to capture electrochemical processes away from equilibrium. Central to this concept is the idea that these processes pass through a transition state with the formation of an activated complex ($\mathbb{D}^* + \mathbb{A}^*$). The more advanced Marcus picture however suggests that the reactants

retain their individual structure during the transition.

2.1.3 Heterogeneous kinetics: electrode reactions

The potential energy picture can be a useful way to view and understand heterogeneous processes as well. We will return to this picture shortly with classical and more sophisticated microscopic theories of ET processes. Let us begin here by discussing the general aspects of electrode kinetics. It is well known that implementing a kinetic formulation into the analysis of interfacial processes requires a representative theory to satisfy two fundamental conditions:[1] firstly, electrode kinetics must reduce to thermodynamic equilibrium via satisfying Nernst equation, which connects electrode potential/energy (ε) to bulk reactant concentrations; and secondly, the theory must explain Tafel behaviour which predicts exponential rise of electrode current at small overpotentials. Based on this premise, an electrode process can mainly be characterized with two key components. First, a *rate constant* which captures the characteristics of ET across an interface. This will be discussed in detail across later sections of this review. The second component is the *concentrations of electroactive redox species* and their evolution at and near the electrode surface. Combining the two gives the basic framework for building the rate of or current due to ET between an electrode and an active redox species in a heterogeneous process. This review will highlight the key aspects of this connection to present a strong understanding of the electrochemistry.

Let us begin by analyzing a classical perspective of a single electron transfer in a simple redox reaction

$$Ox + e \rightleftharpoons Red$$

using the potential energy surface representation. This approach leads to the classical Butler-Volmer formulation for ET. Just as in Figure 2.2 for a homogeneous case, the changes

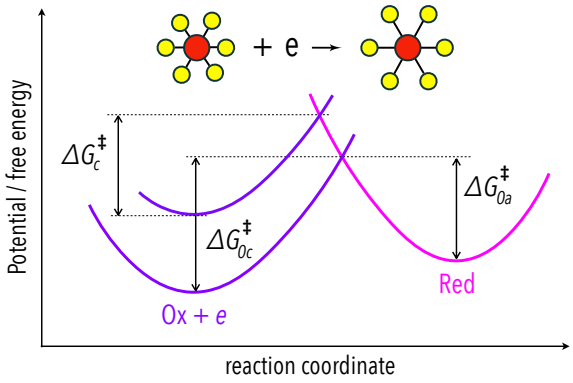

Figure 2.3: Heterogeneous transfer processes via reactant and product energy surfaces representation.[1]

in the geometric structure of the oxidized (Ox) and the reduced (Red) reactants along a heterogenous reaction are captured by the characteristics of their potential energy surfaces shown in Figure 2.3. Here again, we take bond lengths of reactants as the representative metric for the reaction coordinate. Unlike the homogeneous case, here the surface regarding $Ox + e$ in Figure 2.3 includes the energy of both oxidized reactant and electrons in metal electrode. Under equilibrium conditions, the activation energy for reduction ($Ox + e \rightarrow Red$) is given by $\Delta G_{0c}^{\ddagger}$. Similarly, the oxidation process ($Ox + e \leftarrow Red$) has an activation energy equal to $\Delta G_{0a}^{\ddagger}$. At this state, applying an overpotential η would change the energy of the electrons in electrode which raises or lowers the $Ox + e$ surface with respect to its equilibrium position. This is shown in Figure 2.3, where it was assumed that a positive overpotential changes electron energy in such a way that the $Ox + e$ surface shifts in an upward direction. This consequently, leads to a lowering in the activation energy for the cathodic process ($Ox + e \rightarrow Red$) from $\Delta G_{0c}^{\ddagger}$ to $\Delta G_c^{\ddagger}$. The non-equilibrium energy $\Delta G_c^{\ddagger}$ can be related to the equilibrium characteristics with $\Delta G_{0c}^{\ddagger}$ via[1]

$$\Delta G_c^{\ddagger} = \Delta G_{0c}^{\ddagger} + \alpha_{tc}\ q\ \eta \tag{2.4}$$

where α_{tc} is the transfer coefficient capable to taking values ranging between zero and unity, q is the charge of an electron. The value of transfer coefficient α_{tc} depends on the angle of intersection between the oxidized and reduced reactant energy surfaces. Therefore, the shapes of these surfaces determine the activation energy needed to transfer an electron. The activation energies for anodic processes ($Ox + e \leftarrow Red$) can be connected in the same way

$$\Delta G_a^{\ddagger} = \Delta G_{0a}^{\ddagger} - (1 - \alpha_{tc})\ q\ \eta \tag{2.5}$$

where $\Delta G_a^{\ddagger}$ and $\Delta G_{0a}^{\ddagger}$ are the activation energies for transferring an electron back from redox-species to electrode with and without (equilibrium) an applied overpotential η, respectively. The activation energies dictate the probability of a transfer event which gives rise to the rate constants[1] for the forward ($Ox + e \rightarrow Red$) and backward ($Ox + e \leftarrow Red$) processes in the form of

$$k_{f,het} = A_f\ exp(-\Delta G_c^{\ddagger}/k_B\mathcal{T}) = A_f\ exp(-\Delta G_{0c}^{\ddagger}/k_B\mathcal{T})\ exp(-q\alpha_{tc}\eta/k_B\mathcal{T}) \tag{2.6}$$

$$k_{b,het} = A_b\ exp(-\Delta G_a^{\ddagger}/k_B\mathcal{T}) = A_b\ exp(-\Delta G_{0a}^{\ddagger}/k_B\mathcal{T})\ exp(q(1-\alpha_{tc})\eta/k_B\mathcal{T}), \tag{2.7}$$

respectively. A_f and A_b are proportionality constants. Considering the interface to be under equilibrium at zero overpotential ($\eta = 0$), one can expect equal current flow due to reduction and oxidation processes via $k_{f,het} \times C_{ox}^{*} = k_{b,het} \times C_{red}^{*}$, where C_{ox}^{*} and C_{red}^{*} are the equilibrium concentration of oxidized and reduced species, respectively. This situation at $\eta = 0$ gives rise to the standard rate constant k^0 which leads to the rate expressions

$$k_f \equiv k_{f,het} = k^0 exp(-q\alpha_{tc}\eta/k_B\mathcal{T})$$

$$k_b \equiv k_{b,het} = k^0 exp(q(1-\alpha_{tc})\eta/k_B\mathcal{T}).$$

Since, we will mostly be dealing with heterogenous processes in this discussion, we drop the "*het*" subscript from the above heterogenous rate definition. From here onwards, only

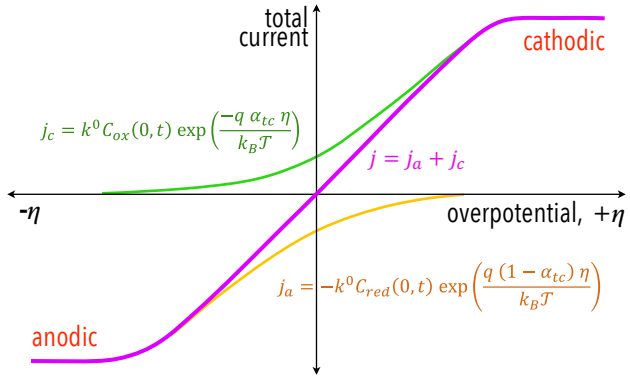

Figure 2.4: Total current (normalized) in BV formulation showing contributions from both cathodic and anodic components.[1]

k_f and k_b shall be used to define the heterogenous rate constants. Thus, under an applied overpotential ($|\eta| > 0$) at any time t, the current by reducing the species in solution would be $k_f \times C_{ox}(x = 0, t)$ while that from oxidizing the species would be $k_b \times C_{red}(x = 0, t)$, where $x = 0$ represent the immediately neighbouring layer to the metal surface. Hence the current density (j) *vs* overpotential (η) characteristics can be expressed as

$$j = k^0 \left(C_{ox}(0,t)\ exp\left(\frac{-q\alpha_{tc}\eta}{k_B\mathcal{T}}\right) - C_{red}(0,t)\ exp\left(\frac{q(1-\alpha_{tc})\eta}{k_B\mathcal{T}}\right)\right) \tag{2.8}$$

This is the general formulation of the well known Butler-Volmer (BV) model[36–38] of heterogenous kinetics. This has become the standard phenomenological description of electrode kinetics[1,39,40] that correlates electrode current with overpotential and redox concentrations. Figure 2.4 shows a typical current profile obtained from BV formulation. The equation reduces to Nernst expression under equilibrium conditions. At low overpotentials, contributions to total current j from both cathodic and anodic processes are considerable as it appears in the Figure. However, as η is made large, only one process can dominate and the total current is controlled either by the anodic component (shown on the negative

overpotential region in Figure 2.4) or by the cathodic component (on the positive overpotential region in Figure 2.4). At these limits, the current is essentially controlled by mass transfer effects via C_{ox} and C_{red}. In the absence of mass transfer, equation 2.8 effectively reduces to a Tafel expression[1] at high η, where again either the anodic or the cathodic term solely determine the current output.

Because of its coherence to these fundamental conditions , BV equation has been a very useful tool for analyzing experimental observations and gathering information about reaction mechanisms. In the past half century however, microscopic factors such as the nature and structure of electrochemical components in a system have emerged as fundamentally significant to the kinetics of electrode reactions. These microscopic aspects encompass chemical and electronic structure of reacting molecules or particles, and of electrode materials. It includes the role of solvent and surface adsorbed/grown foreign species in the probability of electron transfer. In the following section we shall focus on such microscopic approaches toward the formulation of electrode kinetics.

2.1.4 Heterogenous kinetics: microscopic models.

During the course of evolution of the microscopic regime, different aspects of electrochemical reaction and characteristics of reactant and solution were analyzed and incorporated in the emerged theories. The free energy/potential energy surface representation has been utilized extensively within this scope as well. In large part, the theories cover outer-sphere electrochemical reactions where an electron usually tunnels between a donor and an acceptor. Many redox processes in various disciplines of science, engineering, biology, medicine and other technologies are found to occur in this manner, where the electroactive group in a solution does not interact strongly with the electrode. A direct and strong

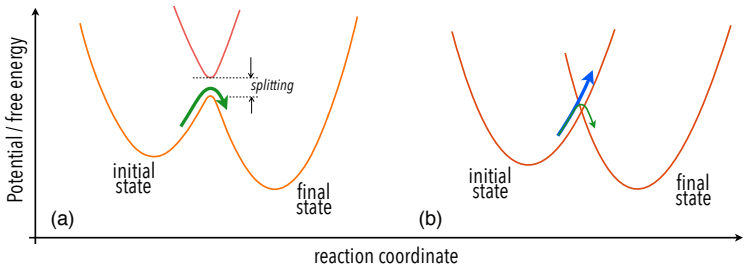

Figure 2.5: Adiabatic and non-adiabatic interactions.[2,3] In the adiabatic case (a) strong interaction between reactants and electrode opens a well-defined gap that leads to high transition probabilities from initial to final state once the system reaches the barrier. In the non-adiabatic case (b) the interaction is poor, causing the splitting at the intersection to be negligible. Therefore, most of the transition attempts are unsuccessful and the system stays in its initial state. This is marked with the heavy blue arrow. A successful transition may require 100,000 attempts[1] leading to low transfer probabilities (marked by green light arrow).

donor-acceptor interaction leads to specific effects such as bonding among species via adsorption, and thus falls into the category of inner-sphere electrode reactions[1]. Inner sphere interaction appear in many practical applications such as catalysis, fuel cells and batteries etc. In this thesis however, we deal with outer-sphere processes only, where an electron has to tunnel over a distance through a dielectric media *i.e.* monolayer and/or electrolyte solution between a donor and an acceptor. The distance between electrode and redox reactant is a significant component in the heterogenous rate picture, as it divides the physics of transfer process into adiabatic and non-adiabatic interactions. Adiabatic process dominates when the distance between electrode and reactants are rather short *i.e.* typically between 5-10 Å.[4] For longer distances a transfer event is likely to favour the tunnelling mechanism, which dominates the processes addressed in this work. Here, the interactions between electrode and reactants fall in the non-adiabatic category.

Figure 2.5 shows the outcomes of the two interactions via reactant and product potential energy surfaces, which outlines a much lower transition probability from an initial to a

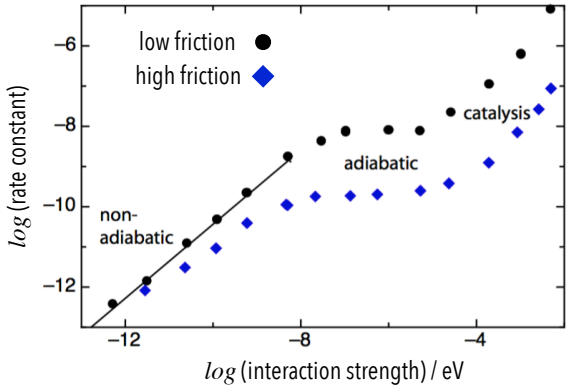

Figure 2.6: Variation of rate constant with interaction/coupling strength. *Reprinted from Ref. 4.*

final reactant state in the non-adiabatic case (part b). A well-known formulation on the rate of charge transfer under such conditions was first proposed by Landau and Zener.[2,3,41] This has been followed by decades of work, which have now resulted in more advanced and sophisticated theories. Seminal works were performed by Marcus[42,43], Hush[44,45], Chidsey[46], Levich[47], Dogonadze[48] and others, and their theories have been validated by experimental observations. Levich and Dogonadze addressed the non-adiabatic rate picture on the basis of the Landau-Zener formulation of the intersection area crossing, as appeared in Figure 2.5. Marcus incorporated the effect of reactants' nuclear structure in the form of identical reactant and product parabolic potential energy surfaces on kinetics of ET, which famously lead to his Nobel Prize in Chemistry. The consideration of nuclear structure in his theory gives rise to the energy of nuclear reorganization λ, which accompanies a typical ET process. This is an essential energy component that an electron must possess before it can make a transition from an initial to a final state. Later, Hush[44,45] provided a quantum mechanical formulation to Marcus theory which now is widely known as Marcus-Hush theory.

Typical outer-sphere electron transfer reactions at bare metal electrodes are adiabatic. Although the interaction between electrode and reactants are strong in this regime, the rate of reaction itself is independent of electronic coupling $|M|$. This is the well known Marcus-Hush plateau region as shown in Figure 2.6, where reactant and electrode share their electron; and the reaction mechanism can be formulated without considering any electronic level information of the reacting species.[4] On the other hand, the coupling $|M|$ can be much weaker for semiconductor electrodes, or if an electrodes is covered by an insulating film, or when an electrode and the reactants in a solution are separated by a suitable spacer such as a self-assembled monolayer (SAM). These scenarios represent the non-adiabatic regime where an electron tunnels through the insulating film or monolayer bridge between specific electronic levels in electrode and reactant. In such cases, the rate constants vary with the strength of electronic coupling $|M|^2/\hbar$, which represents overlap of the electronic states across the interface between a donor-acceptor couple. Here, $\hbar = h/2\pi$ is the reduced Planck's constant. This was incorporated into the rate picture by Gerischer[49–51] who formulated the transfer of electron via tunnelling between an occupied (empty) energy state in electrode and an empty (filled) redox state of matching energy in solution during a reduction (oxidation) process. The coupling is considered weak in these circumstances, which keeps the broadening of redox energy states to a minimum that arises from the overlap of electronic wavefunctions across an interface. However, in the presence of a solvent, the redox species can develop a solvation shell which leads to thermal broadening of the redox energy states via reorganization energy λ. This accounts for the changes in the nuclear structure of a solvation-shell as the redox-center gains or looses an electron (Figure 2.3).

Gerischer described such solvated energy level structures in the form of probability densities that determine the availability of these states for redox transfer. During a redox

process such as

$$Ox + e\ (metal) \leftrightharpoons Red,$$

the match of electronic states on the electrode given by its electrochemical potential to the solvated redox states determines the extent of ET across the interface. Since electrochemical potential can be varied with applied overpotential/bias η, one can calculate the instantaneous heterogenous rate constant via the coupling $|M|$ between these states. Thus a reduction/forward step $Ox + e \rightarrow Red$ (as in Figure 2.1) was defined with the rate expression[52,53]

$$k_f = \frac{4\pi^2}{h}|M|^2 \int D_S\ f(\varepsilon)\ D_{ox}\ d\varepsilon, \tag{2.9}$$

Where D_S is the density of electrode states, $f(\varepsilon) = [1 + exp((\varepsilon - \mu_{eq})/k_B\mathcal{T})]^{-1}$ is the Fermi function describing the electronic occupation in electrode, ε is the energy, μ_{eq} is the equilibrium electrochemical potential, k_B is Boltzmann's constant. D_{ox} is the Gerischer probability density of oxidized states available to accept an electron from the metal. We will discuss this function in more detail in the later sections. For a metal electrode, as employed in this work, the density of states D_S can be considered a constant[54] such that it acts as an electron reservoir within the applied range of overpotential. A similar expression can describe the oxidation/reverse process where the electrode accepts an electron from the redox state. We can write this rate as

$$k_b = \frac{4\pi^2}{h}|M|^2 \int D_S\ (1 - f(\varepsilon))\ D_{red}\ d\varepsilon, \tag{2.10}$$

where, $(1 - f(\varepsilon))$ defines the distribution of empty states in metal, D_{red} is the Gerischer probability density of reduced states that already possess an electron. A detailed connection has been presented between the rate and D_{ox}/D_{red} in Chapter 3. The coupling term $(|M|^2/\hbar)$, placed as an integral prefactor in these two rate equations 2.9 and 2.10 is an applied interpretation of the more general description that originally arose from Gerischer's

picture.[1] In a broader definition, a proportionality constant was defined between the transition probability of a transfer event and the density functions D_{ox} and D_{red} along with a frequency of transition. Different interpretations of the proportionality constant exist in the literature.[1] Nevertheless, its final form as coupling strength ($|M|^2/\hbar$) has become a standard practice within the electrochemistry community in addressing interfacial kinetics. Interestingly, the constant factor originally appeared within the integral (equations 2.9 and 2.10) which seemingly leads to the energy dependence of $|M|$. While this holds for ET in the realm of quantum transport, assuming energy independence of $|M|$ has become a standard treatment in non-adiabatic electrochemistry. This is convincingly supported by the vast majority of electrochemical measurements which demonstrate a symmetric Tafel slope.[55–58] This symmetry is unlikely to appear with the variation of coupling $|M|$ with energy (ε) of electrons.

2.1.5 Probability density function

The probability density is a central concept in the Gerischer rate picture which brings the effect of thermal vibration and nuclear reorientation of both electroactive and solvent species into the rate formulation. Consequently, it spreads over a range of energy at non-zero temperatures and as stated above shows a remarkable dependence on the nuclear reorganization energy λ. To begin with, such a state (D_{ox} and D_{red}) by definition can hold only one electron such that

$$\int_{-\infty}^{\infty} D_{ox}(\lambda, \varepsilon)\ d\varepsilon = 1, \qquad and \qquad \int_{-\infty}^{\infty} D_{red}(\lambda, \varepsilon)\ d\varepsilon = 1 \tag{2.11}$$

For these functions, a formal description can be obtained via Marcus' activation energy formulation. Let us explore this formulation[1] as given by

$$\Delta G_f^{\ddagger} = \frac{\lambda}{4}\left(1 - \frac{\eta}{\lambda}\right) \tag{2.12}$$

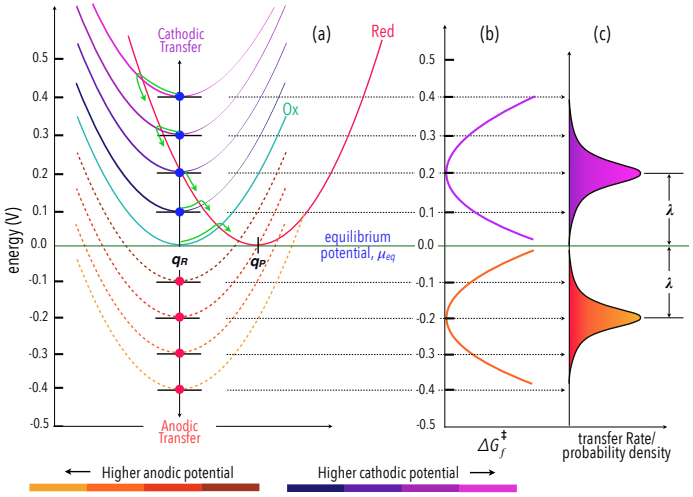

Figure 2.7: Connection between Marcus activation picture (equation 2.12) and the probability density functions D_{ox} and D_{red} via potential energy surfaces. Considering reduction ($Ox + e \rightarrow Red$), an increase in η raises the energy of electrons in metal, which raises the reactant energy surface (a). This reduces $\Delta G_f^{\ddagger}$ until it becomes zero (purple curve in (b)) when the reactant surface minima intersects with the product surface (a). This reduction in activation barrier is accompanied by increase in probability of ET as shown schematically in (c). Marcus predicted that with further rise in η, the barrier goes up again (a and b), which should reduce the transfer rate (c). However, in practice this is only observed in some homogenous reactions. The same description applies for the oxidation step ($Ox + e \leftarrow Red$). q_R and q_P in (a) are the minimum energy coordinates (e.g. bond-length) of the initial and final state.

while we take into account of the fact that an electron transfer event in metal always takes place from it's Fermi level. Here the overpotential $\eta = \varepsilon - \mu_{eq}$ is the excess potential applied to the metal over its equilibrium state (μ_{eq}). Initially, when the overpotential $\eta = 0$, the activation energy is the highest ($\Delta G_f^{\ddagger} = \lambda/4$). A qualitative description of this behaviour is presented schematically in Figure 2.7. It shows that for a given process such as a reduction reaction, the activation energy goes down as a positive η is applied, and then eventually becomes zero at $\eta = \lambda$. At this overpotential the rate of ET would be the highest. Upon further increase in overpotential, the activation energy goes up again and the consequent probability of ET begins to go down. Introducing this dependence of activation energy

into the Marcus rate picture leads to the expressions for probability densities[1] -

$$D_{ox}(\lambda,\eta) = \frac{1}{\sqrt{4\pi\lambda k_B \mathcal{T}}}\ exp\left(\frac{(\eta-\lambda)^2}{4\lambda k_B \mathcal{T}}\right),\ and \tag{2.13}$$

$$D_{red}(\lambda,\eta) = \frac{1}{\sqrt{4\pi\lambda k_B \mathcal{T}}}\ exp\left(\frac{(-\eta+\lambda)^2}{4\lambda k_B \mathcal{T}}\right) \tag{2.14}$$

for reduction and oxidation processes, respectively, which agree well with Gerischer's description.[49–51] These density expressions are Gaussian distributions (Figure 2.7(c)) with a mean at $\eta = \lambda$ and a standard deviation of $\sqrt{(}2\lambda k_B \mathcal{T})$. These definitions have widely been adopted in exploring interfacial processes. One typically includes the redox-energy levels into the exponential term to obtain a more explicit description of these states in terms of the overall energetics of the systems. We shall see such descriptions later in Chapter 5. Nevertheless, this simplified form allows us to understand how reorganization energy λ can control the extent of redox processes.

Before heading into detailed discussion, we take note of a critical point regarding the Marcus picture (equation 2.12) that leads to the above probability functions. As mentioned above, Marcus theory predicts that the activation energy begins to rise again beyond the zero activation point at $\eta = \lambda$, giving rise to the so called Marcus inverted region.[1] Although a decrease in rate constant has indeed been observed for homogenous ET[5] as presented in Figure 2.8a, the phenomenon does not appear in heterogenous processes at metal electrodes.[4] The continuous distribution of electronic states in a metal as described by the Fermi function $f(\varepsilon)$ in the equations 2.9 and 2.10 causes the rates to be independent of the applied overpotential at $\eta \gg \lambda$. Literature also suggests a possible explanation based on the reactant and product potential energy surfaces.[1,59] This is schematically illustrated in Figure 2.8b,c for a reduction reaction. Because of the presence of continuous states in a metal near its Fermi energy, a donor level would always remain available at the zero activation point under $\eta \geq \lambda$ at the intersection of the reactant and product surfaces. In this

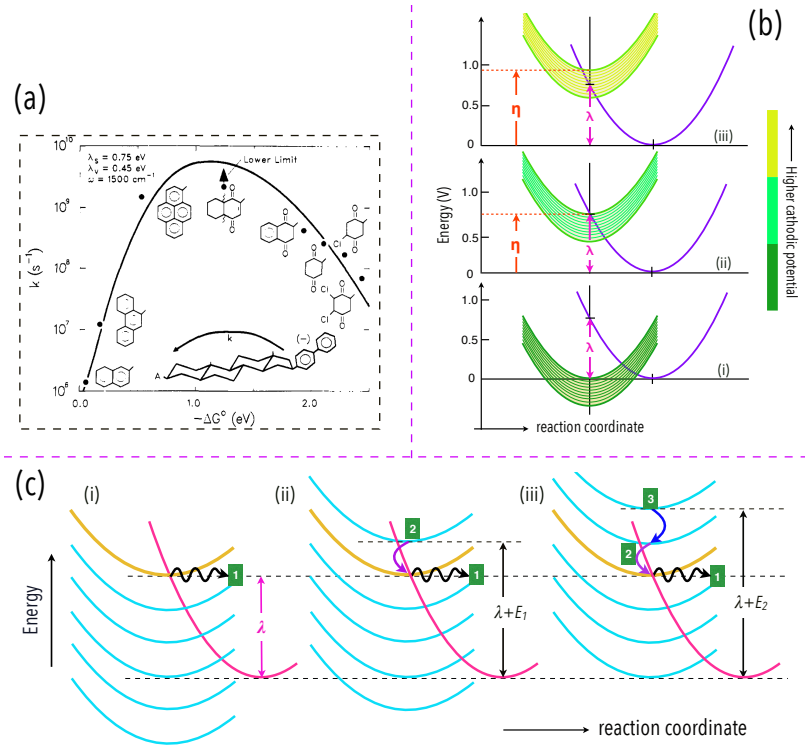

Figure 2.8: Marcus inverted region (*reprinted*) observed in the seminal work by Miller and coworkers[5] in a homogenous system (a). However, this inversion of activation energies do not apply in heterogenous cases, supposedly due to the presence of continuous energy levels in metal electrodes[1] as suggested in (b). Here, an occupied state (from metal) is suggested to be always available for reduction at zero activation point (b[ii,iii]). Once a state looses its electron (c[i]) to reduction, a higher energy electron dissipates its energy to drop into the emptied level (c[ii,iii]) and continue reduction.

picture, ET may continue at a maximum rate (Figure 2.7 and 2.8b,c) followed by a possible dissipation of electron from the Fermi energy to the emptied lower levels. Therefore, although the probability density of capturing a redox state in energy can be represented by the above Gaussian form, the final heterogenous rate at high η remains independent of it, unlike the possibility in a homogenous transfer process.

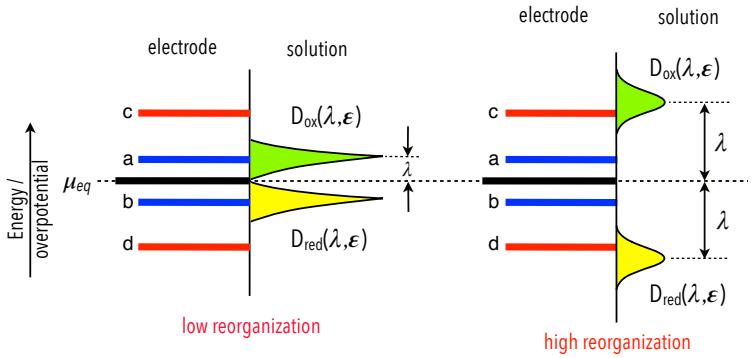

Figure 2.9: Effect of reorganization energy λ on ET.[1] For low λ (left), the required energy to transfer an electron is small, indicated by a and b for reduction and oxidation, respectively. In addition, limited broadening of redox states at low λ allows the transfer of electron within a low range of overpotentials. The efficiency of a transfer event goes down as λ increases (right). The states broaden more in energy (in accordance with equations 2.13 and 2.14) and a transfer requires higher overpotentials indicated by c (reduction) and d (oxidation).

2.1.6 Nuclear reorganization energy

The reorganization energy (λ) is a critical component in the rate picture as made obvious via equations 2.13 and 2.14. The schematic in Figure 2.9 shows how λ can control the efficiency of electron transfer. This energy to transform a reactant-solvent configuration into a product-solvent structure (Figure 2.7) has typically an inner (λ_i) and an outer (λ_o) component such that $\lambda = \lambda_i + \lambda_o$. The inner component on the one hand represents the changes in the molecular structure of a redox-active reactant, which is harmonic in nature and can be calculated by summing over the normal vibrational modes about the equilibrium configuration.[4] On the other hand, the outer mode captures the changes in the structure of the solvation shell surrounding a reactant molecule upon the loss or gain of an electron. The resulting polarization of the solvent follows Born model whereby the Coulomb interaction with the ionic charge is taken into account. This has contributions firstly from the electronic polarizability of the solvent molecules where a reactant can respond instantly to an ET, which is typically on a time scale of $10^{-15} - 10^{-16}$ s.[4] This is

also called the *fast polarization* which can be defined by the optical dielectric constant ϵ_∞. Typically ϵ_∞ can be small (*i.e.* $\epsilon_\infty = 1.88$ for water) with respect to the static dielectric constant (ϵ_s), which defines the second contribution to polarization of the outer mode. This is also known as the *slow polarization* that arises from the reorientation and distortion of the solvent molecules during charge transfer. Based on these contributions, one can express the outer reorganization energy as[1,4,60]

$$\lambda_o = \frac{q^2}{8\pi\epsilon_0}\left(\frac{1}{\epsilon_\infty} - \frac{1}{\epsilon_s}\right)\left(\frac{1}{r_s} - \frac{1}{2d_{mr}}\right) \tag{2.15}$$

where, r_s is the radius of the reactant species and d_{mr} is it's distance from an electrode (metal) surface; ϵ_0 is the permittivity of vacuum, q the charge of electron as before. In many cases, this outer component (λ_o) dominates the total reorganization energy λ since the extent of solvent reorientation can be large compared to the distortion of the redox-active molecule itself upon a change in charge state. To activate an ET across a metal-liquid interface, this energy must be supplied via overpotential (as suggested in Figure 2.9) in addition to the standard redox potential for the process. As highlighted in Chapter 5, the two contributions have an intimate connection to Coulomb charging energy as well, which is critical to the final energy demand for a transfer process.

Effect on kinetics. Marcus theory provides a qualitative understanding of the role played by λ_i on reaction kinetics via equation 2.12. For example the activation energy is $\Delta G_f^\ddagger = \lambda/4$ at equilibrium with $\eta = 0$, where the forward (k_f) and backward (k_b) rates are equal to equilibrium rate constant k^0, as illustrated in Figure 2.10a,b. A smaller internal reorganization means that the reactant and product species have a similar structure upon the exchange of an electron (Figure 2.10a), which would result in a larger k^0. Similarly, a considerable change in molecular structure *e.g.* bond length is accompanied by a large λ_i (as suggested in Figure 2.10b), causing k^0 to be small and thus, would require higher

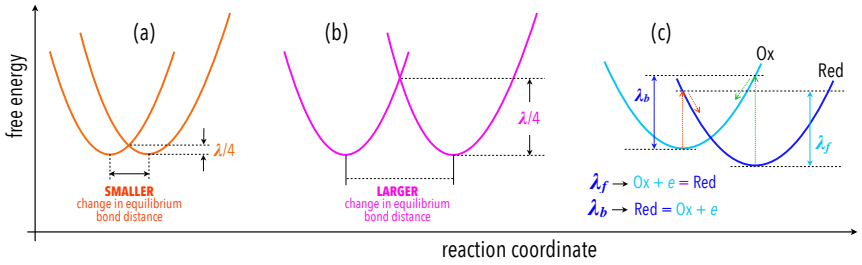

Figure 2.10: Reorganization energy (λ) and molecular structure *e.g.* bond length. Small λ means a small shift in molecular structure (a), whereas large λ causes a large change in structure (b). Part (c) shows that the reorganization energies for forward (λ_f) and backward (λ_b) processes can be different if the reorganized structure settles into a new minimum energy followed by an ET.

external potential (η) to make a transfer. The size of a molecule/nanoparticle can also influence the kinetics, which appears via the λ_o in equation 2.15. Large particles (via the radius r_s) typically have a low λ_o due to a lower solvation energy and a consequent smaller change in the structure of solvation-shell upon ET. This is possibly due to lower charge density in larger species. Conversely, the solvation shell would be much more responsive upon the transfer of an electron around a smaller reactant molecule/particle, resulting in a higher λ_o and a higher energy demand to activate an ET. In practical heterogenous systems therefore, it can be quite useful to have λ measured beforehand to predict and understand the efficiency of the redox processes therein. In Chapter 3 and 5 a method is proposed and discussed, and discussed for different energetic equilibrium between a metal and a redox-group that may allow experimental determination of reorganization energy via linear sweep voltammetry.

2.1.7 Coupling kinetics to mass transfer

Until this point, we have focused on understanding the fundamental elements in a heterogenous rate picture. While this is a prerequisite to predict and sense the behaviour

of a redox-active species, it essentially has to be connected to the transfer of electroactive masses to and away from an electrode surface along the progress of reaction in order to interpret the electrochemical current response under an applied overpotential. In typical Butler-Volmer formulation, the faradaic exchange is principally limited on the surface concentration of redox species only.[1] However, in the outer-sphere regime, quantum tunnelling of electrons may occur to/from a range of distance in solution, which activates redox species far beyond the surface layer for a gain (reduction) or loss (oxidation) of electron. A detailed interaction of these species with metal under applied overpotential is outlined in Figure 2.11. Here the reactant concentrations come to play along with equations 2.11, 2.13, 2.14 (Figure 2.11a). For unbound redox species, the evolution of single or multiple charged states in solution under non-equilibrium conditions can induce drift and diffusion of these charged states to and away from the surface (as shown in Figure 2.11b,c). The resulting changes in reactant concentration at and near the interface impacts the availability of active species for the redox reaction, which effects the magnitude of final current shown in Part (d) of the Figure. In Chapter 4 a general theoretical formulation is presented to capture the role of drift and diffusion. Typical electrochemical processes take place under the presence of supporting ions in an electrolyte solution. These ions perform the essential task of screening the potential at an interface (Figure 4.1) which otherwise can raise the required overpotential to transfer an electron well beyond the predicted energy demand in a redox process. Transport of both redox-active and supporting ions in solution occur on the basis of drift and diffusion and they give rise to faradaic/electron current and non-faradaic/charging current, respectively. Its the faradaic component that one seeks in a typical electrochemical study. In Chapter 4 the two contributions have been isolated and analyzed to explore in detail their role on a final observable current. Although both

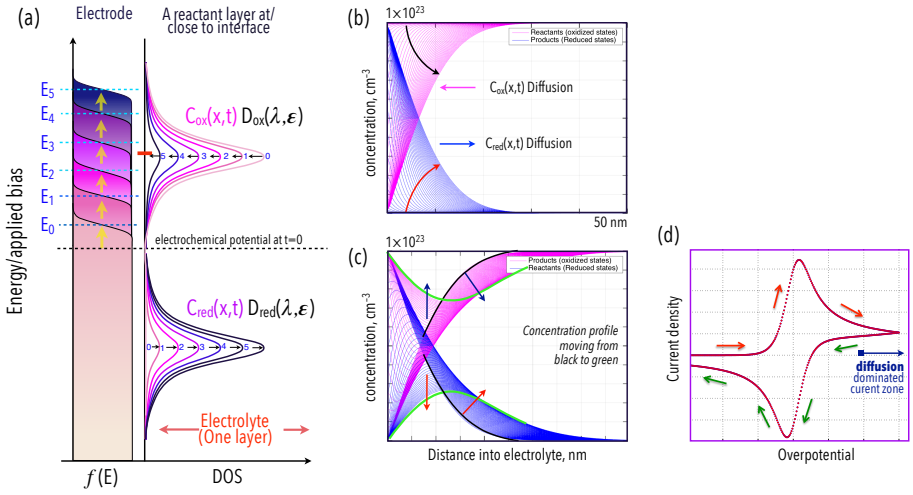

Figure 2.11: Combining Gerischer density of states ($D_{ox}(\lambda, \varepsilon)$ and $D_{red}(\lambda, \varepsilon)$) to concentration of reactants at different distances from interface. The DOS can be multiplied to reflect the total concentration of oxidized and reduced reactants via equation 2.11 such that $\int D_{ox}(\lambda, \varepsilon) \times C_{ox}(x,t) = C_{ox}(x,t)$ and $\int D_{red}(\lambda, \varepsilon) \times C_{red}(x,t) = C_{red}(x,t)$, respectively. With reduction, the concentration of oxidized reactant (C_{ox}) goes down (shown with numbered arrows on top of part (a)), while the reduced reactant concentration (C_{red}) goes up (shown with arrows at the bottom of part (a)). This can be implemented for reactant concentrations at different distances at/near the interface. The resulting evolution of concentrations are shown in (b) and (c) during a cyclic change in cathodic (marked by $0 \rightarrow E_0 \rightarrow E_5$ in part (a)) and anodic (not marked) overpotentials. $C_{ox}(x,t)$ goes down with reaction (purple profiles) while $C_{red}(x,t)$ goes up (blue profiles) (b). At the same time, reactants diffuse to ($C_{ox}(x,t)$) and away ($C_{red}(x,t)$) from interface due to the concentration gradients. The process reverses during oxidation under anodic overpotentials (c). The density profiles in part (a) move in the direction opposite to that marked to show cathodic processes. The built-up concentrations of C_{ox} and C_{red} during cathodic bias attempt to reverse in oxidation cycle and move back towards their original profile (c). However, the original profile at $t = 0$ cannot be retrieved after a full cycle of overpotential.[6] The associated current is shown in part (d).

of these currents have fundamentally unique origin, the transport of both redox and solvent ions/molecules/particles in solution can be formulated on the basis of the same drift and diffusion theories. The changes in redox reactant concentrations *i.e.* C_{ox} and C_{red} for oxidized and reduced reactants, respectively, resulting from these movements are coupled

with rate expressions such as the equations 2.9 and 2.10 to obtain the final faradaic current (as in Figure 2.11d) which has the form,

$$j_{et}(\eta,t) = 4\pi^2 q \frac{|M|^2}{h} D_S \; [\; C_{ox}(t) \int f(\varepsilon+\eta)\; D_{ox}(\varepsilon)\; d\varepsilon \\ -\; C_{red}(t) \int (1-f(\varepsilon+\eta))\; D_{red}(\varepsilon)\; d\varepsilon \;], \tag{2.16}$$

Here, j_{et} is the electron transfer/faradic current. Typically this current is accompanied by a charging current from the transport (e.g. drift and diffusion) of supporting ions in solution. A comprehensive analysis in this regard appears in Chapter 4. Typically, one may wish to see the faradaic current only; however, interference from the charging component in a voltammogram becomes more pronounced as scan rate increases. In such cases, a closer attention is required to understand the nature of current output as it can be quite different from the current in slow scan rate regime (Figure 2.11d).

2.1.8 Heterogenous rate picture: a view from quantum transport

Equations 2.9 and 2.10 form the basis of the electrochemical studies performed in this thesis. These equations originated in the electrochemistry community, and were based upon the total energy picture via reactant potential energy surfaces.[1] It was Gerischer who introduced the single-particle energy level approach in these rate expressions[1,4] for heterogenous electron transfer processes. This approach implies a potential connection to the condensed matter physics community, where a typical transport phenomena is viewed on the basis of Landauer's quantum transport picture.[61] In recent years, a direct connection between these two theories has been established,[7] where the quantum transport theory has been shown to converge into the same electrochemistry via equations 2.9 and 2.10. Such a connection can potentially broaden the access of the solild-state community into the field

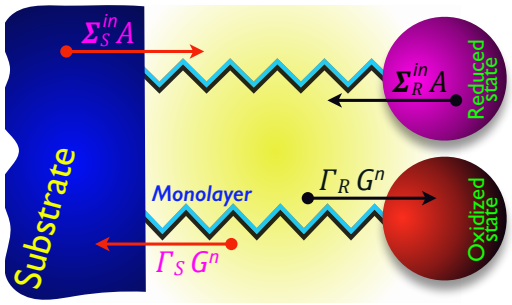

Figure 2.12: NEGF description of redox charge transfer through a monolayer bridge[7].

of electrochemistry, which can effectively enhance the development and progress of various applied technologies.

The connection[7] utilizes non-equilibrium Green's function (NEGF) representation of the Landauer quantum transport picture[62] in a redox-functionalized self-assembled monolayer configuration (Figure 2.12), from which the typical electrochemical transport formulation was derived.[4,52] The model system may appear as in Figure 2.12, which has all the NEGF relevant quantities defined. The Landauer's electron transmission probability to or from the reactant species at any bias, including zero bias can be expressed as[62,63]

$$T(E) = tr[\ A_R\ M\ A_S\ M^{\dagger}\ ]. \tag{2.17}$$

Here, $M = \tau_R^{\dagger}\ G\ \tau_S^{\dagger}$ is the substrate-reactant coupling matrix, where G is the partitioned Green's function characterizing the monolayer and can be expressed as $[G] = [(E + i\eta)S - H - \Sigma_R - \Sigma_S]^{-1}$. In this expression, the typical linear combination of atomic orbitals (LCAO) representation was assumed;[7] thus, $[S]$ and $[H]$ represent the monolayer overlap and Hamiltonian matrices, respectively. The Green's function self-energies, Σ_R and Σ_S, capture the monolayer's interaction with the reactants and the substrate while τ_R and τ_S are the reactant and substrate monolayer coupling matrices, respectively. The spectral functions $[A_R]$ and $[A_S]$ for the reactant and substrate, are related to the DOS matrices by

$[D_S] = [A_S]/2\pi$ and $[D_R] = [A_R]/2\pi$ – from which quantities such as the projected DOS and the local DOS can be calculated. Although, equation 2.17 is not the usual Landauer transmission expression[62,63], it can be related to the usual expression via

$$\begin{aligned} T(E) &= tr[\ A_R\ M\ A_S\ M^\dagger\ ] \\ &= tr[\ A_R\ \tau_R^\dagger\ G\ \tau_S^\dagger\ A_S\ \tau_S\ G^\dagger \tau_R] \\ &= tr[\tau_R\ A_R\ \tau_R^\dagger\ G\ \tau_S^\dagger\ A_S\ \tau_S\ G^\dagger] \\ &= tr[\Gamma_R\ G\ \Gamma_S\ G^\dagger] \end{aligned} \tag{2.18}$$

where $\Gamma_R = i(\Sigma_R - \Sigma_R^\dagger)$ and $\Gamma_S = i(\Sigma_S - \Sigma_S^\dagger)$ are the reactant and substrate broadening matrices[62,63]. The current flow from this transmission expression was obtained by considering electron transition from a filled to an empty state as shown in Figure 2.12 and 3.1. At equilibrium, the net current flow is zero due to equal and opposite ET events to and from the substrate.

On the basis of the representation in Figure 2.12, the electron current from the substrate to an oxidized species, across the substrate-monolayer interface can be defined as,[64]

$$\begin{aligned} I_e^{+z} &= \frac{q^2}{h} \int\ tr[\ f\ \Gamma_S\ A\ -\Gamma_S\ G^n] dE \\ &= \frac{q^2}{h} \int\ tr\left[\ \Gamma_S f\ G[\Gamma_R + \Gamma_S] G^\dagger\ -\Gamma_S\ G[\theta\Gamma_R + f\Gamma_S] G^\dagger\ \right] dE \\ &= \frac{q^2}{h} \int (f - \theta)\ tr\left[\ \Gamma_S\ G\ \Gamma_R\ G^\dagger\ \right] dE \\ &= \frac{q^2}{h} \int f\ T(E) dE \end{aligned} \tag{2.19}$$

where, θ defines the occupation factor of an oxidized reactant which is 0, f the Fermi distribution, G^n is the monolayer electron correlation function, and A the monolayer spectral

function. Combining equation 2.19 with equation 2.18 leads to[7]

$$I_e^{+z} = 4\pi^2 q \ \frac{|M|^2}{h} \int f(E) \ D_{ox}(E) \ D_S(E) \ dE \tag{2.20}$$

Likewise, ET from a filled reduced state to the substrate can be expressed as[7]

$$\begin{aligned} I_e^{-z} &= \frac{q^2}{h} \ \int [1 - f(E)] \ tr[D_{red} \ M \ D_S \ M^\dagger] \ 4\pi^2 \ dE \\ &= 4\pi^2 q \ \frac{|M|^2}{h} \int [1 - f(E)] \ D_{red}(E) \ D_S(E) \ dE \end{aligned} \tag{2.21}$$

such that the total electron current between a single reactant and the substrate is $I_e = I_e^{+z} - I_e^{-z}$. While these expressions hold for a single reactant, usually one would deal with an ensemble of reactants that make up the monolayer in a typical electrochemical experiment. The current density j ensuing from such collection of reactants is dictated by the coverage of surface that represents the number of reactants per unit area. Under equilibrium, this is given by

$$\begin{aligned} j = 4\pi^2 q \frac{|M|^2}{h} \ D_S \ \ [\ C_{ox} \int f(E) \ D_{ox}(E) \ dE \\ - \ C_{red} \int (1 - f(E)) \ D_{red}(E) \ dE \ ], \end{aligned} \tag{2.22}$$

where the coverage of oxidized (empty) reactants are distinguished by C_{ox} from those that are reduced (filled) by C_{red}. However, the net equilibrium current flow is zero. In this model monolayer system mass transfer kinetics such as diffusion was ignored.[57] This quantum transport based expression is identical[7] to the electrochemically derived current as in equation 2.16. This convergence highlights the possibility of an improved understanding of electrochemical interactions from a broader fields of expertise.

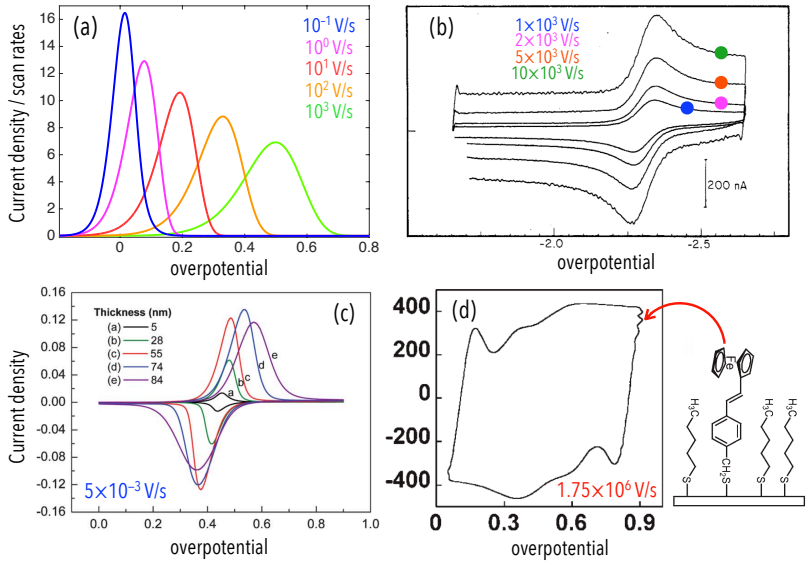

Figure 2.13: Effect of scan rates on faradaic current density in redox-active monolayer based heterogenous configurations (a).[8–10] Part (b) and (c) shows diffusion-dominated (*reprinted from Ref. 11*) and diffusionless (*reprinted from Ref. 12*) faradaic responses, respectively in monolayer based systems. Part (d) shows a plateaued total current (faradaic plus charging) response under ultrafast scan rates *(reprinted from Ref. 13,14)* in complex redox-active molecular wires (shown on the side).

2.1.9 Role of applied scan rate

The scan rate R, expressed in V/s influences both faradaic/redox/electronic and non-faradaic/charging/ionic current. Typically, slower scan rates allow a significant degree of interfacial activities - both faradaic and non-faradaic. The duration of these activities become limited as scan rate is increased. The evolution of current output is better understandable when scan rate is raised by orders of magnitude as shown in Figure 2.13a.

At very low scan rates, the features that define a faradaic current profile such as peak potential, peak current height, width of current peak etc do not show any noticeable dependence on scan rates.[6] This independence arises from the fact that electrons in metal can reduce or oxidize all the available reactants at and near an interface at a rate that is

much higher than the rate of increment in overpotential before reaching to a new equilibrium state. In a restricted reactant-diffusion medium, the resulting current is likely to fall to zero[12] at steady-state after reaching the peak as shown in Figure 2.13c for organic radical batteries. Under high reactant diffusion in electrolyte, the faradaic current falls asymptotically beyond its peak[11] at steady state (Figure 2.13b). A low scan rate voltammogram would typically be dominated by the faradaic component alone, as contribution form the charging component becomes negligible on account of the long allowed time. This negligible contribution typically indicates a proper screening of any potential drop at the interface arising from an applied electrode overpotential. This property of charging component along with the associated screening and their evolution with increased scan rate is addressed in detail in Chapter 4.

If the scan rate R is increased, the time available for electron transfer goes down, causing the same quantity of redox reactions to occur over a longer time period than that under a slow scan rate voltammetry (Figure 2.13a). Hence the peak width broadens in overpotential. At the same time, the current density goes up as well due to faster sweeping. This trend is likely to be consistent as one increases R until to the point where the current peak disappears and saturates into a plateau. In practice however, this is only likely at very high scan rates *i.e.* typically $\geq 10^6$ V/s, which as explained in Chapter 3 and 4 is a function of interfacial coupling strength $|M|$. In addition, the non-faradaic/charging current begins to appears at high scan rate as well; although, its effect on screening in a voltammogram is negligible up to 10^4 V/s.[65] In general, the rate and the current expressions do not capture the role of scan rate; rather, it is captured via the evolution of reduced and oxidized reactants in the allowed timescale during the charge transfer processes under an applied bias. The details of this incorporation into the rate picture is implemented in

Chapter 4.

2.2 Bridge mediated electron transfer

In the past few decades, bridge mediated electron transport has become a subject of widespread investigation across various disciplines of science, engineering, medicine and pharmaceutical research. Typically, these bridges are monolayers of polymeric chain/ molecule that can be self-assembled on a metal electrode such as Au or Pt at one end. The other end of these monolayers can be functionalized with a redox-active group that can hold and exchange one or more electrons under non-equilibrium conditions ($|\eta| > 0$). Depending on the chemical nature of a monolayer, it can act as a fast, conducting channel for an electron to tunnel between the metal and the redox-group, or it can act as an insulator to a transfer event. In general, saturated alkane groups such as $C_{11}H_{24}$ act as

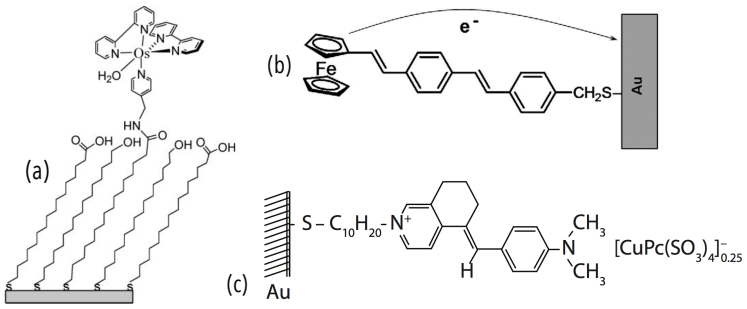

Figure 2.14: Saturated (a) and π-conjugate (b,c) monolayers. Many such chain compounds are found in electronic and electrochemical applications. The structures are *reprinted from Ref. 15–17* .

an insulating media,[46] whereas the presence of π-conjugate compounds such as benzene (C_6H_6) in a chain can act as a fast conducting channel. This range of variability between insulating and conducting character is one of the most appealing features of monolayer-mediated transport as it offers great flexibility in system design. In addition, the degree

of conduction can also be varied by changing the length of such a monolayer. For example cutting $C_{11}H_{24}$ to a shorter alkane group would allow faster electron tunnelling and therefore faster conduction.

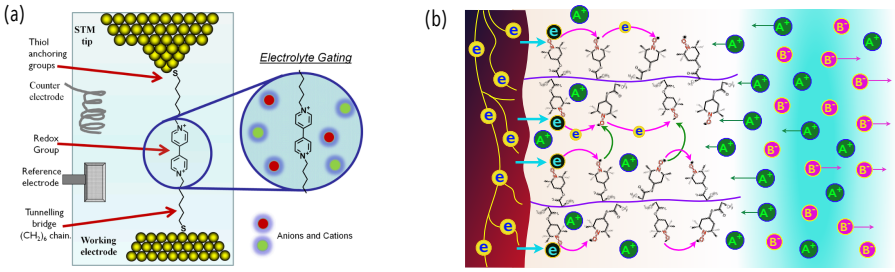

Figure 2.15: Redox-active electronics based on self-assembled monolayers. Two contact molecular wire (a) and single contact organic radical battery (b). *Reprinted and adopted from Ref. 18 and 19* respectively.

Monolayer mediated systems appear in molecular electronics, electrochemical energy storage and capacitor applications, sensors, in various organic radical devices such as organic semiconductors and resistive memory devices, and in drug delivery etc. From the electron-transport point of view, one the one hand, these systems can either have a typical double contact junction where an electron tunnels between two electrodes through a bridging monolayer, as shown in Figure 2.15a. Here the two ends of the monolayer are connected to an anode and a cathode, and the conduction is dictated by the chemical makeup of the monolayer.[18] This configuration is typically found in molecular electronic devices. On the other hand, a system can effectively be a single-contact system, where a monolayer is only connected to an electrode at one end, whereas it's opposite end is usually modified with a redox-active group, as illustrated by the organic radical battery configuration in Figure 2.15b. Although, the system would have another electrode to complete the circuit like in any other electrochemical configuration, the electrochemistry here can essentially be explored by analyzing the charge transport at one interface only. Various

organic radical based systems such as batteries, semiconductors etc features this configuration. The work presented in this thesis is focused mainly on the fundamental aspects of ET at single-contact interfaces.

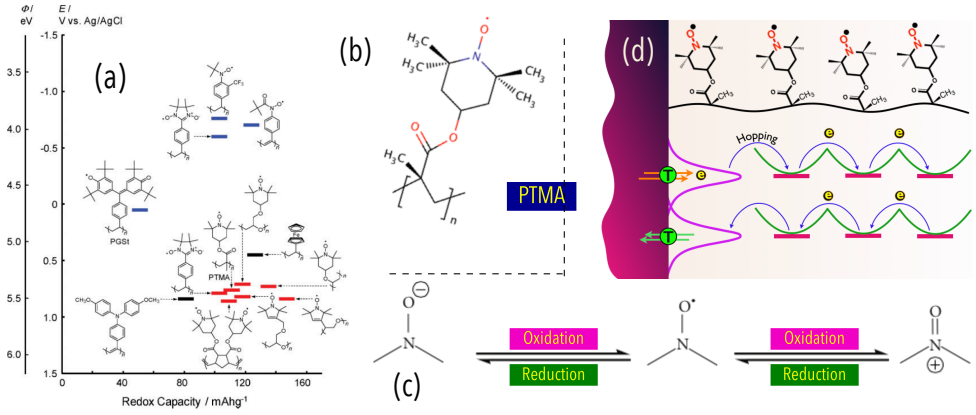

Figure 2.16: Redox-potentials of some popular radical molecules for organic radical batteries, *reprinted from Ref. 20.* Among them, most popular is the PTMA (b), which is capable of donating or accepting its electron (c)[21]. The combined tunnelling and hopping mechanisms for ET in typical organic radical battery configurations (as shown in Figure 2.15b) are illustrated in (d), *adopted from Ref. 20.*

2.2.1 Organic device systems

An exciting prospect within single-contact configurations appears in organic radical storages *i.e.* batteries and super-capacitors.[20,66–68] A generic structure is shown in Figure 2.15b where in principle charge transfer occurs through metal-monolayer-radical group configuration. Conduction in these systems can take place over a longer distance in space for greater energy storage, which is achieved by branching the radicals over a long polymeric chain that acts as a backbone. These chains disperse in electrolyte from a metal contact and allow easy transport of supporting ions during the charging and discharging cycles (Figure 2.15b). The supporting ion transport as discussed above ensures interfacial screening for efficient electron transfer. A widely adopted radical in such organic devices

is 2,2,6,6-tetramethyl-1-piperidinyloxy or commonly known as TEMPO that exhibits reversible oxidation and reduction behaviour[21]. This radical unit was first utilized in 2002 as a repeating unit in poly(2,2,6,6-tetramethylpiperidinyloxy-4-ylmethacrylate) or as known as PTMA polymer as the cathode in organic radical battery (Figure 2.16(b-d)). Since then, many other radical species have emerged[23,69] as shown in Figure 2.16a, while PTMA remains one of the most popular choices. In such a long chain configuration, in addition to tunnelling, ET can take place via a hopping mechanism between the neighbouring radicals as illustrated in Figure 2.16d. Although conduction within these polymer cathodes are represented via phenomenological diffusional parameters of electrons, opportunities remain wide open for deeper atomic level investigation of charge transfer along long chains.

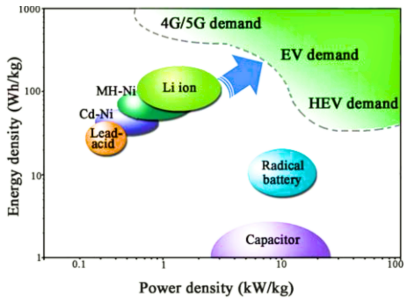

Figure 2.17: The potential of organic radical batteries for usage in electric and hybrid vehicles in terms of their high power density compared to other available cathode materials, although the energy density still lags behind the more prevalent cathode systems such as $LiFePO_4$. (*reprinted from Ref. 22*)

A remarkable advantage of organic radical batteries is their high rate constants[20,32] at both interfacial and hopping (along chain) electron transfer processes compared to that in the present day Lithium-ion cathodes. On the one hand, this allows superior power densities in organic batteries compared to the current technologies. However on the other hand, their energy density lags considerably behind than the more widely used $LiFePO_4$ cathodes.[22,32] This picture has been summarized in Figure 2.17 for potential applications

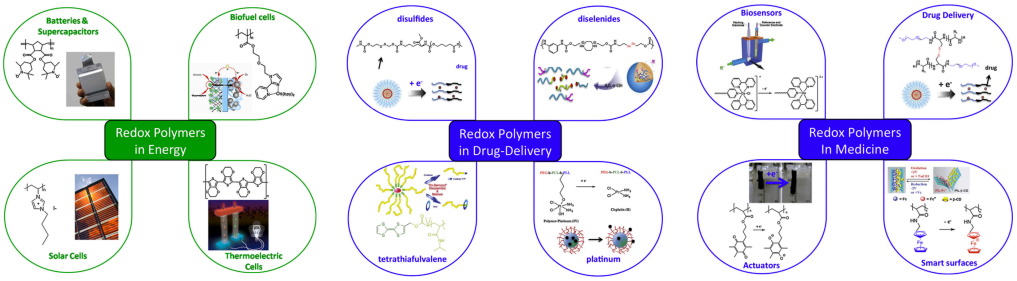

Figure 2.18: Application of redox-active polymers across various disciplines in science and engineering (*reprinted from Ref. 23*)

in electric vehicles.[22] To couple these two desired characteristics, a hybrid $LiFePO_4$/PTMA system has been developed which shows excellent improvement in power delivery.[32] While effective assembly of such radical polymers in a cathode-electrolyte system remains limited by the associated high cost, with relentless prevailing pursuit, much can be expected in future from these systems.

While storage applications have emerged as an exciting new prospect of organic radical based systems, the versatility of self-assembly and organic radicals goes far beyond into many other promising device applications. The organic radical configuration utilized in batteries were also implemented in organic resistive memory devices (memristors) and organic semiconductors with a promising prospect.[20,23,70,71] The efficiency in all these devices depend on a common aspect - the effective occupation of radical groups under an applied bias. Systems with and without an electrolyte have both been reported in literature. Some perspective systems are shown in Figure 2.18.

Another frequent application of self-assembled monolayers in electroanalytical chemistry is found in the development of sensors.[72,73] The surface of an electrode modified by SAMs provide strong selectivity for a specific analyte in solution at very low concentrations.[74] In addition, they protect an electrode from absorption of surface-active species in solution which allows the interface to retain its sensitivity for detection of a given species.

Typically SAM modified electrodes are employed to monitor pH, and detect inorganic and organic molecules. For example, carboxylic acid functionalized SAMs has been utilized to detect the presence of harmful Cd^{2+} in food industries with a detection limit in the range of 1 parts per billion (ppb).[73,74] Such limits mark the high sensitivity regime offered by SAM based sensors. In present days biosensors have become the more popular and established technology for sensing activities in food processing and monitoring, in medical fields, metabolic engineering etc.[73]

2.3 Electrochemical Methods

Typically there are mainly four electrochemical techniques[75] that are employed to explore the rate of electron transport in redox-active SAMs: cyclic voltammetry (CV), chronoamperometry (CA), alternating current voltammetry (ACV) and electrochemical impedance spectroscopy (EIS). Because of the inexpensive and well-understood nature of instrumentation, CV is one of the most widely used tool in electrochemistry, and is commonly utilized in SAM characterization. Here, a potential is applied in time at a specific rate at an electrode (as illustrations show in Figures 2.1, 2.4 and 2.11) which is in contact with an electrolyte. The redox groups under investigation float in an electrolyte solution, coupled to an electrode via SAMs (as in Figures 2.14, 2.15, 2.16). The applied potential scheme can range from a simple linear sweep (LSV) to differential pulse voltammetry (DPV).[1] These different schemes typically provide the opportunity to analyze and understand electron transfers with great flexibility and to see how they can be affected by other electrochemical and non-faradaic variables in solution.

In accordance with the redox potential of a given redox-active species, CV generates a peak in current profile when an external potential is applied, as shown in Figures 2.11 and 2.13. This peak is generally a confirmation of a redox event. The position (peak potential),

and width of such a peak and the background current contribution to the overall profile can give a wealth of information regarding the kinetics of the interfacial processes. Both peak position and peak width are functions of scan rate, which are more apparent at higher scan rates. As scan rate is increased, any given redox-peak shifts toward higher overpotential and the peak width increases (Figure 2.13a). The faradaic current is proportional to the scan rate as well. The initial rise in current (following Tafel's law) gives information about the surface coverage via the slope of the current[75]. In case of diffusion mediated transport of reactants in electrolyte, the diffusion-current contribution can appear as a plateaued response at overpotentials beyond the faradaic peak (Figure 2.11d and 2.13b). The origin of electrochemical responses during CV can be divided into two categories. The first kind arises from the electronic and geometric structure of redox-active species while the second kind comes from the transport characteristics of solvent ions/molecules in a given solution. While there is a strong correlation between these factors and the nature of current in a CV, it is challenging to establish this correlation based on voltammetric output - mostly due to the presence of strong interfacial kinetics. In Chapter 5 we formulate and discuss how suppressing the faradaic kinetics at high scan rate regime can lead to a direct and easy correlation between a current vs voltage profile and the various energetic parameters of a solvated monolayer-bridged redox environment.

Very high scan rates in voltammetry are typically employed to determine critical ET steps in chemical reaction to uncover reaction mechanisms. This is applicable in fast ET rate processes where a typical slow scan rate voltammetry is unlikely to exhibit a redox peak.[76] Fast scan rates such as those in the order of KV/s to MV/s are needed in such cases to gain confirmation of any redox events. While the need to explore the high scan rate regime was known well among electrochemists, the implementation was challenging with the prevailing planar electrode geometry. At ultra/fast potential sweeping,

planar electrodes generate a high charging current (non-faradaic) in voltammogram (Figure 2.13b,d), which can easily undermine or even suppress the faradaic component.[76] Moreover, high sweep rate causes the potential applied to an electrode to drop over a long distance in solution, which due to smaller allowed time in ultrafast voltammetry are less likely to be screened by supporting ions in electrolyte. The excess potential in electrolyte can make the redox process highly energy intensive by raising the molecular acceptor/donor energy levels of redox species (See Figure 1 in Chapter 4). Both of these limitations were resolved by replacing the planar electrode by a microelectrode which effectively causes charge transport to occur radially, as opposed to linear transport in planar electrodes. Because of the radial nature of ionic diffusion from electrolyte bulk towards interface (or away from interface) with a microelectrode, screening is achieved at a faster rate which leads to a reduced potential-drop and a low charging current. Although it is now possible to fabricate nanoelectrodes that can induce strong ionic drift and diffusion, the upper limit of maximum applicable scan rate remains in the order of $\sim 10^6$ V/s due to the limitation in ionic diffusivity constants in electrolyte. Further development in this regard is discussed in Chapter 3.

Besides CV, another useful technique to characterize SAMs is chronoamperometry (CA), where a single potential step is applied in time to capture the resulting decay in current.[1,75] Typically such step experiments allow us to see the trend in charging current which as explained above can potentially interfere with the concurrent faradaic component. The time required for a satisfactory decay in charging current can be a very useful information for collecting pure faradaic response during investigations. As shown in Chapter 4, a simple linear sweep voltammetry (LSV) scheme can be broken into much finer potential steps, each of which mimic the step in CA. The length of steps here is critical to the strength and quality of faradaic response collected in voltammetry.

The CV or LSV experiment can be performed with a sinusoidally oscillating voltage.[1,75,77] The technique is known as alternating current (AC) voltammetry. Typically this method is utilized where diffusion dominates among the modes of transport and usually needs to be coupled with a voltage sweep experiment.[75] Here the perturbation in applied voltage causes the reactants in solution to move back and forth from an interface. Depending on the frequency of perturbation, the ratio between peak current and background current varies. Collecting this data for a range of frequencies provide useful kinetic information of the redox processes. Creager and coworkers have utilized this method in redox-active SAMs to build the Randles equivalent circuit from which the rate constants can be calculated.[75,78]

Redox-active SAMs are also analyzed with electrochemical impedance spectroscopy (EIS)[75] where an AC signal is applied to electrochemical cell over a range of frequencies. Typically the method is applicable in diffusion dominated processes. During measurement, the system usually is required to be in a steady state, without which results can lack accuracy. Therefore, the technique can be time consuming. However, it allows several different parameters to be measured in one experiment such as electrolyte resistance, double layer capacitance, polarization resistance, charge transfer resistance, identification of diffusion dominated processes, distinguishing between multiple electrochemical reactions in a system etc. The data obtained at various frequencies from EIS can be used to determine the elements in the Randles circuit from which the rate constant can be obtained.

An advanced technique to understand redox reaction in SAM is scanning electrochemical microscopy (SECM).[75,79,80] Its operation resembles that of scanning tunnelling microscopy (STM). Here a metallic tip with a radius in the range of micro to nano meters scan the monolayer modified surface. This tip can be placed very close to the redox groups on monolayers and can probe an entire surface to explore its reactivity. The experiments

are done under steady-state conditions which allow minimization of double-layer charging current and potential drop at interface. Since multiple measurements of rate constants on different points on monolayer covered surface can be performed, the method can be used to determine the spacial heterogeneity in SAMs.

2.4 Present challenges and the objectives of the thesis

Faradaic response in any electrochemical device system is critically dependent upon different energetic components of the entire system. These energies arise from both electroactive redox and supporting species in solution. The contributions are by nature fundamental materials properties that add up all together to fix the decisive energy for a redox transfer. On most occasions, the required energy is supplied via external potentials (η) to an electrode. Undeniably, knowing the contributions from the individual energetic elements to the final makeup of the redox-level/required bias is critical to the development of new device systems. Design of new redox-active molecules are now being widely pursued, in which engineering of molecular energy level structure is a prime objective to control the extent and efficiency of electron transfer. Typically we resort to various spectroscopic methods that although expensive, are capable of producing an accurate energy level description. However, in the context of an electrochemical system design, this is barely the end of the story, since transport of electrons across an interface typically reorganizes the structure of a solvation shell around a redox-group. This calls for additional energy demand beyond that defined by a quantized molecular level structure. Therefore, it is essential to obtain the energetics of reorganization (λ) as a part of designing a system.

Ideally an appropriate understanding of energetic contributions to the requirement of ET would demand in-situ electrochemical characterization. While voltammetry is one of the simplest and most pursued method in electrochemistry to gain confirmation of transfer

events, it is surprisingly under-appreciated regarding its potential to generate information about the various energetic contributions in a system. A key reason behind this lack of pursuit emerges from the dominance of electron-transfer-kinetics in a redox-reaction (See Chapter 3). This is connected to the broadening of redox levels via reorganization energy λ in the presence of a solution (Figure 2.7, 2.9, 2.11). This is unique from the broadening in quantum transport[61] which is due to wavefunction overlap across an interface. The electrochemical broadening introduces a scan rate dependence (the extent of which depends on the width of broadening) such that reactants begin accepting/donating electrons at overpotentials much earlier than the formal redox potential/energy. As a consequence, the current peak always appears at a lower overpotential η than the actual redox energy level. This gives rise to the challenge in connecting redox energetics to an electrochemical response.

This work is aimed at overcoming this challenge and to show the versatility and strength of voltammetry in identifying the key individual energy components in an electrochemical environment. To that end, the entire work has been divided into three sections. In the first part, the energetic contribution from solution/electrolyte in an outer-sphere redox process has been analyzed. The contrast between the timescale of electron tunnelling and the timescale of an external observation (via applied scan rate) is identified as a key determinant of the properties of an electrochemical current *i.e.* peak potential, peak width etc. The understanding lays the foundation to suppress electron transfer kinetics via ultrafast voltammetry, which reveals the probability density structure of an electroactive redox energy level. This allows us to make qualitative and quantitative predictions regarding the reorganization energy of a system.

In part two, issues regarding ultrafast voltammetry and its impact on the formation characteristics of electric double layer in the presence of SAM has been discussed. The key

point of interest here is the extent of electrostatic screening by supporting ions to eliminate the potential drop inside a solution under nonequilibrium conditions. This is required to ensure conservation of redox energy levels in solution that can otherwise raise the energy demand for an electron transfer. The analysis is then extended into the recognition of faradaic component of a current profile in ultrafast voltammetry, which typically has a strong interference from non-faradaic charging current. This latter contribution drives the formation of double layer and has been studied in detail in the context of an electrode surface covered with SAMs to various degree. This is expected to aid in the design of SAM based electrochemical devices.

In the final section, the insights from the first two sections are combined to formulate a voltammetry based method to extract the energy level structure of a solvated molecule or nanoparticle. The method is then implemented along the lengths of a model armchair carbon nanotube system where the respective energy level structure at each tube length was extracted via voltammetry. This part of the work clarifies our understanding of the evolution of electrochemical charging from molecular and nanoparticle dimensions in terms of the extent of energetic contributions from the redox-active and supporting components in an electrochemical environment.

CHAPTER 3
Connecting Quantum Transport to Electrochemistry: A Theoretical Study of Redox-Active Monolayers

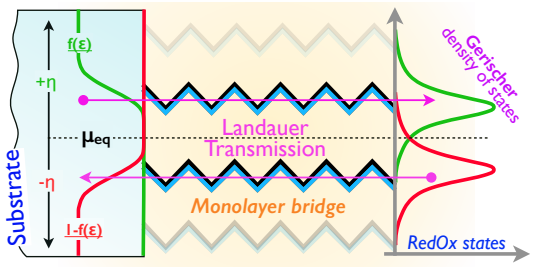

Tunnelling of electrons in a redox process at a metal-electrolyte interface is typically analyzed and captured with theories that are developed within the realm of electrochemistry. The kinetic theories such as those via equations 2.9 and 2.10 have been proven to be successful in representing countless outer-sphere processes. However, the unique nature of electron transfer in solid-liquid interfaces (such as reorganization, energy independence of coupling strength etc) has confined the application and evolution of such theories within the electrochemistry community alone. With an aim to expand the potential of such a theory, this work began with an attempt to view these theory from the angle of quantum transport. The outcome depicts a successful derivation[7] of electrochemical rate expressions on the basis of the Landauer's electron transport picture that is commonly used in quantum transport.

This method is utilized in this entire work to capture the response in linear sweep voltammetry. In this section, the method is applied to a model electrochemical tunnelling system consisting of a passivating monolayer (SAM) terminated by redox active groups. The key objective here is to explore the ultrafast scan rate regime and the consequent evolution in current profiles. Based on Gerischer's density of states formulation, electronic coupling independent current spectra are predicted which suggest an easy way to extract the redox reorganization energy. Moreover, two methods, based on voltammetric peak potentials and the degree of reaction completion, are examined as possible techniques to measure the electronic coupling between redox species and a substrate. In general, this work aims to further the translation of quantum transport derived electrochemical concepts into directly measurable electrochemical properties.

3.1 Introduction

In last few decades, the study of electron transfer (ET) between redox active monolayers and a conductive substrate has emerged as an intriguing field of research.[46,55–57,81] Interest has especially grown with respect to the development of electrochemical variants of molecular electronic systems where one of the attached contacts is replaced by an electroactive redox group.[17,46] Transport through these single contact molecular configurations displays electrochemical behavior to varying degrees[13,82–84] and has been identified as a controlling conduction mechanism in organic light emitting diodes, organic radical batteries, molecular photovoltaics, biosensor, actuator, and molecular motor applications.[20,85–87] In typical redox active monolayer systems such as that sketched in Figure 3.1a, the faradaic current may be engineered through two key controlling parameters: the degree of electronic tunneling[46,56,57,81] via the molecular bridge, which is directly connected to the strength of

coupling between the contact and redox-active group; and the nuclear reorganization energy of redox groups upon the loss or gain of an electron.[46,52] Therefore, one would identify tunneling probability and nuclear reorganization to be the key transport criteria of interest; and for a comprehensive understanding of such electron transport behaviour, it becomes incumbent on one to characterize and understand these electrochemical components. Although phenomenological theoretical descriptions exist in the literature for both electronic coupling and the reorganization energy,[8,9,88–93] experimental measurements are usually limited to methods such as various emission, absorption and fluorescence spectroscopic techniques[94,95], electron spin resonance measurements[96] and voltammetric techniques[97–100] from which information such as the stokes shift, peak potential, and rate constant are extracted. These are subsequently converted into reorganization and tunnelling parameters. In this work we propose that ultrafast voltammetry may also be utilized to extract both parameters.

While electrochemical transport is typically investigated within the Marcus-Hush formalism, in part I of this series[7] we derived similar heterogeneous electrochemical rate expressions within the Landauer picture via the non-equilibrium Green's function (NEGF) formalism. The Landauer picture has become the de facto method for analyzing electrical transport characteristics within molecular electronics,[101] thus its extension to electrochemical spectra stands out as an enormous opportunity to further understand the emergent electrochemical behavior in single contact molecular electronic systems.[20,85–87] Moreover, its direct extension to electrochemical properties via this work, also provides a crucial opportunity to further connect the diverse physics and chemistry communities that utilize the Landauer approach. By extending our quantum transport derived electrochemical rate model to capture current-overpotential characteristics, we show that the two aforementioned properties of interest can also be probed directly by taking advantage of advances

in ultrafast voltammetry[13,14,16,82,102,103] – which are able to reveal electron transfer and coupled chemical reaction information occurring at ultrashort timescales[102]. The suggested approach predicts unique current-overpotential spectra for a given reorganization energy that is qualitatively independent of electronic coupling. Overall, the predicted results are expected to have the potential to be directly translated into voltammetric experiments.

3.2 Method

To perform our voltammetric simulations, we employ the electrochemical transport formulation derived previously.[7] Utilizing the NEGF formalism within the Landauer quantum transport picture,[62,64] the following outer-sphere (tunneling) rate expressions were derived for electron transfer to (k_f) and from (k_b) reactants[7,52]

$$k_f = \frac{4\pi^2}{h}|M|^2 D_S \int f(\varepsilon) D_{ox}\, d\varepsilon \tag{3.1}$$

$$k_b = \frac{4\pi^2}{h}|M|^2 D_S \int [1 - f(\varepsilon)] D_{red}\, d\varepsilon\ , \tag{3.2}$$

where h represent Planck's constant, M is the coupling between the reactant and substrate, and D_S is the density of states (DOS) of the substrate as illustrated in Figure 3.1b. The electronic occupation in the substrate is given by the Fermi function $f(\varepsilon) = [1 + exp((\varepsilon - \mu_{eq})/k_B\mathcal{T})]^{-1}$, where μ_{eq} is the equilibrium electrochemical potential, k_B is Boltzmann's constant and $\mathcal{T}$ is the temperature. The quantities D_{ox} and D_{red} represent the Gerischer density of states distribution for reactants in either the oxidized or reduced state,[49–51] and are given by

$$D_{ox}(\varepsilon) = \frac{1}{\sqrt{4\pi\lambda k_B\mathcal{T}}} exp\left(\frac{-(\varepsilon - \varepsilon_{ox})^2}{4\lambda k_B\mathcal{T}}\right) \tag{3.3}$$

$$D_{red}(\varepsilon) = \frac{1}{\sqrt{4\pi\lambda k_B\mathcal{T}}} exp\left(\frac{-(\varepsilon - \varepsilon_{red})^2}{4\lambda k_B\mathcal{T}}\right) \tag{3.4}$$

where λ is the heterogeneous reorganization energy (for the sake of brevity we have dropped the heterogeneous subscript notation utilized in part I). The quantities ε_{ox} and ε_{red} represent the single particle oxidation and reduction energies of the reactants (as discussed in detail in part I).

To arrive at a current expression dependent on the applied overpotential (η), we need to consider that at any given instant the total current density (j) leaving the substrate is given by the surface concentration of oxidized (C_{ox}) and reduced (C_{red}) reactants multiplied by the forward and reverse reaction rates

$$\begin{aligned} j(\eta,t) = 4\pi^2 q \frac{|M|^2}{h} D_S \; [\; C_{ox}(t) \int f(\varepsilon+\eta)\; D_{ox}(\varepsilon)\; d\varepsilon \\ -\; C_{red}(t) \int (1-f(\varepsilon+\eta))\; D_{red}(\varepsilon)\; d\varepsilon \;], \end{aligned} \tag{3.5}$$

where the transfer rate multiplied by the charge q expresses the flow of current. The overpotential dependence η introduced in the Fermi distribution reflects the rising/lowering of substrate energy levels, with respect to that of the reactant, as an overpotential is applied. The potential is assumed to drop across the monolayer due to the very short screening length of the metal and the presence of a high supporting electrolyte concentration (typically utilized in electrochemical measurements) as depicted in Figure 3.1c. Here we also ignore diffusion kinetics amongst the reactants, since the redox active species are tethered to the monolayer chain at a fixed distance as illustrated in Figure 3.1a.

It is also important to note that a time dependence was introduced into the reactant concentration in equation 3.5. This time dependence follows from the fact that an oxidized reactant which accepts an electron will be converted into a reduced reactant ($Ox + e^- \rightarrow Red$), likewise a reduced reactant which gives up an electron will be converted into an oxidized reactant ($Red - e^- \rightarrow Ox$) – for further details see the discussion in part I. Thus at positive overpotentials the reduced reactant concentration grows at the expense of the

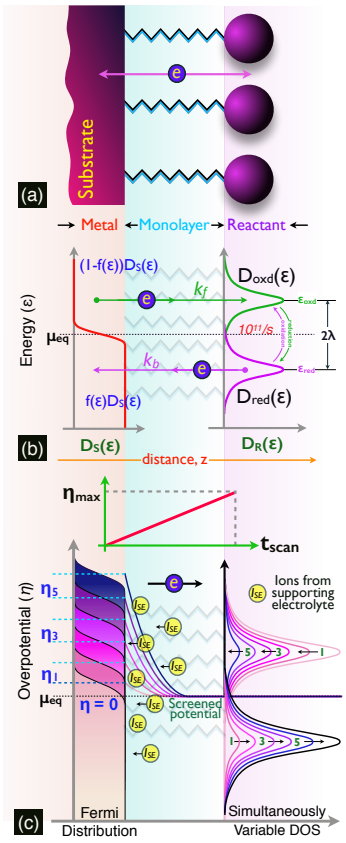

Figure 3.1: The charge transfer process for a redox capped monolayer. (a) Schematic configuration of contact-bridge-reactant system participating in electron transfer. (b) A linear sweep cathodic overpotential reduces the reactants (c) with the waveform shown on top, and thereby enforces the time dependent redistribution of unoccupied to occupied reactant states such that the total reactant coverage is conserved. A supporting electrolyte screens the contact potential, thus the reactant distribution remains fixed around reference potential (μ_{eq}). The process in (c) reverses when a negative overpotential is applied (not shown).

oxidized reactant concentration and vice versa for negative overpotentials (as illustrated in Figure 3.1c). However, the total species concentration ($C_{ox} + C_{red}$) remains conserved at all times. This approach towards reaction tracking means that two implicit subtle assumptions are therefore present in equation 3.5: (1) that electrons transfer while the

nuclei stand still (i.e. the Franck-Condon principle); (2) that the *rate* at which electrons are transferred between the substrate and reactants is much slower than the *rate* at which nuclei reorganize after a charge transfer event.

The supporting arguments behind the first assumption are outlined in part I of this series. However, the second assumption requires more discussion. The *rate* of electron transfer (k_f or k_b) can be paraphrased as: the inverse mean time between ET events. The mean time between transfer events differs from the transit time of an electron transfer. A single ET event is very rapid, while the mean time between subsequent ET events can be quite long (relatively speaking). This is analogous to the canonical low light concentration photodiode experiment, where the particle nature of light becomes apparent.[104] During such an experiment, each light particle rapidly traverses the space between the light source and the detector at the speed of light (extremely fast). However, at exceedingly low light intensity, the mean time between light detection events is long enough that it can be detected within the bounds of human perception (more than $1/20^{th}$ of a second). Analogously, in the case of electron transfer between the substrate and reactant, once a transfer event occurs: we assume there will be a "long time" before another transfer event occurs with the reactant and that the transfer event will be "very rapid". To define the electrochemical notion of a "long time", we refer to the timescales as perceived by the nuclei during the reorganization process, that typically occur in about 10^{-11} s.[52] Thus we are assuming that the rate of ET is much less than 10^{11} s^{-1} ($k_f \ll 10^{11}$ s^{-1} and $k_b \ll 10^{11}$ s^{-1}), such that nuclear reorganization inevitably occurs (99.9% of the time) before that reactant can again participate in an ET event as illustrated in Figure 3.1b.[25,52,105] Thus "very rapid" refers to the much shorter time scale of electron dynamics, as compared to the "long time" scale of nuclear dynamics;[52] therefore between each "very rapid" ET event there is a sufficiently "long time" for the nuclei to relax (see also part I in this series).

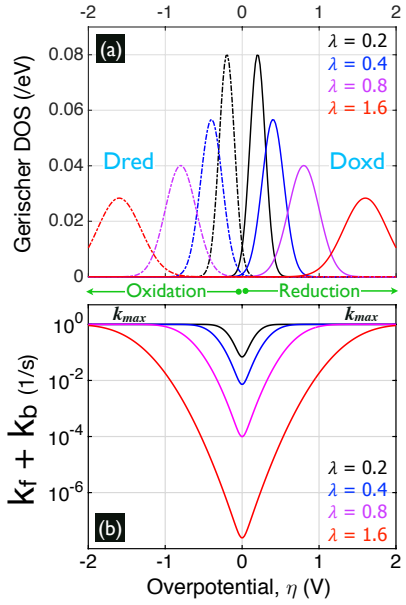

Figure 3.2: (a) Gerischer distribution of unoccupied (D_{ox}) and occupied (D_{red}) single reactant states for different reorganization energies (λ). (b) Overpotential variation in the redox rate constant ($k = k_f + k_b$) with $4\pi^2|M|^2/\ h = 1$ eV/s and D_S =1/eV.

In what follows, we apply this approach to linear sweep voltammetry (LSV) and discuss how it might be employed to interpret experimental measurements of quantities such as the reorganization energy (λ) and electronic coupling ($|M|$).

3.3 Results and Discussion

Let us begin our analysis by considering the impact of the reactant DOS energy dependent distribution upon the total ET rate ($k = k_f + k_b$) at a given η as illustrated in Figure 3.2a. This can be determined by introducing an overpotential dependence (η) into the Fermi distributions in equations 3.1 and 3.2, as was done in equation 3.5. Firstly, we note that the empty and filled single reactant DOS defined through equations 4.13 and 4.14 results in diminishing ET probabilities at any overpotential, as the reorganization energy becomes larger (see Figure 3.2a). Hence, since the substrate DOS (D_S) and the

coupling $|M|$ may be approximated as constants (see the discussion in part I), the reactant DOS distribution determines the bias dependence of the ET rate. At low cathodic biases ($\eta \to 0$), $\int d\varepsilon f(\varepsilon+\eta)D_{ox}(\varepsilon) \ll 1$; thus, the rate contribution of a single state is much less than one, thereby resulting in a low ET rate (relative to what is achieved at higher biases). Moreover, the low bias ET rate decreases relative to the high bias ET rates as λ increases – the same is true for anodic overpotentials. These trends are shown in Figure 3.2b. Both k_f and k_b increase with applied bias as more of the reactant DOS enters the bias window (as illustrated in Figure 3.1 and 3.2); reaching a maximum at overpotentials well in excess of λ and remaining constant thereafter. At high biases nearly the entire oxidized or reduced DOS contributes to ET, since for $|\eta| \gg \lambda$, we have $\int f(\varepsilon+\eta)D_{ox}(\varepsilon)d\varepsilon \approx 1$ or conversely, $\int [1-f(\varepsilon+\eta)]D_{red}(\varepsilon)d\varepsilon \approx 1$. This behavior agrees well with experimentally obtained $k\ vs\ \eta$ profiles for electron transfer between an Au substrate and various redox centre terminated monolayers[46,58,106].

3.3.1 Ultimate scan rate

Based on this maximum possible contribution from an individual reactant, one can define the absolute rate maximum as

$$k_{max} = 4\pi^2 q\ \frac{|M|^2}{h} D_S \Big[\int f(\varepsilon+\eta)\ D_{ox}(\varepsilon)d\varepsilon \Big]_{\eta \gg \lambda} \tag{3.6}$$

$$= 4\pi^2 q\ \frac{|M|^2}{h} D_S \Big[\int [1-f(\varepsilon+\eta)]\ D_{red}(\varepsilon)d\varepsilon \Big]_{\eta \ll -\lambda} \tag{3.7}$$

$$= 4\pi^2 q\ \frac{|M|^2}{h} D_S. \tag{3.8}$$

This is the electronic coupling dominated maximum rate with which tunneling may occur through an interface. Importantly, since k_{max} arises from the tunneling physics, it is *independent* of λ. Correspondingly, $t_{min} = 1/k_{max}$ may be defined as the "shortest" mean time between ET events at a given $|M|$. In LSV, one scans to a maximum bias η_{max} over a time

period t_{scan} (as shown in Figure 3.1), resulting in a scan rate of $R = \eta_{max}/t_{scan}$. Thus, setting $t_{scan} > t_{min}$ should drive a reaction to completion. This serves as an important voltammetric benchmark which we name the *ultimate scan rate*, $R_{ult} = \eta_{max}/t_{min}$, where $R_{ult}/\eta_{max} = k_{max}$. From this ultimate rate, experimentally observed voltammetric features can be directly related to what we term the *normalized scan rate*, $\alpha = R/R_{ult}$; *which is independent of the substrate-reactant coupling* $|M|$ *and depends only on the reorganization energy* λ. Thus observations for a given reactant species on identical substrates can be correlated across various monolayer thicknesses at various scan rates.

3.3.2 Calculation of reorganization energy λ

To better understand this physical chemistry, we examine the reduction of an ensemble of oxidized states as sketched in Figure 3.1c for different λ. At low biases, ET rates are much smaller than k_{max} as illustrated in Figure 3.2b; here, with slow scan rates ($\alpha \ll 1$), the time allowed for charge transfer is likely to match the time scale of low bias ET events. Hence, the reaction can consume all of the oxidized states within the scan time and the voltammogram consequently shows well defined peaks beyond which the faradaic current goes effectively to zero as shown in Figure 3.3(a-d)[i]. This has been observed and discussed in earlier literature.[14,56,81,106]. The bias dependent consumption of oxidized reactants is plotted in Figure 3.3(a-d)[iii], which shows a rapid fall in the oxidized reactant concentration for $\alpha \ll 1$ and a corresponding rise in the reduced state concentration. As the scan rate (α) is increased, less time is allotted for low bias ET events; thus, the current peak shifts towards higher overpotentials (see Figure 3.3(a-d)[i]) and further delays the full consumption of oxidized reactants (see Figure 3.3(a-d)[iii]). As α approaches 1, the scan time t_{scan} approaches t_{min} and therefore becomes too short to fully consume the reactants as shown in Figure 3.3(a-d)[iii]. Thus the current at $\eta = \eta_{max}$ does not go to zero

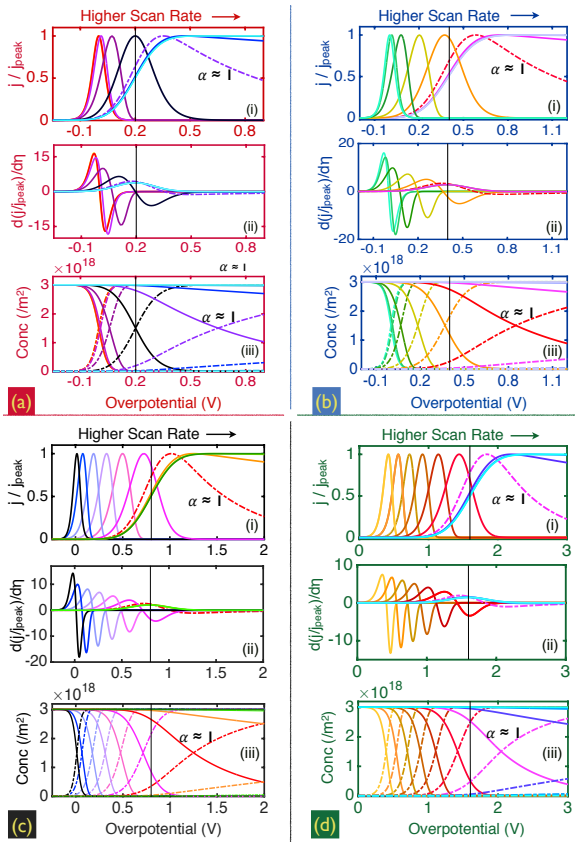

Figure 3.3: The figure is divided into four sections, each representing the transport characteristics of only the cathodic cycle for $\lambda = 0.2(a), 0.4(b), 0.8(c), 1.6(d)$ eV. The three subfigures in each section convey identical information for the corresponding reorganization energies. Figure (i) in each section shows the current densities (A/m^2) normalized by the respective peak currents. This is performed to fit all the waves within visible range. The normalized scan rate associated with each curve is such that $log(\alpha) = -6, -5, -4, -3, -2, -1, 0, 1, 2, 3$, with $log(\alpha) = 0$ being marked on spectrum (i) and (iii). Figure (ii) in all four sections shows the derivative of the current plot in part (i) and is critical to locating λ and extracting $|M|$. Part (iii) in sections [a-d] represent how the initial concentration $(3 \times 10^{18}/m^2)$ of oxidized reactants (solid line) diminishes while the reduced concentration (dot-dash line) grows with overpotential, as the sweep rate is varied. In all these plots the scan rates are increasing from left to right.

when $\alpha \geq 1$ and represents the reactant consumption over a wide bias range through peak broadening as shown in Figure 3.3(a-d)(i). These voltammetric trends have been frequently

reported in the literature[8,14,16,103,106,107]. Once the scan rate R is made significantly greater than R_{ult}, we are in the regime of $\alpha \gg 1$, where very little time ($t_{scan} \ll t_{min}$) is provided for the reactant consumption as in Figure 3.3(a-d)[iii]. As a result, the voltammetric curves become progressively more asymptotic and eventually settle towards a limiting, flat plateau as shown in Figure 3.3(a-d)[i].

However, once the transition to a plateaued response occurs, increasing the scan rate further does not result in any further shift of the current profile towards higher overpotentials. This, in turn, reiterates the dependence of the high scan rate ($R \gg R_{ult}$) current profile on the energetic distribution of oxidized and reduced states [equations 4.13 and 4.14], that are only functions of the reorganization energy λ. Interestingly, these normalized current profiles were found to be independent of the strength of interfacial coupling between the participating states. Although the absolute peak current is expected to rise with stronger coupling, the results in Figure 3.3(a-d)[i] suggests that the peak position should remain unaffected.

Importantly, the limiting flat plateau profile ($\alpha \gg 1$) mentioned above provides an alternate approach for measuring the reactant reorganization energy λ and is, to our knowledge, a unique prediction arising from this quantum transport based approach. We argue that the overpotential corresponding to the half maximum in the positive trending slope of a plateauing voltammetric curve, as shown in Figure 3.3(a-d)[i], corresponds to λ. This is better exposed in the derivatives of Figure 3.3(a-d)[i] as plotted in Figure 3.3(a-d)[ii], in which the position of the aforementioned half maximum appears as a single peak. At low scan rates ($\alpha \ll 1$) a double peak appears in Figure 3.3(a-d)[i] due to the completion of the reaction. Thus, this "single peak" feature is feasible only at high normalized scan rates ($\alpha \gg 1$) where reactants are only marginally reduced, such that the current primarily depends on the reactant DOS (D_R) localized within the bias window. This means, there

is virtually no time dependence in C_{red} and C_{ox} when $R \gg R_{ult}$; thus, at $\alpha \gg 1$, the derivative of voltammetric curves reveal information regarding the profile of D_R and the reactant reorganization energy λ.

Experimental measurements of the faradaic response at high scan rates as shown in Figure 3.3, would likely be impeded by interference from the charging current and ohmic drop distortions. However, these complications can be alleviated by using ultra/microelectrodes[11,76,108] and employing Amatore's online ohmic drop compensation method.[103] Moreover, the upper bound of achievable scan rates currently reported lie in the low megavolt per second (MV/s) range.[13,14,102] This limits the choice of monolayers for which $R \gg R_{ult}$ or $t_{scan} \ll t_{min}$ and hence plateaued voltammetric curves might be achieved, since $t_{min} = h/4\pi^2 q\ D_S|M|^2$. Assuming $\eta_{max} \approx 1$ V to achieve a plateauing profile, a reasonable lower bound on the achievable scan time would be $t_{scan} = 1\ V/(1(MV/s)) = 1\ \mu s$. This, in turn, places an approximate upper bound $|M|_{max}$ on the monolayer coupling for which λ might be observed in this manner via $|M|_{max} = \sqrt{\hbar/2\pi q D_S\ t_{scan}} \approx 10^{-5}$ eV. With stronger coupling $|M| \gg |M|_{max}$, the ET rate exceeds that achievable with modern instrumentation, hence it becomes largely theoretical to argue in terms of scan rates achieving $R \gg R_{ult}$.

3.3.3 Determination of coupling strength $|M|$

Thus the nature and thickness of monolayer dictate our ability to measure λ as predicted in Figure 3.3. This holds because $|M|$ decays exponentially with the monolayer thickness and it decays with increasing tunneling barrier height[52,63]. The tunneling barrier height is controlled by the chemical makeup of the monolayer, that is the HOMO-LUMO gap.[63] Lower tunneling barriers are often exhibited by π-conjugated monolayers,[56–58,81,106] whereas higher tunneling barriers are often provided by alkane monolayers.[109] Indeed,

weak coupling $|M| \approx 10^{-6}$ eV has been reported in redox terminated alkane monolayers on $Au(111)$.[46] Therefore, one would ideally choose *long chain alkane* monolayers for measuring λ. For short chain and/or π-conjugated monolayers, even MV/s might not be fast enough to enter the plateaued voltammetric regime shown in Figure 3.3(a-d)[i] in order to characterize for λ and $|M|$.

Since substrate-reactant coupling ($|M|$) through the monolayer has such a significant role in determining the measured voltammetric characteristics, let us further examine how $|M|$ might also be measured. One possible method is to plot the voltammetric peak potentials (η_{peak}) at different scan rates (R).[8,9] Here, we can make use of the absolute scan rate (R), rather than the normalized one (α), since the R_{ult} shifts with different values of $|M|$ and so do the observed η_{peak}. In general, a plot of η_{peak} *vs* R shifts from left to right as $|M|$ increases. For different λ, these plots ranging from very weak to strong coupling are presented in Figure 3.4(a-d)[i]. It can be seen that for all $|M|$, the peak position rises rapidly at first followed by a levelling-off at higher scan rates as the system enters the plateaued region, where the peak position effectively becomes constant. As discussed above, with MV/s scan rates, such behavior is only likely for $|M| \approx 10^{-5}$ eV or less. In general, such diagrams can be compared with experimental measurements to estimate the value of $|M|$.

Figure 3.4(a-d)[ii] presents an alternate method for determining the effective coupling strength $|M|$ from voltammetric data. Besides resolving the λ, the derivatives in Figure 3.3[ii](a-d) also provide an intuitive perspective regarding the degree to which the redox process is complete. Importantly, the integral of the derivative approaches zero at $\alpha \ll 1$. This observation is consistent with the understanding that the reaction is very likely to complete at such low sweep rates with negligible quantity of reactants left (as shown in Figure 3.3(a-d)[i,iii]). Therefore, one can perceive this integral as a rough measure of the

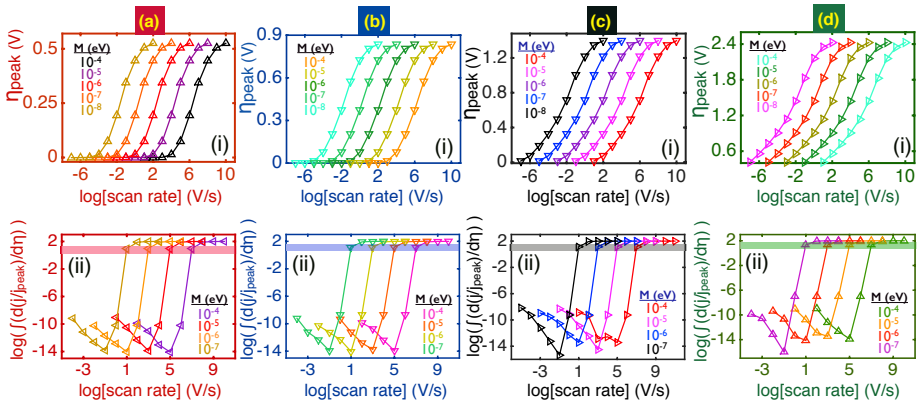

Figure 3.4: Calculation of $|M|$ presented as in Figure 3.3 for $\lambda = 0.2(a), 0.4(b), 0.8(c), 1.6(d)$ eV. Plot (a-d)[i] shows the current peak potentials collected from corresponding $j-\eta$ plots in 3.3(a-d)[i] for different scan rates. As $|M|$ changes (listed), the curves slide into higher or lower scan rates accordingly. Finally, part (ii) in each plots takes the sum of the respective derivatives produced in part (ii) of 3.3 for different scan rates. Multiple plots in each individual part depict calculations with different $|M|$ (values enlisted). The horizontal color band on each plot spots the approximate position of the ultimate scan rate R_{ult} at the intersection of each curve.

degree to which the reaction is able to complete at a particular scan rate. As shown in Figure 3.4(a-d)[ii], a sudden upsurge appears in the derivative (from Figure 3.3[ii]) integral that lifts the percentage of remaining reactants by orders of magnitude from near zero to a non-trivial $\sim 10-20\%$. We have calculated that the scan rate associated to this sudden rise corresponds very well with the ultimate scan rate, R_{ult}. The coupling strength then can be estimated from R_{ult} via

$$|M| = \sqrt{\frac{\hbar R_{ult}}{2\pi q\ D_S \eta_{scan}}}$$

However, as discussed above for λ measurements, it would be challenging to apply this method to "strongly" coupled systems where R_{ult} lies above the MV/s range.

3.4 Conclusion

In conclusion, an electrochemical rate model derived within the Landauer picture in part I of this series, was further employed to study ET in a bridge mediated redox system. Under an applied bias, the method was determined to be inherently time dependent through the adjustment of oxidized and reduced species concentrations following each ET event. It was then applied to study redox reactions across a monolayer bridge atop a metallic substrate, where an intuitive normalized scan rate representation was developed based on a reorganization energy (λ) independent coupling parameter, denoted as the ultimate scan rate. From this, experimentally accessible voltammograms were predicted to exhibit plateaus at sufficiently high scan rates and at reactant-substrate couplings of 10^{-5} eV or less, from which reactant reorganization energies may be directly measured. Lastly, it was further shown that this coupling value could be extracted by plotting either the normalized peak overpotential versus scan rate,[8,9] or the degree to which the reaction has run to completion versus overpotential. It is likely that this approach is only valid in the weak coupling regime; that is, on time scales where the ET rate is much less than the nuclear reorganization rate.

We would like to point out that all of these results presented herein have made use of simplified rate expressions as given by equations 3.1 and 3.2. However, quantum transport calculations are amenable to the sophisticated NEGF matrix formalism by which these trends might be further explored through sophisticated single-particle Hamiltonians – e.g. via first-principles methods.[63] Though we have not made full use of this matrix formalism here, it offers a fascinating avenue for future research for the further extension quantum transport methods and concepts within electrochemistry.

Although, the suggested technique in this chapter offers a promising avenue, a critical assumption was made at the beginning of this work - whereby it was stated that an applied

overpotential would be fully screened at the position of a redox group (Figure 3.1c). As discussed in Chapter 2, the issue of screening needs to be addressed as an integral part of interfacial activities during ultrafast measurements. In general, the nature of solution and the surface coverage by monolayers play a critical role to the extent and rate at which screening can be achieved. These aspects are thoroughly analyzed in the next chapter.

CHAPTER 4
Interfacial Screening in Ultrafast Voltammetry: A Theoretical Study of Redox-Active Monolayers

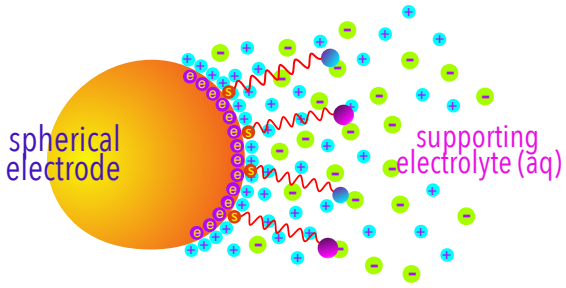

In the preceding discussion, the extraction of a localized electroactive level in solution has been given a theoretical formulation on the basis of overpotential scan rates at ultrafast regime. This analysis has been solely centred around faradaic response that represents the current due to electron transfer. In this section the focus is shifted to the non-faradaic component, which arises from the ionic transport bound within solution and occurs simultaneously with the faradaic transfers. The significance of this current is discussed in the context of interfacial screening, which typically is overlooked at low scan rate regime. At ultrafast scan regime however, as addressed in a large part of this thesis, potential screening of interface can no way be ignored. The small time (∼nanosecond) available in this regime firstly challenges the achievement of the desired screening that can raise the energy

demand for an electron transfer. Secondly, it produces a high charging current that can undermine the accompanying faradaic response.

In this chapter, the impact of interfacial screening on electron transfer (ET) at ultrashort timescales is theoretically investigated on redox active monolayers by linear sweep voltammetry (LSV). The charging current associated with the nanosecond screening process is an important experimental determinant in finding both the reorganization energy (λ) and electronic coupling ($|M|$) through ultrafast methods. On the one hand, time dependent decay of the charging current mitigates its impact on the current contribution from faradaic processes; while on the other hand, allowing substantial decay translates into a reduced upper-bound of applicable scan rates – which are crucial for ultrafast characterization. Analysis of the decay in the charging current suggests that the desired screening may be achieved for relatively weakly coupled systems within the charging time constant. For weakly coupled systems, the scan rate corresponding to nanoscale charging time constants appears to be suitable for the ultrafast investigation of ET characteristics. Moreover, the level of screening achieved at nanosecond decay times is shown to change with the coverage of electrode surface by monolayers; which appears to be accompanied by sharp drops in the time constant during successive saturation of interfacial layers by supporting ions. These observations are expected to help design electrochemical device systems with interfaces capable of high faradaic efficiency at ultrafast limits.

4.1 Introduction

Electrochemistry nowadays is an integral part of many electronic devices, especially in energy storage applications and emerging sensing technologies[110–112]. Devices such as supercapacitors[113], store energy through the formation of an electric double layer (EDL) at the solid liquid interface with no significant physical changes to the electrodes[113]. A typical

battery, on the other hand, may go through electrochemically driven structural changes during its charge-discharge cycles. An exception to this trend can be found in recently developed organic radical batteries (ORB)[20,66,114] where electrons were shown to be stored in redox active polymers assembled on a metallic substrate. Besides structural stability, an exciting feature recognized in systems with polymer mediated redox transport is the orders of magnitude higher rate constants for both heterogenous and homogenous electron transfer (ET) processes - as reported in PTMA (poly(2,2,6,6-tetramethylpiperidenyloxy-4-ylmethacrylate)) based ORB[20], when compared to conventional cathode systems[115]; this makes them potentially suitable for high power density storage applications. In fact, conventional cathodes hybridized with radical monolayers were shown to improve their pulse power performance by an order of magnitude[32]. Variants of this configuration have been applied in organic radical based capacitors, memristors, photovoltaics, light emitting diodes and biosensors[20,85,87]. Generally the extent of faradaic transport, and therefore the charge storage properties in these redox-active systems are tuneable on the basis of the characteristics of the chosen monolayer as well as of the radical group. However, the exact physicochemical parameters influencing the performance of these technologies are not well understood. Typically, a monolayer functionalized with redox groups provide an ideal model system to study the fundamental interfacial charge transfer properties of these technologies.[20,46,75,107] While the tunnelling across the interface is controlled by the electronic coupling $|M|$ of the monolayer bridge, the availability of localized redox states for electronic occupation mainly depends on its reorganization energy λ. Therefore, it is essential to understand and evaluate these two parameters as well as the redox potential of the molecule relative to the unbiased Fermi level in the metal in order to determine the faradaic efficiency of the overall transport process in such systems.

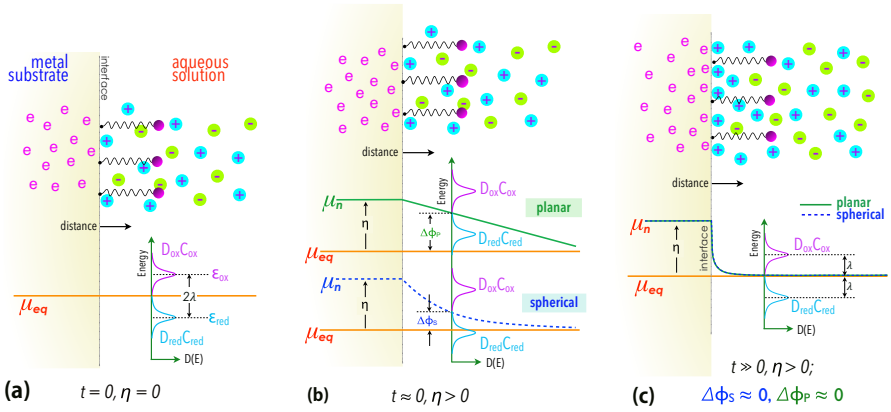

Figure 4.1: Mechanism of the screening process in time. (a) A general equilibrium exists at zero bias with a uniform electrochemical potential μ_{eq} across the interface. The oxidized ($D_{ox}C_{ox}$) and reduced states ($D_{red}C_{red}$) are separated by 2λ [24–26]. (b) When an overpotential is applied ($\eta > 0$), the redistribution of the system potential at femtosecond time scales causes it to drop over a long distance into the solution due to lack of screening at this timescale. This drop is linear in planar electrodes and has a $1/r$ dependence in spherical electrodes, where r is the distance from spherical surface. The excess potential energy in the solution shifts the redox-molecular states up by $\Delta\phi_s$ and $\Delta\phi_p$ for spherical and planar electrodes respectively. The supporting ions distribution shown on top remains almost unaltered. (c) In time, however, these supporting ions screen the potential and can return the redox states to their original position. The extent of screening during fast scanning can depend strongly on the percentage of surface coverage by the assembled monolayers as they dictate the available passage area for the migrating ions. While the molecular states localized on the redox groups can accept (ε_{ox}) and donate (ε_{red}) electrons, the charge transfer efficiency also relies on the relative magnitude of C_{ox} and C_{red}, the sum of which must remain conserved at all times. The reorganization energy λ is considered to be equal for oxidation and reduction.

On the basis of Marcus expressions for the heterogenous electron-transfer rate constant [116,117], we recently reported the possibility of measuring these two parameters $|M|$ and λ in redox active monolayer systems using ultrafast linear sweep voltammetry (LSV) [118]. At such high scan rates, especially above ~ 10 KV/s [65], it is necessary to efficiently screen the electrode potential at the location of redox states to inhibit any shift of their energy levels as shown in Figure 4.1. Such shifts in redox levels may also arise due to time-dependent

charge accumulation on the redox-centers via the faradaic process under applied biases. These shifts can introduce an error[117] into the characterization of λ via ultrafast LSV. In this regime, the interfacial screening process is accompanied by a considerable non-faradaic current which appears as an addendum to the ET current in a voltammogram. This is called the charging current and is known to decay exponentially in time[1]. This decay is illustrated in Figure 4.2b that appears repeatedly in response to each microscopic step (η_{step}) within the ultrafast LSV scheme as shown in Figure 4.2a. The short timescale of operation at every η_{step} restricts the decay and can result in a high charging current contribution to the total current. As a result, the extraction of analyzable faradaic features from a voltammogram becomes challenging. While techniques were suggested in order to record charging free voltammograms[65,103], the level of screening achieved therein with respect to both applied overpotential and faradaic charge accumulation remains unidentified and yet to be investigated, which is essential to accurately characterize the redox energetics as illustrated in Figure 4.1.

While ultrafast LSV, apart from experimental preparation, could be a quicker way[118] of characterizing electronic coupling and reorganization energy over other available methods proposed on the basis of experiments with a step potential scheme[46] and/or through an analysis of voltammetric peaks[116,117], it would still require proper screening of the interface to ensure the redox states conservation. The time required for screening usually depends on the diffusivity of mobile ions and the permittivity of the electrolyte. Enforcing any screening criteria therefore leads to an upper bound of applicable scan rates for a system when characterizing redox energetics via LSV. However, high scan rates may prevent the charging current as shown in Figure 4.2b from decaying to the desired level, which in turn can partially compromise the validity of the technique by concealing the faradaic features in part or in whole. The accuracy of this method therefore could be enhanced through

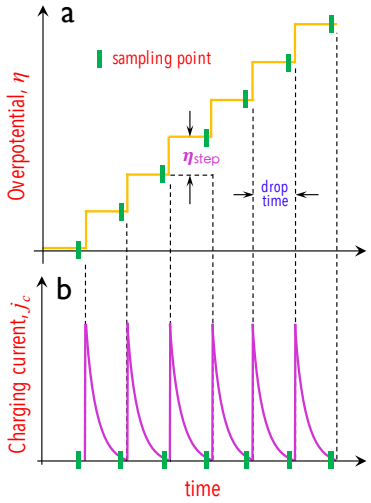

Figure 4.2: Microscopic view of an ultrafast LSV scheme (a) and the resulting charging current (b). The current in the final voltammogram consists of the currents sampled near the end of each pulse, with low charging current contribution.

proper control of the charging current, in order to satisfy the screening conditions as well as to be able to extract meaningful faradaic information.

Moreover, electron transfer efficiency at ultrafast scan rates may be hampered by the shift of molecular energy levels arising from an unscreened potential dropping long after the redox-active groups as illustrated in Figure 4.1a,b or due to the unscreened excess local potential following the build up of faradaic charges. Depending on the time allowed and the diffusivity of the supporting electrolyte, these shifts may be minimized through charging the interface according to the mechanism suggested in Figure 4.1. In addition, screening of the faradaic charges by localization of supporting ions near the redox-centers may be undermined by the drift of the supporting ions towards the surface due to strong interfacial electric field. The charging process becomes even more complicated if the monolayer coverage on the metal surface is densely packed. Under these circumstances, ion migration and

accumulation during charging may be limited, resulting in poor screening, a wide potential drop, and error prone characterization of λ and $|M|$.

In this chapter, we provide a semi-classical physical model of the role played by interfacial screening during electron transfer processes based on a numerical solution of drift-diffusion equations. Utilizing this model we simulate ultrafast LSV in single contact redox-active monolayers deposited on a metal nanoelectrode in an aqueous electrolyte. In a given solution, although the properties of charging current may vary with the electronic coupling $|M|$ under the given nature of electron donors/acceptors in solution, the faradaic component does show a definite quadratic dependence on it. From this, we show that controlled decay of the charging current to a desired magnitude can result in faradaic relative contribution to the total current to an extent that favourably exposes the ET features (that are λ and $|M|$) in an ultrafast voltammogram. Moreover, for dense monolayer coverages, analyses of the charging current decay behaviour suggest a drop in time constants upon saturation of subsequent interfacial layers by ionic accumulation during the course of screening. We examine these issues in order to validate previously made predictions regarding ultrafast redox characterization[118] as well as to understand the effect of screening on the efficiency of ET in the presence of solution dynamics.

4.2 Method

We consider a 1D spherical model of a single contact electrochemical system with a nanoelectrode of radius r_0 contained in an aqueous electrolyte solution of singly charged positive and negative supporting ions. The equilibrium concentration distribution of these mobile positive and negative ions between the surface ($r = r_0$) and solution bulk ($r \to \infty$) are C^+ and C^- respectively. In addition, with each hydrocarbon in the monolayer is terminated by a single redox group, we assume a minimum uniform coverage of 3 hydrocarbon

chains grown per nm^2 area of the nanoelectrode surface. For an Au electrode, this corresponds to $\sim 20\%$ occupation of the total surface area which leaves the rest of the surface for supporting ion diffusion and migration in response to an applied overpotential. The positive and negative ion flux due to this coupled migration and diffusion can be written as

$$J_{C^+}(r) = qD^+\nabla C^+(r) - qu^+C^+(r)\nabla\phi(r) \tag{4.1}$$

$$J_{C^-}(r) = qD^-\nabla C^-(r) + qu^-C^-(r)\nabla\phi(r) \tag{4.2}$$

respectively. Here, q is the unit charge; D^+ and u^+ are the diffusion constant and mobility of the positive ions, D^- and u^- express the same for the negative ions and $\phi(r)$ is the potential distribution across the system. $J_{C^+}(r)$ and $J_{C^-}(r)$ are the respective ionic currents. The redistribution of C^+ and C^- due to the spherical flux can be found using the continuity equations

$$q\frac{\partial C^+(r)}{\partial t} = \frac{1}{r^2}\ \nabla\cdot(r^2\ J_{C^+}(r)) \tag{4.3}$$

$$q\frac{\partial C^-(r)}{\partial t} = \frac{1}{r^2}\ \nabla\cdot(r^2\ J_{C^-}(r)) \tag{4.4}$$

for positive and negative ions respectively. The changes in these profiles predominantly appear at the interfacial region in accordance to the strongest electric field through equations 4.1 and 4.2. This ionic rearrangement triggers an extremely rapid screening response in the metal causing accumulation or depletion of electrons at the surface. We note that the timescale of electron screening in the metal is orders of magnitude faster than the timescale of ionic drift-diffusion. Following the Gummel method[119], the adjustment in the electronic concentration profile $n(r)$ and the associated potential $\phi(r)$ across the system, with the fixed concentration of static metal ion-cores $N_{ic}(r)$ and mobile supporting ions $C^+(r)$ and $C^-(r)$ in solution, was calculated iteratively via solution of 1D spherical poisson's equation

$$-\epsilon_r\epsilon_0 \frac{1}{r^2}\nabla \cdot (r^2 \nabla \cdot \phi(r)) = q\left(n(r) - N_{ic}(r) + C^-(r) - C^+(r) + n_f(r_0 + \delta)\right) \tag{4.5}$$

in conjunction with electron concentration distribution given by

$$n(r) = n_i \; exp\left(\frac{\phi(r)}{k_B \mathcal{T}}\right). \tag{4.6}$$

Here, ϵ_0 is the permittivity of vacuum, ϵ_r is the dielectric constant of solution, k_B Boltzmann's constant, and $\mathcal{T}$ the temperature. Here $n_f(r_0 + \delta)$ is the time dependent concentration of the charge transferred to or from the redox groups during the faradaic process via a monolayer of length δ. The parameter n_i is phenomenological and is utilized to capture the density of electrons in a metal, in a manner that can be implemented to capture metallic screening using the Poisson-Boltzmann statistics within the Gummel framework; while in the liquid region n_i is set to an infinitesimally small value to reflect the absence of free charge carriers. While the analyses presented here are principally for spherical transport dynamics, comparative analyses with planar electrodes were also included as deemed appropriate. For planar electrodes, the radial dependence in equations 4.3-4.5 were replaced with the respective linear forms. Although the discussion surrounding the spherical transport dynamics may hold for electrodes with radius up to a few micrometers[76], from an experimental point of view, one may prefer nanoelectrodes that can ensure a lower charging current over larger spherical dimensions – which as discussed later, is critical to extracting faradaic features from ultrafast voltammograms. Above micrometers, the electrode curvature may not be high enough to consider the solution dynamics to be spherical and one enters into the planar dynamics regime. Continuing with the spherical representation, the electron concentration is fixed to its equilibrium level defined by the electrochemical potential at the interface ($r = r_0$), such that for an applied overpotential

η the boundary conditions are

$$\phi(r = 0) = \eta \tag{4.7}$$

$$\phi(r \gg r_0) = 0. \tag{4.8}$$

The interface blocks the mobile ions completely and therefore

$$J_{C^+}(r \leq r_0) = 0 \quad \text{and} \quad J_{C^-}(r \leq r_0) = 0. \tag{4.9}$$

The charging current density j_c was calculated from the change in the total electron concentration $dn(t, r)$ in the metal with respect to time,

$$j_c(\eta, t) = q \int_0^{r_0} \frac{dn(t, r)}{dt} dr. \tag{4.10}$$

Electron transfer to/from the redox-active groups occurs in parallel with the charging process where the rates of reduction and oxidation can be written as[52,53]

$$k_{red} = 4\pi^2 \frac{|M|^2}{h} D_S \int f(\varepsilon + \eta)\ D_{ox}(\varepsilon)\ d\varepsilon, \quad \text{and} \tag{4.11}$$

$$k_{ox} = 4\pi^2 \frac{|M|^2}{h} D_S \int (1 - f(\varepsilon + \eta))\ D_{red}(\varepsilon)\ d\varepsilon \tag{4.12}$$

respectively. Here, $|M|$ is the electronic coupling between contact and redox group via the monolayer, h represents Planck's constant, D_S is the metal density of states. The Fermi distribution in the metal is given by $f(\varepsilon) = [1 + exp((\varepsilon - \mu_{eq})/k_B\mathcal{T})]^{-1}$, where μ_{eq} is the equilibrium electrochemical potential. The Gerischer density of states distribution for oxidized and reduced states are expressed by D_{ox} and D_{red}, respectively, and are functions of heterogenous reorganization energy λ and single particle oxidation (ε_{ox}) and reduction

(ε_{red}) energies of the corresponding reactants[49–51]. These are given by

$$D_{ox}(\varepsilon) = \frac{1}{\sqrt{4\pi\lambda k_B \mathcal{T}}} exp\left(\frac{-(\varepsilon - \varepsilon_{ox})^2}{4\lambda k_B \mathcal{T}}\right) \tag{4.13}$$

$$D_{red}(\varepsilon) = \frac{1}{\sqrt{4\pi\lambda k_B \mathcal{T}}} exp\left(\frac{-(\varepsilon - \varepsilon_{red})^2}{4\lambda k_B \mathcal{T}}\right) \tag{4.14}$$

and are schematically presented in Figure 4.1. The above rate expressions were also derived using a quantum transport based approach in previous work[7,118]. The integrals in equations 4.11 and 4.12 represent the fractions of the respective single states D_{ox} and D_{red} activated for the electron transfer by an overpotential of η. This active fraction becomes the total number of effective states for ET when multiplied by the available concentration of oxidized ($C_{ox}(t)$) and reduced ($C_{red}(t)$) species terminating at the monolayer end as shown in Figure 4.1. As mentioned earlier, for 20% surface coverage the initial concentration $C_{ox}(0)$ can be $\sim 3 \times 10^{14}/\text{cm}^2$. Therefore, during a reduction cycle, the number of electrons transferred to a redox molecule over a time step of dt is $N_{red} = k_{red} \times C_{ox}(t) \times dt$; which leads to a loss of the concentration of total oxidized states from $C_{ox}(t)$ to $(C_{oxd}(t) - N_{red})$ while a simultaneous growth in the reduced species concentration from $C_{red}(t)$ to $(C_{red}(t) + N_{red})$[118]. The size of the time step dt is the same that arises during the calculation of charging current in equation 4.10. The process reverses during the oxidation cycle, when the number of electrons transferred from the redox molecule to the metal is obtained via $N_{ox} = k_{ox} \times C_{red}(t) \times dt$. This in consequence drops the concentration of reduced species from $C_{red}(t)$ to $(C_{red}(t) - N_{ox})$ and raises the oxidized states concentration simultaneously from $C_{ox}(t)$ to $(C_{ox}(t) + N_{ox})$[118]. We note that, the faradaic concentration term n_f in equation 4.5 corresponds directly to the concentration of the final state of the reaction – which is $C_{red}(t)$ during the reduction process and $C_{ox}(t)$ during the oxidation process. The shifts in the number concentrations of various species during this faradaic process give rise to the faradaic current density that can be calculated at each time step using the general

relation

$$j_{et}(\eta, t) = q\left(\frac{N_{ox} - N_{red}}{dt}\right) \tag{4.15}$$

The total current as observed in voltammetry can be obtained by adding the charging (equation 4.10) and faradaic (equation 4.15) components

$$j(\eta, t) = j_c(\eta, t) + j_{et}(\eta, t). \tag{4.16}$$

While different approaches to handle the formation of screening layers at nanoelectrode-liquid interfaces have been suggested,[120–124] they are primarily focused on understanding the capacitive issues, mostly of the pristine crystalline interface region - from which it is not clear whether the proposed screening characteristics would hold for intercalated screening within monolayers. Any detailed structural formulation and issues regarding their stability in the monolayer system that we are investigating would require further experimental and theoretical work. For now, the drift-diffusion method described here is utilized to capture the general physics and explore the role of interface charging on electrochemical characterization of monolayer bound redox groups.

4.3 Results and Discussion

Equations 4.1-4.6 were solved numerically with an iterative procedure using the boundary conditions in equations 4.7,4.8 to achieve self-consistency. Once the potential $\phi(r)$ was determined, a new $C^+(r)$ and $C^-(r)$ were calculated using backward difference for the time derivative with a time step limited by the Courant condition.[125] This process was repeated throughout the calculation until the desired drop in the charging current and the necessary screening level were achieved. To capture the screening process, the electron transfer distance, roughly equal to monolayer length δ, was fixed at 1.5 nm from the metal

surface – although smaller distances were also investigated and are presented later in this discussion. The required screening at any applied scan rate and overpotential was set to conform with the condition $|\phi(r = r_0+\delta)-\phi(r \gg r_0)|< 10$ mV as illustrated in Figure 4.1. This was enforced to limit the shift in redox-active states situated at $r \approx r_0+\delta$ as much as possible. However, because of the faradaic charge evolution in time, this limit was allowed to rise at high overpotentials ($\eta > \lambda$) - while a consistent level of decay in charging current was maintained in order to achieve the highest possible scan rates. During the slow scan rate simulations, this condition was more relaxed. Under non-equilibrium, these objectives are typically achieved by the drift and diffusion of supporting ions in the solution near the interface which leads to the formation of an EDL that in time grows by continuous charging at a given potential.

The magnitude of current arising from the charging process is a function of time. In typical ultrafast voltammetry, the time allowed for interfacial processes can be μs/V or even less. Such short time scales inhibit the suggested decay of the charging current in Figure 4.2b at each η_{step}. As a result, the charging current can dominate the total current density upon sampling at the end of each overpotential step. On the other hand, the magnitude of ET (faradaic) current primarily relies on the coupling ($|M|$) of the bridging monolayer as in equation 4.15. With a strongly coupled monolayer, the ET current generated may be comparable to the charging component which can produce observable faradaic features in voltammetry. However, for a weakly coupled system, the ET current may be so low that the total current is dominated by the charging component. To extract analyzable faradaic features from experimentally obtained current-overpotential data, one must therefore understand the dynamic variation of coupled charging and electron transfer processes at different scan rates.

4.3.1 Properties of the charging current.

We begin our analysis by simulating LSV applied to redox-active monolayers grown on an Au nanoelectrode at 20% surface coverage in 1 M aqueous solution of NaCl. Before going into an analysis of the simultaneous charging and faradaic processes present within a voltammogram, let us first consider a scenario where there are no faradaic activities in this system to better understand the physics of the charging current. Hence we are left to deal with only the interface screening which is independent of the monolayer characteristics λ and $|M|$. Since the charging current is associated with the screening process as discussed earlier, we examine the average decay behaviour of the charging current j_c along a forward cathodic scanning step as illustrated in Figure 4.2. This was calculated for both spherical and planar electrodes and the results are presented in Figure 4.3. Employing a single $\eta_{step} = 10$ mV step according to the scheme in Figure 4.2, we calculated tenfold difference in RC time constants between spherical (τ_s) and planar (τ_p) transport geometries (the results are compared in Figure 4.3a,b). Moreover, the study suggests almost an order of magnitude higher initial charging current density in planar dynamics. In contrast, a lower time constant and lower initial charging current density in spherical electrode systems leads to a reduced charging contribution compared to systems with planar electrodes. The difference between τ_s and τ_p readily suggests that for the given 1 M NaCl solution, the achievable scan rates with radial diffusion dynamics can be at least one order of magnitude higher than that possible by linear dynamics on planar surfaces. In addition, the decay behaviour during continuous charging over the course of voltammetry shows a dependence on the packing density of redox-monolayers on the electrode surface. This is discussed next.

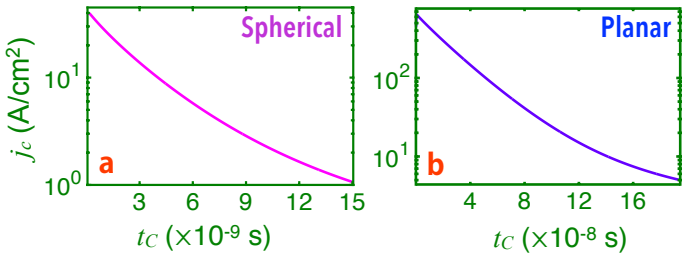

Figure 4.3: Average decay behaviour at fixed cathodic overpotential in spherical (a) and planar (b) electrode systems, for a single $\eta_{step} = 10$ mV voltage step.

4.3.2 Effect of variation in surface coverage on electron transfer.

During the screening process, electrostatic attraction draws the supporting ions towards the surface where they occupy the available sites. If the coverage is varied by changing the concentration of monolayers (of identical characteristics) on electrode surface, the space for ion migration and occupation changes accordingly as implied in Figure 4.1. This may influence the extent of screening by imposing a maximum on the number of migrated ions that can pack into an ion layer near the interface. Since the extent of screening can be crucial to conserving the redox-active energy levels as shown in Figure 4.1, we examine how different percentages of surface coverage by monolayers can influence the energetic position of these states placed at $\delta = 1.0$ nm and 1.5 nm from the surface. Although, $|M|$ becomes stronger as δ gets smaller, the rate of ET can still be limited by the energy levels associated with the redox states[7,25] defined by $\pm\lambda + \Delta\phi(r_0 + \delta)$, where appropriate screening gives $\Delta\phi(r_0 + \delta) \approx 0$. We studied three systems with 20, 50 and 80% monolayer surface coverage which can be translated to approximately 3, 7.5 and 12 bridging monolayers grown per nm^2 area of an Au nanoparticle surface. The charging behaviour for these three cases is shown in Figure 4.4, where, $\delta = 1.5$ nm. No specific scan rate was employed here, rather the charging current was allowed to decay to a certain limit

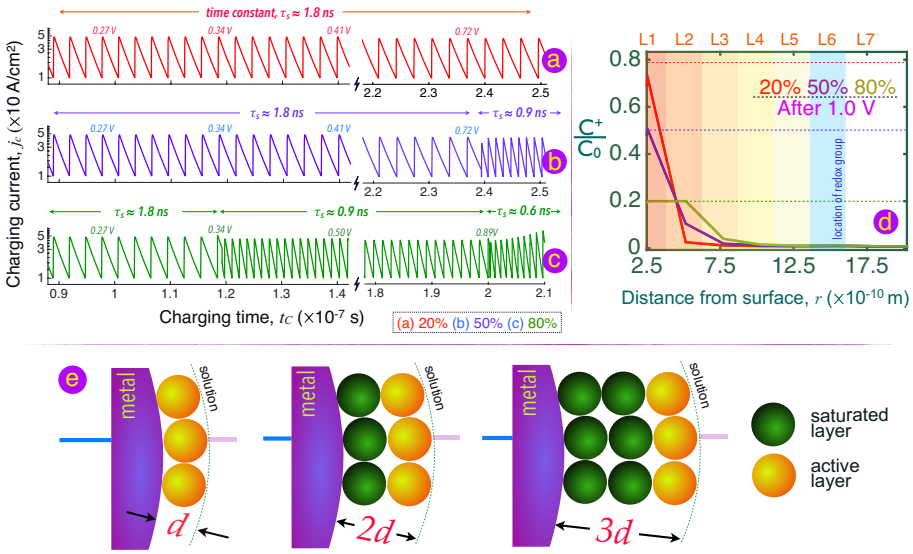

Figure 4.4: Continuous decay in the charging current (a-c) and the associated normalized concentration profiles (d) during the ultrafast scanning process for 20%, 50%, 80% surface coverage by 1.5 nm long monolayer with $|M| = 10^{-5}$ eV. The changes in coverage are assumed to be obtained with identical monolayers. Here C_0 is the maximum capacity of ion occupation on a bare surface. While the charging continues mostly in the closest layer (L1) with the same time constant for 20% (part a and d), it meets the maximum layer capacity early for 50% coverage at ∼0.73 V (d) when the decay process occurs with 1/2 of the original time constant (b). The same layer (L1) gets filled even earlier at ∼0.34 V (c,d) when 80% of the electrode surface is covered by monolayers, offering the remaining layers for ion occupation. Continuous charging here leads to filling up of the second layer (L2) at ∼0.89 V. The time constant τ_s drops at both transitions by 1/2 and 1/3 of the the original magnitude respectively (c). Part (e) illustrates layered ion accumulation followed by successive saturation which leads to reduced capacitance at the interface. This reduction leads to the drop in τ_s in part (b) and (c).

where the aforementioned screening condition was fairly satisfied. Nevertheless, one can easily deduce from the figure that a scan rate well above MV/s is accessible in each case.

For 20% surface coverage, the migrated ions fill around 70% of the total area in the first layer on the surface (L1 in Figure 4.4d) after ∼ 1 V of applied overpotential. The decay in j_c at each of the constituent η_{step} continues with a steady average τ_s of ∼ 1.8 ns as shown in Figure 4.4a. However, the capacity of the same layer with 50% coverage is filled

much earlier, causing further screening to continue by gathering the incoming ions mainly to the next layer (L2 in Figure 4.4d). Since the electric field at L2 is weaker in magnitude than at L1, the incoming supporting ions are required to screen a lesser extent of potential, thus the screening can be achieved much faster. Figure 4.4b shows that the corresponding j_c is decaying with a reduced τ_s of 0.9 ns. The space for charging is even more limited for 80% surface coverage, where both L1 and L2 become saturated (Figure 4.4d) by $\eta = 0.9$ V. At this point the effective time constant goes down by ∼63% of the original τ_s as shown in Figure 4.4c. Judging by these calculated values, the spherical RC-time constant τ_s can easily be related to the subsequent-layer-saturation via

$$\tau_s = \mathcal{R}_{si}\mathcal{C}_{edl} = \mathcal{R}_{si}\left(4\pi\epsilon_r\epsilon_0\frac{r_0(r_0+md)}{md}\right) \tag{4.17}$$

where $\mathcal{R}_{si}$ is the solution resistance to supporting ions transport and is taken as constant for a given solution, $\mathcal{C}_{edl}$ is the EDL capacitance, d is the packing layer separation in solution and m is the index of active layer for ion accumulation (Figure 4.4e). This can be viewed as a growth index parameter that relates with the time-dependent evolution of the thickness of electric double layer via $m \times d$ (as shown in Figure 4.4e). Lastly, the spherical area orthogonal to the direction of ion transport during drift and diffusion can be considered constant for layers close to interface. As the supporting ions fill the subsequent layers, the capacitance $\mathcal{C}_{edl}$ and hence the resulting time constant τ_s goes down closely by a factor of $1/m$. This is demonstrated in the charging characteristics of the interface with 80% packing density by redox monolayers as presented in Figure 4.4c. Such a compression in the time constant with increasing ion packing may allow us to design voltammetric schemes consisting of overpotential steps that varies dynamically in the charging time. This may

allow one to achieve faster scan rates, which may also preserve the energetics of redox-active groups at the desired level as illustrated in Figure 4.1 and 4.2.

4.3.3 Characterization of λ and $|M|$ with ultrafast scanning.

On the basis of this picture regarding the charging behavior in mind, we simulated the coupled charging and faradaic activities through LSV at several different scan rates, where a reorganization energy of $\lambda = 0.5$ eV was assumed. For all the current profiles, the screening condition corresponding to $j_c \leq 10$ A/cm^2 was enforced (discussed earlier with respect to Figure 4.4) throughout the scanning; and the total current j was sampled according to the method illustrated in Figure 4.2. The LSV scan rates were assessed based on a metric that may be termed the *ultimate scan rate*, R_{ult} [118] via the relation $R_{ult} = \eta_{scan} \times k_{max}$, where k_{max} is the maximum rate of electron transfer given by [7,126,127]

$$k_{max} = 4\pi^2 \frac{|M|^2}{h} D_S \tag{4.18}$$

and η_{scan} is the maximum applied overpotential. Importantly, applying scan rate R beyond this ultimate value R_{ult} results in gradual suppression of electron transfer with increasing scan rate, causing the voltammetric current to shift from demonstrating the usual peak feature towards the plateaued feature [118] that can be observed in typical ultrafast voltammetry. [13] We also adopt from our previous work the ratio $\alpha = R/R_{ult}$ between the applied scan rate R and the ultimate scan rate R_{ult}, which will be useful in the discussion of the simulated LSV results.

Let us begin by directly comparing LSV the results of a spherical nanoelectrode to that of a planar electrode. The j vs η plots from first set of spherical calculations with $|M| = 10^{-5}$ eV at different scan rates are presented in Figure 4.5a(i,ii). At the highest possible R defined by $\alpha \approx 5$, the total current at each η_{step} was recorded when the charging current decays

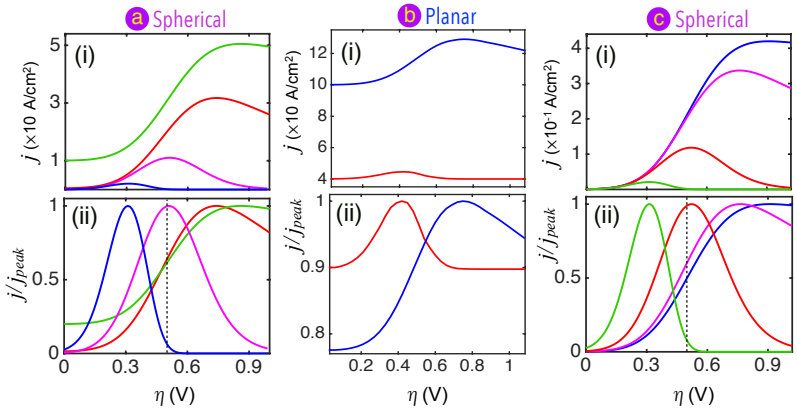

Figure 4.5: Current density (j) vs overpotential (η) plots for spherical (a,c) and planar (b) electrodes. Part a(i) shows j for assumed $|M|= 10^{-5}$ eV while the respective peak normalized profiles are shown in a(ii). The four scan rates here correspond to $\alpha \approx 5$ (green), 1 (red), 1/10 (purple), 1/100 (blue). The same is presented for $|M|= 10^{-6}$ eV in part c(i,ii) for $\alpha \approx 10$ (blue), 1 (purple), 1/10 (red), 1/100 (green). The approximate position of λ is shown by a broken line. Part (b) presents the current density profiles for a planar electrode with $|M|= 10^{-5}$ eV, where the enforced screening condition ($j_c \approx 100$ A/cm^2) gives the maximum scan rate corresponding to $\alpha \approx 1/2$ (blue). The red curve correspond to $\alpha \approx 1/10$. The charging current is large in both cases as explained in the text, making the planar electrode unsuitable for ultrafast applications.

to $\sim$ 10 A/cm^2 as seen in Figure 4.5a(i). The time to this decay is on average $\tau_s \approx 1.8$ ns. This upper bound of applied rate, defined by $\alpha \approx 5$ exceeds the maximum rate of ET (k_{max}) to produce a plateaued voltammetric response (green profile), the half maximum of which corresponds to the reorganization energy λ of the monolayer[118]. Accordingly, the predicted λ from the voltammogram is 0.5 eV which is equal to the assumed λ in the calculation.

As we reduce the scan rate from $\alpha \approx 5$ to $\alpha \approx 1$, where the rate of sweeping should match the k_{max}, voltammetric peaks begin to appear followed by asymptotic fall of the total current (red profile Figure 4.5a). The calculated charging time here is around $\sim 13\tau_s$ per η_{step}, corresponding to a decay in j_c to the order of $\sim$ 0.25 A/cm^2. Continuing the calculations with slower scan rates of $\alpha \approx 1/10$ and $\alpha \approx 1/100$ generates distinctly recognizable

peaks on account of longer time span provided for ET accompanied by a negligible charging contributions. These currents are shown in purple and blue, respectively, in Figure 4.5a(i). The two latter cases with $\alpha = 1/10$ and $1/100$ lead to an extremely small j_c. However, due to heavy computational expenses j_c was decayed to approximately 0.1 A/cm^2, below which the screening performed to minimize the electric field at and adjacent to the interface is negligible; hence the calculation thereafter proceeded only with the faradaic component. Although, this may lead to some partially unscreened potential at $r = r_0 + \delta$ caused by the accumulation of the faradaic charge in time. This introduces an upper bound on the screening shift in these slower rate calculations, where $\Delta\phi_s$ is expected to only go down if the screening were to continue beyond $j_c = 0.1$ A/cm^2 (see Figure 4.1). Because slow scan LSV curves are dominated by the consumption of reactants at low biases, we have found this does not have a discernible impact on the final LSV profiles. Figure 4.5a(ii) shows same current profiles normalized by the respective peak values in 4.5a(i). These are required for the extraction of $|M|$, as will be discussed shortly.

The simulation was repeated for a planar electrode with the same system parameters (as shown in Figure 4.5b). Here the drift and diffusion dynamics are linear, as opposed to the radial dynamics present in spherical systems. Having an order of magnitude or higher RC-constant than spherical electrodes, the maximum scan rate achievable here with planar electrodes lies below R_{ult} for the given $|M|$ as dictated by equation 4.18. Therefore, λ cannot be extracted here since the plateaued faradaic features are not obtainable with this electrode geometry. Figure 4.5b(i) and (ii) shows the j vs η profiles for two different scan rates differing by a factor of $\sim$1/5 and their peak normalized profiles, respectively. The highest obtainable scan rate corresponds to $\alpha \approx 1/2$ that leads to asymptotic fall of total current beyond the peak (blue curve). The slower rate represented by the red profile leads to nearly zero faradaic current after producing a well defined peak.

Finally, Figure 4.5c(i,ii) shows the results for spherical system with the same $\lambda = 0.5$ eV but with $|M| = 10^{-6}$ eV, typical of alkane monolayers[46]. For this coupling, the calculated ultimate scan rate was $R_{ult} \approx 9.5 \times 10^3$ V/s, which is two orders of magnitude lower than R_{ult} for systems with $|M| = 10^{-5}$ eV. Thus the applied scan rate R can be much larger than R_{ult} for this system, and the plateaued feature can easily be obtained. Moreover, due to this lower scan rate requirement, the charging current can easily be given enough time to decay to such a value where the faradaic features can be observed clearly. However, it is notable that the faradaic current would drop by two orders of magnitude as $|M|$ is reduced from 10^{-5} to 10^{-6} eV as determined by equation 4.11 and 4.12. Hence, applying high scan rates such as MV/s may generate voltammogram for the latter that is fully dominated by the charging current component. Figure 4.5c(ii) shows the position of half maximum of the plateaued profile which properly predicts λ to be 0.5 eV.

4.3.4 Role of faradaic charging.

Let us now examine, in further detail, how faradaic charging at redox sites influences LSV characteristics. Specifically, we shall explore the impact of the monolayer coverage and length on the redox group screening characteristics as illustrated in Figure 4.1. This is the final component needed to fully assess the accuracy to which λ may be characterized with ultrafast LSV measurements. While the potential distribution inside the liquid is primarily due to the applied η during active voltammetry, the growth of faradaic charge on the redox sites in time can cause the local potential at $(r_0 + \delta)$ to shift as well. This effect, although negligible when $\eta \ll \lambda$ due to the lack of charge transfer, can become an important component of interfacial screening when $\eta \geq \lambda$. This is demonstrated in Figure 4.6 for two different cases: when the monolayer length corresponds to $\delta = 1.5$ nm

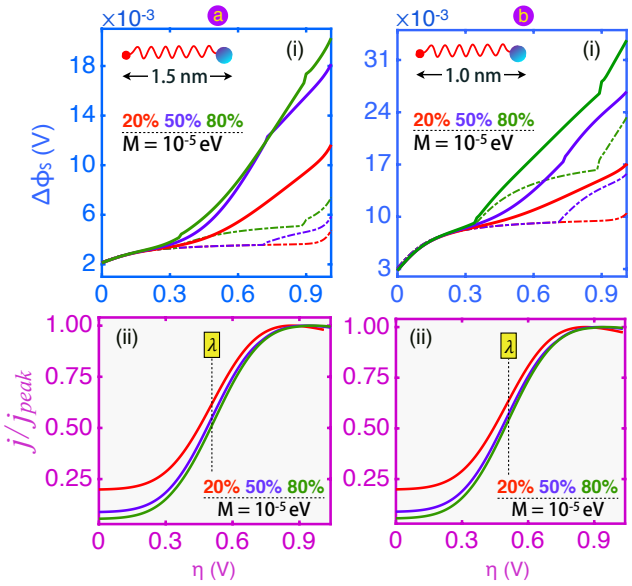

Figure 4.6: Shift of redox energy states during interface charging placed at $\delta = 1.5$ nm and $\delta =$ 1.0 nm away, a(i) and b(i) respectively, at an electronic coupling of $|M| = 10^{-5}$ eV. Coverages of 20, 50, 80% are considered. The shift is recorded after screening followed by decay of j_c to ~ 10 A/cm^2. Dot-dash curves show the electrostatic shift without considering faradaic charge present on the redox groups, whereas solid lines show the actual rise due to the combined effect of η and faradaic charge. The associated LSV currents ($j = j_c + j_{et}$) are shown in panels a(ii) and b(ii) along with the position of λ.

(Figure 4.6a(i)) and when the length is shortened to $\delta = 1.0$ nm (Figure 4.6b(i)) – each case evaluated for three different surface coverages.

If we ignore the faradaic charge for the moment, it seems that the effect of coverage on the electrostatic shift of redox levels at 1.5 nm away from the surface is small; since the shift $\Delta\phi_s$ (for spherical dynamics - as shown by the dot-dash profiles in Figure 4.6a(i)) is well below 10 mV as plotted for all three percentage occupations. However, including the effect of the faradaic charge leads to almost a threefold rise in $\Delta\phi_s$ for the chosen $|M|$ as shown by the solid curves in Figure 4.6a(i). Interestingly, this potential shift raises the half maximum for λ estimation to a barely perceptible higher η as shown in Figure 4.6a(ii). We note that

each abrupt change in the potential drop in Figure 4.6 corresponds to a change in the RC-time constant (as discussed earlier in the context of Figure 4.4). A similar comparison can be made for a shorter monolayer of length 1.0 nm as shown in Figure 4.6b. Here screening becomes more difficult within the targeted decay in charging current ($j_c \approx 10$ A/cm^2 as in Figure 4.4) than the above case with 1.5 nm long monolayers, due to stronger electric fields present closer to the interface. Hence, a general increase in $\Delta\phi_s$ for all occupations can be seen in Figure 4.6b(i) for the same level of current decay. The figure also shows that the evolution of faradaic charge shifts the redox levels at relatively high overpotentials by an additional 50-70% (shown in solid profiles in Figure 4.6b(i)) on top of the $\Delta\phi_s$ shift provided by interface screening (shown in dot-dashed profiles). Overall, the ultrafast LSV plots in Figure 4.6 show that λ may be measured with reasonable accuracy despite faradaic charge accumulation at redox centres.[118] This apparent contradiction can be explained by the low conversion of redox sites (<10%) during ultrafast LSV scans, with most faradaic charge transferred when $\eta > \lambda$. This, in turn, limits the excess rise in $\Delta\phi_s$ primarily to biases exceeding λ.

With the system parameters needed to effectively extract λ now understood, we can now focus on how the electronic coupling $|M|$ may be extracted for the two spherical systems discussed in Figure 4.5. As elaborated in our previous work[118], this can be obtained by first taking the derivative of the normalized current density profiles (j/j_{peak}) followed by taking their summation, which represents the percentage of *remaining reactants*[118] at the corresponding scan rate R. This refers to the states that are not provided sufficient time to participate in the faradaic processes by an ultrafast LSV scan. Ideally, in the absence of charging interference, scan rates corresponding to $\alpha \gg 1$ may result in close to ∼100% remaining reactants (as is ∼90% at $\alpha \approx 5$ in Figure 4.5a). On the other extreme, for $\alpha \ll 1$, the summation can practically be ∼0%. Between these two extremes, one can identify R_{ult}

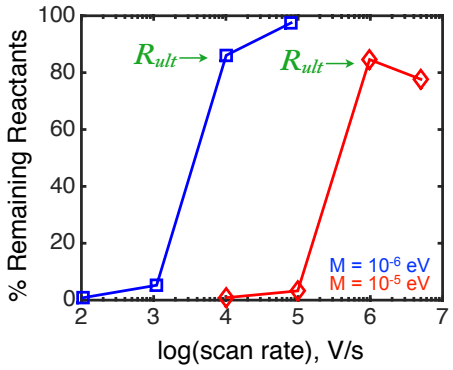

Figure 4.7: Percentage of remaining reactants in a cathodic LSV cycle at different scan rates. This is calculated by taking the sum of derivatives obtained for each of the peak normalized profiles for assumed $|M|= 10^{-5}$ and 10^{-6} eV spherical systems in Figure 4.5. The sudden upsurge at this derivative summation gives the approximate value of the ultimate scan rate, R_{ult} which can be used to determine the electronic coupling $|M|$ from experiments.

by the scan rate at which a sudden jump is observed in the derivative summation from near zero to a non-trivial percentage of remaining reactants. This shift appears due to the asymptotic fall of the faradaic current at $\alpha \approx 1$. This R_{ult} upon conversion to k_{max} can be used to calculate $|M|$ via equation 4.18 as discussed in Ref. 118.

The calculated percentages from the derivative summations extracted from the plots in Figure 4.5a(ii) and c(ii) are shown in Figure 4.7. Based on the results in Figure 4.5, the extracted R_{ult} for the two profiles with assumed electronic couplings of 10^{-5} (red) and 10^{-6} (blue) eV were $\sim 9.75 \times 10^5$ and $\sim 1 \times 10^4$ V/s, respectively. To these results, equation 4.18 can be applied to extract $|M|$ values of $\sim 8.9 \times 10^{-6}$ and $\sim 9.3 \times 10^{-7}$ eV, respectively, which is sufficiently close to the actual values. Interference due to high charging current contributions in this type of characterization is apparent in the red profile of Figure 4.7 where the summation saturates below 100%. Intuitively, for the highest applied rate ($\alpha \approx 5$) in the $|M|= 10^{-5}$ eV scenario, the derivative sum should be close to 100%. However, due to the high charging current present, particularly at low biases

in the normalized current plot provided in Figure 4.5a(ii), it predicts only ∼77%. Hence, the derivative method fails here to produce the correct percentage of remaining reactants. While the problem reduces with lower $|M|$ in spherical electrodes, the charging current becomes even more problematic in planar electrode systems as shown in Figure 4.5b(ii) or in systems with very strong electronic coupling ($|M|$).

These calculations suggest that high charging currents are unavoidable in ultrafast voltammetric experiments, which according to the results presented in Figure 4.5 and 4.7 may obstruct the characterization of λ and $|M|$ through ultrafast methods[118]. However, the non-faradaic charging component may be isolated through controlled LSV measurements of an electrochemically inactive monolayer without pendant redox sites. The absence of faradaic activity in such a system would provide a current composed only of the charging contribution (j_c). This charging component can be used as a reference for the screening process that can be subtracted out from the total current ($j = j_c + j_{et}$) to obtain the pure ET current (faradaic). Upon extraction, this faradaic output ($j_{et} = j - j_c$) can be analyzed to calculate λ and $|M|$. This subtraction method has indeed been employed previously by Amatore *et. al.*[103] to obtain the faradaic response.

In general, depending upon the system configuration, the factors and issues discussed here can play important role in determining the ET efficiency in various ultrafast applications. While we have only considered Na^+ and Cl^- supporting ions, that are among the species with high diffusivity ($> 10^{-5}$ cm^2/s) in aqueous solution, in practice a system may contain ions that have orders of magnitude lower diffusivity. In such cases, screening may take much longer, yielding a maximum possible rate of applied overpotential that is significantly lower than MV/s. If a scan rate beyond the limit set by screening is employed, then the electrostatic shift of redox states can seriously hamper the efficiency of ET over the expected range of overpotential. However, the general limitation in the diffusivity of

supporting ions sets the upper bound of an applied scan rate at MV/s. Scan rates in this upper bound would allow for the characterization of redox-active electrochemical systems via the proposed model with an electronic coupling $|M|$ of up to $\sim 10^{-5}$ eV.

4.4 Conclusion

In conclusion, an electron transfer model derived previously[7,118] in the context of redox-active molecular systems was employed to study time dependent simulations of redox reactions across a monolayer passivated metallic substrate. To theoretically assess the capabilities of ultrafast voltammetry, the model incorporated interfacial screening by the supporting ions in an aqueous solution through drift and diffusion. A comparative study between the interface charging current associated to the screening process and the faradaic current was presented, which may allow well regulated decay of the charging current with proper screening to ensure the electrostatic conservation of redox energy levels during ultrafast voltammetry. Scan rates corresponding to the timescale of these events can be used to characterize the redox reorganization energy (λ) and electronic coupling ($|M|$). Effects of insufficient screening or possible interference from high charging currents in voltammetry can be overcome by tuning the electronic coupling $|M|$ and utilizing a nanoelectrode. In addition, a reduction in the time constant of the decay current with increased ion packing might lead to successive reductions in the RC time constant. This may lead to the possibility of obtaining faster screening through the rapid filling of ionic packing layers in systems with high surface coverage comprised of long chain monolayers. However, high surface coverage may reduce the efficiency of redox processes in short chain monolayers by restricting the space required for screening the electrode potential. In general, the results of this study are expected to aid in the characterization of redox reactions at solid-liquid interfaces.

The study presented in this chapter provides a theoretical basis to the utilization of ultrafast scan rates such as ∼MV/s in characterization of redox-active monolayers via voltammetry. The formulation highlights some key features that can minimize the distortion of total current arising from ionic transport and the associated charging current in solution. With this basis, an electrochemical method is presented in the following chapter to characterize the energetic makeup of an electro-active levels of a model solvated redox-active system. In this model, both slow and ultrafast scan rate regimes have been utilized to analyze and extract the individual energetic components, knowing that it is feasible to obtain characterizable faradaic responses at ultrafast voltammetry.

CHAPTER 5
A General Theoretical Framework for Characterizing Solvated Electronic Structure via Voltammetry: Applied to Carbon Nanotubes

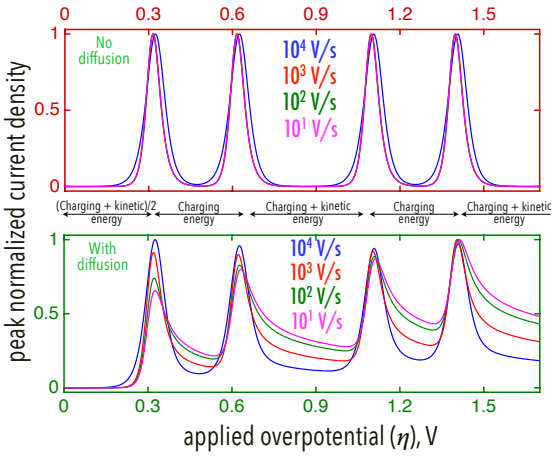

The discussion presented thus far provides a detailed analysis on the extraction of an electroactive energy level from a kinetically suppressed current response. Such a level in practice would consist of multiple energetic components based on contributions from redox-active and supporting species in electrolyte. In this chapter, the current discussion is extended into analysis of multiple electron transfer voltammetry applicable to redox-active molecules and nanoparticles, which can give a direct in-situ measurement of the individual components of the total energetics. A extensive formulation in this regard is proposed which interestingly can lead to the electrochemistry based energy dispersion relation of a nanoparticle system.

We propose a general theoretical framework for multiple electron transfer to solvated nano-particles and their characterization via linear sweep voltammetry. A direct connection is made between the peak potentials observed in voltammograms and the electronic structure of solvated particles. Two major contributions to the voltammogram extracted electronic structure properties are established to be: the quantization of electron kinetic levels (ε^T) and the single electron charging cost (U), both of which display a significant variation with nanoparticle dimensionality. The dimensional dependences of these energetics is reflected in the spacings between voltammetric current peaks. The simultaneous role played by U (typically associated with Coulomb blockade) and ε^T at all dimensions advances our understanding of their relative contributions in the so-called molecular redox charging regime and the nanoparticle charging regime. These general physical properties are investigated in a model solvated "particle-in-a-box" system, consisting of finite length armchair semiconducting carbon nanotubes. While implemented within a model system, the physics underlying these energetics are expected to be general to all solvated species. However, the scan rate dependence of the peak potentials in voltammetry under a considerable reorganization energy (λ) complicates direct correlations between redox-active energetics and peak spacing features. We argue that this scan rate dependence can be resolved by ultrafast voltammetry. Through combined ultrafast and conventional voltammetry, the solvated electronic structure contributions of reactants (including ε^T, U and λ) should be accessible (as shown in the model system). The proposed solvated electronic structure physics and voltammetric extraction technique is general in scope and should be executable on any solvated nanomaterial system participating in heterogenous outer-sphere reactions.

5.1 Introduction

Quantized single electron charging is one of the most intriguing discoveries[128] in the field of solution phase nanomaterials, and has been observed over a wide range of dimensions from protected metal clusters[128–131] to caged structures such as fullerene[132–134], and in graphene[135]. The nature of quantization, detectable via the current vs. voltage response in such species demonstrates a significant size dependence[128,129,136], where the identical separation potential observed between subsequent current peaks for large clusters gradually shifts to exhibit inconsistent and/or broader peak spacings for small nanoparticle dimensions[130]. The first observation, confirmed by experiments carried out in both solution phase electrochemical[130,132,137] and solid state electronic systems,[138] was attributed to the Coulomb staircase charging[128,139] – which can be defined by the energy cost associated to the addition/removal of a single electron to an electroactive species. This mechanism however, is known to change into molecular redox charging[128] for much smaller geometries that gives rise to variability in successive peak separations as pointed above in the latter case. These trends demonstrate the role played by the nanoparticle energetics on the nature of current output in an electrochemical measurement. The responsible energetics primarily include the single electron charging energy U and electron quantization contributions to molecular energy level spacing ($\delta\varepsilon^T$). Despite the suggested nature of the shift in the mechanisms from redox charging to Coulomb blockade,[128,129] both of these contributions are dimension dependent functions - such that with the downscaling of the investigated nanoparticle size the density of electronic states goes down (dictated by $\delta\varepsilon^T$), notably adjacent to the Fermi level (ε_F), while the U goes up. This dependency reveals a largely unexplored aspect within the transition from the molecular redox to the Coulomb repulsion charging limits, with respect to the dimensional changes of a nanoparticle, which can lead to interesting approaches for the electrochemical characterization of $\delta\varepsilon^T$ and U.

The objective of this chapter is to propose a general theoretical framework for the interpretation of solvated electronic structure as explored through voltammetry – in outer-sphere redox process at all reactant dimensions. In multiple charge transfer voltammetry, each transfer follows as the applied overpotential (η) overcomes both $\delta\varepsilon^T$ and U, which add up to construct a typical single-particle level. These two contributions however are not directly transferable to the energy/potential at which an electron transfer (ET) takes place in a solvated environment, due to nuclear reconfiguration (λ) of both redox reactant and the surrounding solvent species in response to an ET. This interaction places an additional *blockade* to charge transfer via reorganization (λ). Furthermore, the broadening of single-particle levels under the influence of reactant and solvent reorganization introduces a scan rate dependence in voltammogram current-peak positions, that further complicates the extraction of electroactive energy level information. Our theoretical framework is intended to quantify all these contributions and enable the direct interpretation of solvated electronic structure properties via voltammetry. The prospect of quantifying these energetics via voltammetry offers a useful and complementary approach to various spectroscopic techniques[140–146] for solvated molecular[147]/nanoparticle characterization. A particle with its electronic structure determined via spectroscopy can behave quite differently[148,149] in the presence of a solvent, which directly impacts upon U and introduces λ to the total energetics. Therefore, the quantities obtained from current-overpotential characteristics can provide direct system-specific information on charge transfer energetics in an electrochemical setup.

When selecting a model system to explore these features and our framework, our primary consideration is that both $\delta\varepsilon^T$ and U should be near equally resolvable via voltammetry. A nano-particle system which possess 2D or 3D symmetry, will exhibit quantization degeneracy in the electron kinetic energies (ε^T) – e.g. the six-fold lowest unoccupied

molecular orbital (LUMO) degeneracy in fullerenes.[132–134] Fully resolving successive $\delta\varepsilon^T$ contributions by overcoming multiple degenerate electronic states with an overpotential is often not possible due to breakdown of the electrolyte.[132–134] *Thus ideally, to fully explore the proposed framework one would wish to utilize a model 1D "particle-in-a-box" type system with limited quantization degeneracy (with levels accessible at stable electrolyte overpotentials).* To this end we have chosen to explore these energetic features in a model finite-length single walled armchair carbon nanotube (CNT) system that acts as our solvated "particle-in-a-box", whose quantized energy levels typically offer minimally degenerate highest occupied molecular orbital (HOMO) and LUMO energy levels. This model system allows us to clearly elucidate the contribution of both $\delta\varepsilon^T$ and U in a simulated voltammogram across all length scales, however the physical interpretation is expected to be general.

Within our model redox-active system, we simulated multiple heterogenous reductions through linear sweep voltammetry (LSV). The peak potentials from the current profiles were then utilized to extract experimentally obtainable energetics. The energies, derived as a function of particle geometry were then used to construct: (1) an electrochemical energy level structure near ε_F of the analyzed species, and (2) the associated energy dispersion relation. From this we show that voltammetry can produce important information regarding the solvated electronic structure contributions of $\delta\varepsilon^T$, U and λ. The study thoroughly emphasizes that the basis of these connections are rooted in the fact that the contributions from the two most important energies, kinetic electron quantization $\delta\varepsilon^T$ and Coulomb interactions U, are quantitatively significant at all particle dimensions, and its validity is shown for nano length scales. Given the universality of these energetic contributions and

their dependency on particle geometry, these findings are expected to be generally applicable in nano and molecular systems.

5.2 Method

5.2.1 General theoretical framework.

Voltammetry measures single-particle energies for the insertion (reduction) and removal (oxidation) of electrons in solvated systems with respect to a reference electrochemical potential at overpotential $\eta = 0$. Single-particle energies are defined by the difference between total energies $\mathtt{E}$ for a given occupation change of electrons[61], say from $(N-1)$ to N

$$\varepsilon_N = \mathtt{E}(N) - \mathtt{E}(N-1) \tag{5.1}$$

There are several contributions to the total energy, each of which change during redox events. Under the Born-Oppenheimer approximation, $\mathtt{E}$ has the form[150]

$$\mathtt{E}(N) = T_e(N) + U_{ee}(N) + U_{e\mathcal{N}}(N) + U_{\mathcal{N}\mathcal{N}}(N) \tag{5.2}$$

Where, $T_e(N)$ is the kinetic energy of electrons as determined by Schrodinger's equation, $U_{ee}(N)$ is the electron-electron interaction energy, $U_{e\mathcal{N}}(N)$ is the electron-nuclear interaction energy, and $U_{\mathcal{N}\mathcal{N}}(N)$ is the nuclear-nuclear interaction energy each for an N electron and $\mathcal{N}$ atom system. The difference in total energies, which are the electronic ground state single-particle energies accessed by voltammetry, thus has several terms contributing -

$$\begin{aligned}\varepsilon_N = [T_e(N) - T_e(N-1)] + [U_{ee}(N) - U_{ee}(N-1)] + \\ [U_{e\mathcal{N}}(N) - U_{e\mathcal{N}}(N-1)] + [U_{\mathcal{N}\mathcal{N}}(N) - U_{\mathcal{N}\mathcal{N}}(N-1)]\end{aligned} \tag{5.3}$$

each of which depend on the system size.

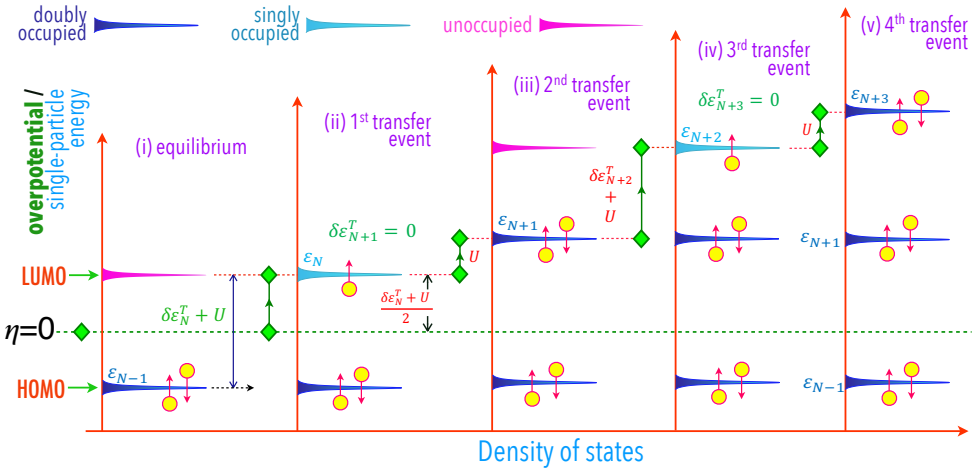

Figure 5.1: Schematic of single particle energy spectrum in the negligible λ limit. Part (i) shows these spin-degenerate levels under equilibrium at $\eta = 0$ in a solvated system; ε_F is placed halfway between the HOMO and LUMO levels, that are assumed to be in equilibrium with the electrode electrochemical potential. Part (ii-v) illustrates the effective single-particle energies for four consecutive single electron occupations at ε_N, ε_{N+1}, ε_{N+2}, ε_{N+3} under $\eta > 0$ in the presence of a charging energy U. The change in applied η follows the green diamonds on the left of each panel. The effective energy demand for each transfer event in (ii-v) is marked in red letters. This picture changes when $\lambda \gg k_B\mathcal{T}$ (see Figure 5.2).

Though these terms are coupled through Schrodinger's equation and the many-body wavefunction describing the system, to first order we can attempt to separate out these terms in order to estimate their individual contributions via voltammetry. To simplify the analysis, we begin by assuming that the change in nuclear coordinates is negligible ($\lambda \approx k_B\mathcal{T}$) upon addition/removal of an electron, such that we can make the approximation

$$\varepsilon_N \;\approx\; [T_e(N) - T_e(N-1)] + [U_{ee}(N) - U_{ee}(N-1)] \;\approx\; \varepsilon^T + UN \tag{5.4}$$

where ε^T is the electron kinetic energy contribution (due to quantization). Here, k_B is Boltzmann's constant and $\mathcal{T}$ is the temperature. We have assumed the mean-field electron-electron interaction $U_{ee}(N) = UN(N-1)/2$, with U representing the Coulomb interaction

between two electrons[61]. In this negligible nuclear relaxation limit, the separation between two single-particle energy levels becomes

$$\delta\varepsilon_N = \varepsilon_N - \varepsilon_{N-1} \approx \varepsilon_N^T - \varepsilon_{N-1}^T + U = \delta\varepsilon_N^T + U \tag{5.5}$$

as shown in Figure 5.1. Here, U would be the Coulomb blockade voltammetric peak separation when $\delta\varepsilon_N^T \to 0$.[61,130,151] Moreover, this separation $\delta\varepsilon_N$ depends upon the degree of quantization and the degeneracy of the accessed single-particle energy. To simplify our analysis we'll deal with levels having only spin degeneracy, but the approach is generalizable to reactants with degenerate orbitals. Figure 5.1 illustrates such a system of single-particle levels during the transfer of four electrons under an applied overpotential; this picture assumes $\lambda \approx k_B\mathcal{T}$, such that ET during both reduction and oxidation events take place from the same single-particle level. However, a considerable solvent reorganization ($\lambda \gg k_B\mathcal{T}$) gives rise to splitting of each single-particle level via a *Stokes shift*[152–154] into acceptor/absorption (D^{acc}) and donor/emission (D^{don}) states, which are shifted by $+\lambda$ and $-\lambda$, respectively from the original single particle energy (such as $\varepsilon_{N-1}, \varepsilon_N, \varepsilon_{N+1}, ...$) as shown in Figure 5.2. The Gaussian distribution of these acceptor and donor states arise from molecular vibrations due to thermal energy.[152–154] During reduction, electrons are transferred from a metal electrode to an unoccupied acceptor state whose density of states (DOS) according to Hopfield[152–154] and Gerischer[49–51] can be written as

$$D_N^{acc}(\varepsilon) = \frac{1}{\sqrt{4\pi\lambda k_B\mathcal{T}}} exp\left(\frac{-(\varepsilon - \varepsilon_N - \lambda)^2}{4\lambda k_B\mathcal{T}}\right), \tag{5.6}$$

Here, D_N^{acc} represent the DOS of the N^{th} acceptor state from the single-particle level ε_N as shown in Figure 5.2 and ε is the single-particle energy relative to a reference potential.[152–154] This transfer event activates a reorganization of the redox species single-particle energy by 2λ into a donor state (expressed as a future state prior to electron transfer and

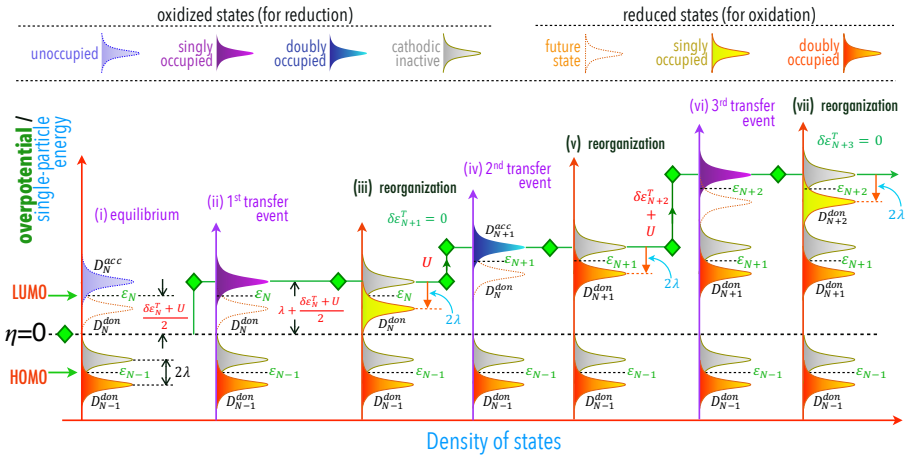

Figure 5.2: The single particle energy levels structure consecutively accessed by three electrons under applied cathodic overpotential ($\eta > 0$), when $\lambda \gg k_B\mathcal{T}$. The effective η is shown by the green diamond. The states are broadened by λ via equations 5.6 and 5.7. In comparison to the negligible λ limit (Figure 5.1), electron transfer here is followed by reorganization of the solvent and the redox-active species. This eventually shifts down the single-particle states by 2λ that are effective during anodic processes. Grey states express the limitation of Faradaic processes at the single-particle energy to oxidation only, after insertion of an electron into an acceptor state and subsequent nuclear reorganization into a donor state.

subsequent reorganization in Figure 5.2). However, since there is a finite probability that this electron may tunnel back prior to reorganization,[9,46,155] which is typically quite small in the outer-sphere tunneling reactions considered here. Consequently, the donor state appears 2λ below the acceptor state[7,152–154,156] (Figure 5.2) and can be expressed as

$$D_N^{don}(\varepsilon) = \frac{1}{\sqrt{4\pi\lambda k_B\mathcal{T}}} exp\left(\frac{-(\varepsilon - \varepsilon_N + \lambda)^2}{4\lambda k_B\mathcal{T}}\right), \tag{5.7}$$

where D_N^{don} is the N^{th} donor state. Implementing the role of λ in a multiple ET scenario evolves the picture presented in Figure 5.1 into a more detailed scheme shown in Figure 5.2. While the acceptor and donor states in Figure 5.1 overlap, the three consecutive reduction events illustrated in Figure 5.2, are each coupled with reorganization of the

acceptor state (D^{acc}) into a donor state (D^{don}) marking the difference between energies accessed during reduction and oxidation events via voltammetry. We assume that λ is the same for each electron transfer event, but the general physics in Figure 5.2 remains even if λ changes between transfer events. An extended analysis of this scheme follows in Section 5.3, where we discuss cathodic current obtained by accessing these energies in a voltammetric simulation. We note that in Figure 5.2, the Fermi level at equilibrium $\eta = 0$ was taken to lie exactly between the HOMO (ε_{N-1}) and the LUMO (ε_N) level. This type of initial equilibration has been observed[133] in a redox scan of C_{60} and C_{70}. However, one may also encounter redox couples such as Fe^{3+}/Fe^{2+} complexes[1] as well, where the Fermi level at $\eta = 0$ rests between an acceptor (Fe^{3+})/donor (Fe^{2+}) pair. In a multiple ET picture, this second equilibration type changes the energy required for the first redox event to λ, which is also deducible from Figure 5.2. However, in this work we consider multiple electron transfer for only the first type of charging and leave the second for future work.

Because of the universality of these energy components ($\delta\varepsilon^T$, U as well as λ) in the makeup of successive single-particle energies, we wish to explore how both $\delta\varepsilon^T$ and U can be estimated from voltammetry. Though earlier authors have explored the extraction of U using this technique[128,129,137,157], the additional extraction of $\delta\varepsilon^T$ remains largely unexplored in the context of voltammetry. To this end we have chosen finite length armchair CNTs, which offer a model system whereby $\delta\varepsilon^T$ can be related to quantization of the electron wavevector in the infinite tube and degeneracy is simplified due to the one-dimensional nature of the system, similar to that of a "particle-in-a-box".

5.2.2 Relationship with shell filling experiments

Before proceeding with our voltammetry study, it is important to note that $\delta\varepsilon^T$ and U contributions have been observed in the context of steady-state charge transport across

nanoparticles. Examples include experiments performed via tunneling spectroscopy [158,159], where a molecule on a substrate is probed via scanning tunneling microscopy (STM). In these steady-state tunneling experiments, which reside in the *shell filling* limit, charge transfer from the STM tip to the molecule is much faster than that from the molecule to the substrate. Hence, the addition of electrons results in conductance peaks whose positions not only depend on the placements of the single-particle kinetic energy levels (ε^T), but also on the Coulomb repulsion energies (U). In this limit, the energetics that determine the gaps between tunneling conductance peaks are given by equation 5.4. However, while the energetics are similar to that in voltammetry, the actual charge transfer processes in shell filling studies are much faster than the electrochemical processes described here. Moreover, shell filling charge transport experiments are typically steady-state measurements rather than transients (which is the case for voltammetry). A deeper connection between the solvated Coulomb blockade phenomena considered here and steady-state conventional Coulomb blockade phenomena [159] merits an independent study for future work.

5.2.3 Model system energetics

In order to simulate electron transfer, we begin by outlining the theoretical approach utilized to calculated quantized electronic structure (ε^T) of our model semiconducting armchair CNT system. As discussed in the introduction, we have chosen this model system because it behaves as a 1D "particle-in-a-box". Systems with greater symmetry typically possess multiple orbital degeneracy, that often show only one $\delta\varepsilon^T$ contribution before breakdown of the supporting electrolyte is reached. [132–134] In this work, we wish to emphasize general physics through both multiple $\delta\varepsilon^T$ and U contributions. Calculations were performed using the nearest neighbour tight-binding (TB) approach, [61,160] where a CNT unit cell was defined by a single column of carbon atoms arranged in the armchair configuration.

For full details see the appendix. This unit nanoring cell was repeated in space to generate a finite nanotube and build the corresponding Hamiltonian for calculating the quantized electronic structure. As the goal of this section is to elucidate qualitative general physics, rather than exactly match or predict experimental values, we have left density functional theory (DFT) based first-principles calculations to future work. However, the number of atoms that are under consideration, including both the solvent and reactant, would render DFT calculations extremely computationally challenging.[161] Moreover, DFT based methods presently demonstrate significant unresolved delocalization errors for solvated charged species, due to underlying exchange-correlation errors, which precludes their immediate quantitive comparison to experiments even for small solvated systems.[162,163]

For all CNTs, we assume that the equilibrium energy levels are filled up to ε_F, which in general is located at the middle of the highest occupied (HOMO) and the lowest unoccupied (LUMO) molecular level[61] (see Figure 5.1). Under an applied overpotential, any interfacial ET event would result in either populating the empty states starting from the LUMO level (reduction) above the ε_F or loosing electrons beginning with those from the HOMO levels (oxidation) at or below the ε_F. For a single ET process to be successful, the applied overpotential as discussed above, must also overcome the Coulomb interaction barrier U. This has been well demonstrated for C_{60} and C_{70}.[132] For a spherical nanoparticle, the Coulombic interaction during a single or multiple exchange events can be obtained simply via $U_s = q/4\pi\epsilon_s\epsilon_0 r_s$,[61] where q is the unit charge, ϵ_s and ϵ_0 are the static dielectric constant of the solvent media and the permittivity of vacuum, respectively, r_s is the radius of spherical particle. However, for a nanotube this contribution to the single-particle electron addition/removal spectrum, as discussed in the context of equations 5.4 and 5.5 may be

defined to first order as

$$U = \frac{q}{4\pi\epsilon_s\epsilon_0 L}\, ln\left(\frac{x+\sqrt{x^2+R^2}}{x-L+\sqrt{(x-L)^2+R^2}}\right), \tag{5.8}$$

which has to be supplied externally via η. Here, x denotes the position of an electron along a CNT of length L and radius R. While U can make a significant contribution across different nano-geometries, it becomes negligible for bulk CNT dimensions as L and/or R approaches ∞. At this point, the magnitude of U falls below the ambient energy $k_B\mathcal{T}$ that renders the energy shift insignificant. This dimensional trend holds for all reactants. Constraining the value of x along the length L of the nanotube between $x = 0$ and $x = L$ leads to a parabolic distribution of U that peaks at $x = L/2$. This suggests that the charging cost is the maximum when an incoming electron is added at the center of the nanotube. In our calculations, this distribution was averaged to obtain the applied U. With this understanding of ε^T and U, we now focus on simulating ET events across an interface.

5.2.4 Current density

The interface ET processes is assumed to be outer-sphere in nature as illustrated in Figure 5.3, with rates are governed by electron tunneling. Two different scenarios were investigated within this regime. Firstly, System 1, where the model redox group (taken to be CNTs in this work) are uniformly bound to the metal by hydrocarbon chains that facilitate the tunneling process. This configuration is illustrated in Figure 5.3a. We assume a uniform coverage of 1 chain per unit nm^2 area on the electrode surface. The tunneling is captured by the electronic coupling $|M|$ between the metal and the model reactant[46]. However, the stability of such a structure may be jeopardized as model reactant dimensions grow. Hence, the alternate approach presented in Figure 5.3c may be considered (System

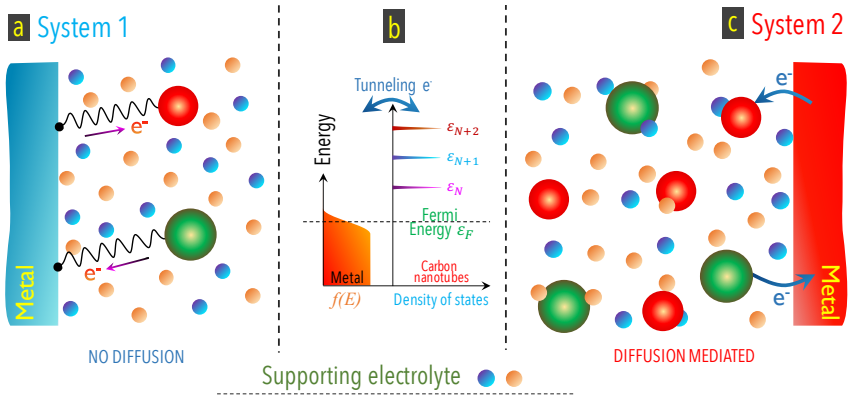

Figure 5.3: Heterogenous interface between a metal electrode and redox-active states (red and green spheres), represented in this work by finite length armchair CNTs. Electrons may tunnel via a monolayer bridge (a) or can tunnel via the dielectric solvent media directly to redox states (c). Supporting ions maintain charge neutrality in the solution at equilibrium, and screen the interface potential under nonequilibrium ($\eta \neq 0$)[27]. A scheme of the energetic configuration of these systems under equilibrium is shown in part (b) (see also Figure 5.1).

2), where an ensemble of unbound model reactants are distributed within an entire electrolyte solution. The heterogenous ET processes in this configuration can be simulated by capturing the tunneling of electrons to/from reactant states over a range of distances from the electrode surface. In this case, the interfacial coupling is dictated by the characteristics of the solution. Unbound reactants can roam freely in the solution, which allows them to achieve good proximity to the electrode surface in order to transfer an electron. Unlike the monolayer bound case (System 1), the tunnelling here is not limited to a fixed distance, but instead drops exponentially as a function of the separation distance between a floating reactant and the surface. For both systems we assumed that $|M|$ lies in between 10^{-5} to 10^{-6} eV, which are common[46] to tunneling dominated electrochemical processes. It is important to note that predicted mixture of Coulomb blockade and kinetic features can only be observed in the weak coupling (tunneling) limit.[61] In the strong coupling limit associated with strong chemical bonding ($|M| \rightarrow$ 1 eV), Coulomb blockade cannot occur

due to strong hybridization between the wavefunction of the reactant and contact.[61,151] In both systems, we further assume that the solution contains the appropriate amount of supporting electrolyte to screen any ohmic drop at the interface[103,132,164]. Although, the two schemes are similar, nonequilibrium interactions in System 2 are highly likely to promote the transport of reactants within the solution via drift and diffusion, which can alter the calculated current under an applied bias (see Figure 5.6). The density of this current, as obtained in voltammetry, represents the extent of interfacial processes via electron transfer, and can be calculated using the expression

$$j(\eta,t) = 4\pi^2 q \frac{|M|^2}{h} D_S \sum_{N=1}^{N_s} \left(C_N^{acc}(t) \int f(\varepsilon+\eta)\ D_N^{acc}(\varepsilon)\ d\varepsilon - C_N^{don}(t) \int (1-f(\varepsilon+\eta))\ D_N^{don}(\varepsilon)\ d\varepsilon \right) \tag{5.9}$$

which can be derived from well known electrochemical rate expressions[7,52,53] for reduction and oxidation processes. Here $|M|$ is the electronic coupling, h is Planck's constant, and N_s is the number of reactant single-particle states. The density of states in the metal is given by D_S, with the Fermi occupation distribution is given by $f(\varepsilon) = [1 + exp((\varepsilon - \mu_{eq})/k_B\mathcal{T})]^{-1}$, and the equilibrium electrochemical potential μ_{eq}. C_N^{acc} is the concentration of the acceptor states awaiting the arrival of the N^{th} electron into the state D_N^{acc}, which is followed by giving rise to the donor state D_N^{don} with a concentration C_N^{don}.

For the monolayer bound case in the System 1, the evolution of these concentrations in time along the progress of the redox processes can be determined as discussed in Ref. 27. However, in System 2 the redox species (CNTs in this work) move due to non-zero concentration gradients of different charged species under nonequilibrium that promote their diffusion to and away from the metal surface. This causes a continuous spatial rearrangement of the different reactant charge states, especially near the surface, that must be captured and incorporated within $j(\eta,t)$ in order to maintain the correct concentrations

of the electroactive components at the interface. We neglect the drift of reactants in our study on the basis of the assumption that the electrode potential would be fully screened by the supporting ions in the electrolyte.[27] This can be justified by assuming very fast ($\sim 10^{-5}$ cm^2/s) supporting ion diffusivity. For example, in a cathodic cycle, the transition of the charge state N to $(N+1)$ of an active redox species would trigger a species flux with N electrons toward the surface and a flux with $(N+1)$ electrons away from the surface. We can express these as

$$J_N^{acc}(r) = qD\nabla C_N^{acc}(r) \qquad and \qquad J_{N+1}^{acc}(r) = qD\nabla C_{N+1}^{acc}(r) \tag{5.10}$$

along with the respective continuity equations

$$q\frac{\partial C_N^{acc}(r)}{dt} = \nabla \cdot J_N^{acc}(r) \qquad and \qquad q\frac{\partial C_{N+1}^{acc}(r)}{dt} = \nabla \cdot J_{N+1}^{acc}(r) \tag{5.11}$$

throughout the entire span of the reduction process. Here r is the distance from the surface, δt is the length of the time step in which the electrochemical processes were captured, D is the diffusivity of the reactant which was taken as a constant in the calculations. The renewed concentrations at any distance from the surface can then be determined via the expressions

$$C_N^{acc}(r, t+\delta t) = C_N^{acc}(r,t) + \delta t \times \partial C_N^{acc}(r)/\partial t \tag{5.12}$$

$$C_{N+1}^{acc}(r, t+\delta t) = C_{N+1}^{acc}(r,t) + \delta t \times \partial C_{N+1}^{acc}(r)/\partial t. \tag{5.13}$$

Continuous evolution of all the electroactive concentrations coupled with equations 5.6, 5.7 and 5.9 gives rise to the observed cathodic current density in the simulated voltammetry. Expressions identical to equations 5.10 through 5.13 can be written for the anodic cycle as well to obtain the oxidation current density. Reactant diffusion to and away from an interface can become gradually more limited as the tube size becomes longer. In that case,

electrolyte stirring can be a probable solution to maintain sufficient reactant concentration at an electrode. This would add a migration term[1] for the CNTs in equation 5.10. Nevertheless, we proceed with equation 5.10 for our calculations. With this formulation, first we investigate the scheme presented in Figure 5.1, where the nuclear reorganization associated with the redox events is negligible. We show in the discussion that follows, that this preliminary assumption allows us to easily correlate between the single-particle levels and the voltammetric peaks. Later, we consider the role of $\lambda \gg k_B\mathcal{T}$ on the voltammetric response, as suggested in Figure 5.2.

5.3 Results and Discussion

5.3.1 Kinetic energy levels of the model system

A detailed account of the calculated energy-level structure of the armchair CNTs, that we have chosen as as our model "particle-in-a-box" system, is provided in the supporting information section. Our tight-binding calculations suggest that confining a nanotube to a finite dimension transforms the typical metallic character of infinitely long armchair nanotubes into mixed metallic and semiconducting properties,[165] due to quantization sampling of the infinite length Brillouin zone in the manner of a "particle-in-a-box". Hence, these tubes are metallic when the number of nanoring unit cells (Figure 5.4) that determine the length of the tubes corresponds to $3\xi_z + 1$, where ξ_z can be any positive integer. Similarly, tube lengths corresponding to $3\xi_z + 2$ and $3\xi_z + 3$ appear to be semiconducting. This trend has been shown in Figure 5.4 for various lengths of the (13,13) armchair tube, that is examined in this study. The choice of (13,13) is somewhat arbitrary, as our primary goal is to examine general physics through a model solvated "particle-in-a-box". In this picture, the gap at the semiconducting lengths between the energy levels immediately above (LUMO) and below (HOMO) ε_F reduces gradually with the expansion in tube length. The trend

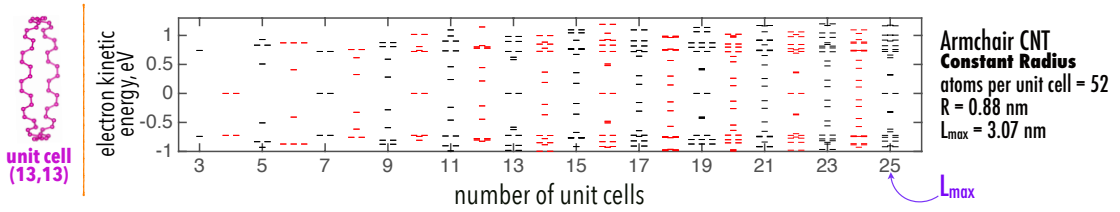

Figure 5.4: The energy levels of finite single walled armchair CNTs with constant radius derived via TB calculations. The x-axis represent various tube lengths via the number of armchairs nanoring unit cells (shown on the left) repeating in space (see *supporting information*). L_{max} denotes the maximum of tube length in the panel. The Fermi energy (ε_F) is referenced at 0 eV.

indicates a possible continuum with the LUMO along such lengths, associated with quantized sampling of the infinite length Brillouin zone, which we attempt to extract via our proposed voltammetry technique in later sections. Considering the alignment [133] of metal Fermi level with that of the model CNTs (which we assume to be halfway between HOMO and LUMO levels) at equilibrium, the validity of our proposed characterization technique is best demonstrated with such semiconducting nanotubes, as these structures are likely to remain charge neutral at zero overpotential.

5.3.2 Role of energetics on the current response

The transfer of an electron across a metal-electrolyte interface is an energy demanding process, which is more discernible at nanoscale dimensions. An electron receives the required energy mostly from the applied overpotential before successfully making the transition across an interface (see Figure 5.3). As discussed above, the makeup of this energy cost is usually categorized into Coulomb staircase charging for larger nanoparticles and molecular redox charging for smaller particles with molecular dimensions [128,129]. However, the correlation drawn in the previous sections between the energetics and the size of a reactant strongly suggests that the Coulomb repulsion potential (U) and the electron kinetic

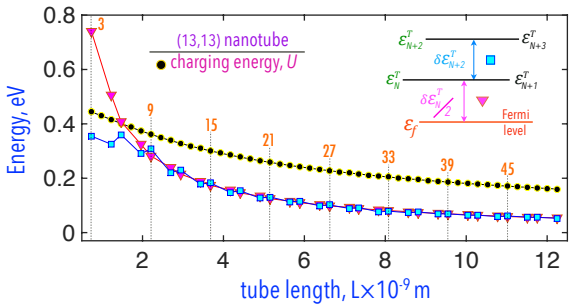

Figure 5.5: The charging energy U and the separations between the consecutive spin-degenerate acceptor levels with respect to ε_F (at $\eta = 0$) as a function of L for semiconducting armchair tubes only. These two energy components combine at all L to fix the final single-particle energy accessed by the electron during a redox event. The number of unit nanorings corresponding to the respective L are marked.

energy ($\delta\varepsilon^T$) needed to reach an allowed reactant acceptor state contribute simultaneously at any particle dimension to the cost of transferring an electron (in addition to the reorganization energy). In our model (13,13) nanotube "particle-in-a-box" system, this is further clarified in Figure 5.5, where U and $\delta\varepsilon^T$ are plotted in the context of reduction events as a function of their length L. The energy states for these CNTs (Figure 5.4) were assumed to be occupied up to the Fermi level at $\eta = 0$, which as mentioned before is assumed to lie in between the HOMO-LUMO gap[133] (Figure 5.1). Therefore, the first state in Figure 5.5, available right above the ε_F (pink profile) was considered to be the point of entry that can accommodate an electron. Similarly, the energy gap between the second and the first kinetic level above ε_F is shown by the blue profile.

The charging energy $U(L)$ shows a descending trend with increasing length (Figure 5.5 black profile), demonstrating magnitudes that are as significant as the electron kinetic energy cost. With less electron quantization at larger lengths, the electron kinetic energy cost $\delta\varepsilon_N^T$ accordingly decreases with length (also shown in Figure 5.5). Thus when a CNT's length is extended to the micron scale the value of U decreases to less than the thermal energy at room temperature, as does the the kinetic contribution to the separation $\delta\varepsilon_N^T$

between single-particle states. Under these conditions the predicted features would not be observed.

To determine the final energy requirement for any successful ET, U and $\delta\varepsilon_N^T$ must be added at all dimensions. Thus, when $\lambda \approx k_B\mathcal{T}$, the first transfer event would require the energy $[\varepsilon_N^T(L) - \varepsilon_{N-1}^T(L) + U(L)]/2 = (\delta\varepsilon_N^T + U(L))/2$ for a successful reduction (since ε_F sits in between HOMO and LUMO). The second transfer however would demand only $\varepsilon_{N+1}^T(L) - \varepsilon_N^T(L) + U(L) = \delta\varepsilon_{N+1}^T + U(L) = U(L)$ on account of the spin degeneracy of the acceptor level. Similarly, the third and fourth reduction event can be activated by supplying $\delta\varepsilon_{N+2}^T + U(L)$ and $U(L)$, respectively via the applied η. Each of these "particle-in-a-box" type transfer events are expected to appear as recognizable current peaks in a voltammogram. However, for systems with multiply degenerate orbitals/levels, voltammetric peaks beyond the first two are also likely to be separated by only U. In fact, the peak positions observed in the differential pulse voltammetry of Au nanoparticles strongly endorses this suggestion[130]. In general, we argue that the overpotentials corresponding to such current peaks hold the key to extract: (1) the charging energy (U); (2) the energy level structure (ε^T); and (3) the relationship between reactant level separations and the bulk energy dispersion of any continuously quantized system. The potential of the first current peak, which can represent the energy demand $(\delta\varepsilon_N^T + U(L))/2$ (see Figure 5.1), is a crucial determinant in extracting this information, as it is dependent on the λ (Figure 5.2) and the applied scan rate. In the following section, we thoroughly focus on this critical issue.

5.3.3 Extracting electronic structure information in the low reorganization energy limit

To explore the possibility of extracting $\delta\varepsilon^T$ and U information from voltammetric spectra, we performed voltammetric simulations with a cathodic (reduction) linear sweep scheme on a 15 unit cell (3.67 nm) long (13,13) armchair semiconducting tube under both

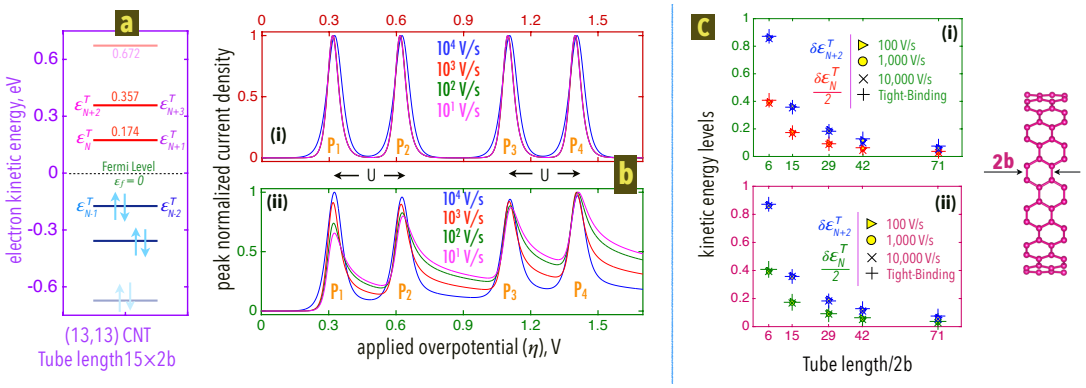

Figure 5.6: Normalized current density (j) profiles representing four cathodic ET events to (13,13) CNTs in System 1 (b[i]) and 2 (b[ii]) at different scan rates for $\lambda = k_B\mathcal{T}$. The electron kinetic energy level structure of the CNT unit (a) denotes the TB-derived levels participating in the heterogenous transfer process as suggested in Figure 5.1. By repeating these simulations with five different nanotube lengths (c) at different scan rates in System 1 (c[ii]) and 2 (c[i]) we calculated their first two kinetic energy levels (c) above ε_F. The energies show a good match with those obtained via TB calculations. The scan rate dependence is negligible at the assumed low λ scenario.

the diffusion-less monolayer bound configuration (System 1 in Figure 5.3) and the diffusion mediated free-floating configuration (System 2 in Figure 5.3). To begin with, we assumed that in both cases the redox-active CNTs are in equilibrium with the metal electrode such that their HOMO and LUMO level straddle ε_F.[133] The normalized current density obtained from the simulation of four ET events in the $\lambda = k_B\mathcal{T}$ limit, is shown in Figure 5.6b. It can be seen that the potentials corresponding to the positions of each of these peaks do not demonstrate any considerable dependence on the applied scan rate. In fact, the four peak potentials correlate well with the kinetic energy levels in Figure 5.6a. To understand this, let us analyze the voltammograms in Figure 5.6b(i,ii) for the two systems. Here, the calculated value of U from equation 5.8 is ~ 0.3 V (Figure 5.5) and $\delta\varepsilon_N^T = (0.174 \times 2)$ V (Figure 5.6a). Hence, the energy required to place an electron in the first acceptor level ε_N above ε_F should correspond to $(\varepsilon_N^T - \varepsilon_{N-1}^T + U)/2 = (\delta\varepsilon_N^T + U)/2 \approx 0.32$ V, when

$\lambda \to k_B\mathcal{T}$ (see Figure 5.1). To obtain U from an experiment, one may aim at the potential difference between the first two peaks P_1 and P_2 in Figure 5.6b, where P_2 corresponds to the transfer of the second electron to the same kinetic level in a reverse spin configuration. The overpotential needed to activate this transfer to the single-particle level ε_{N+1} (Figure 5.1) should in principle correspond to the charging cost U. The difference is captured very well in our simulation as the two peaks appear at $\eta_{P_1} \approx 0.32$ and $\eta_{P_2} \approx 0.62$ V respectively in both systems. This can pave the way to extract ε_N^T via $\eta_{P_1} - U/2$, which according to Figure 5.6b amounts to ~ 0.17 V, and is a good match to the value obtained from the TB calculation, shown in Figure 5.6a. With the first kinetic level identified, we can now extract the second electron kinetic level $\delta\varepsilon_{N+2}^T$ (Figure 5.6a) above $\delta\varepsilon_N^T$ using the third (η_{P_3}) and the fourth (η_{P_4}) peak potentials via $\delta\varepsilon_{N+2}^T = \eta_{P_3} - \eta_{P_2} - U$, where U can again be obtained by the difference $\eta_{P_4} - \eta_{P_3}$. Because of the spin degeneracy, we take $\delta\varepsilon_{N+1}^T = \delta\varepsilon_{N+3}^T = 0$.

Using this method, we calculated the first two electron kinetic energy levels for different lengths of (13,13) armchair nanotubes in both System 1 and 2. These electrochemically derived energy levels, as presented in Figure 5.6c for various scan rates, show good agreement with the corresponding TB-derived values. This formulation can be applied to experimentally obtained voltammograms to examine the molecular electronic level structure near the Fermi energy ε_F. The scan rate independence of the current profiles in Figure 5.6b that leads to this connection between the numerical and electrochemical energetics can largely be attributed to the assumed negligible λ value. While this assumption allows us to see the inherent connection that lies between the energetics of nanomaterials and the voltammetric observations associated with them, in reality a system may deviate considerably ($\lambda \gg k_B\mathcal{T}$) from this ideal situation. Therefore, it is very important for us to identify means by which U and $\delta\varepsilon^T$ might be extracted from voltammetric spectra when $\lambda \gg k_B\mathcal{T}$. To achieve this goal, we now aim at understanding the role of λ on the current profiles in

voltammetry.

5.3.4 Extracting electronic structure information in the large reorganization energy limit

The splitting of single-particle states via the Stokes shift parameter/ reorganization energy has been discussed in the context of Figure 5.2. In addition to this splitting, these levels broaden as well by λ via equations 5.6 and 5.7, which introduces a scan rate dependence into the resulting peak potentials as presented in Figure 5.7a. This does not occur in the limit of negligible λ (Figure 5.6b). Figure 5.2 suggests that the first reduction should occur at $\eta = (\delta\varepsilon_N^T + U)/2 + \lambda$, assuming that ε_F sits in between HOMO and LUMO.[133] The transferred electron converts the acceptor state into a reduced state, which via nuclear reorientation shifts 2λ below the original acceptor level (Figure 5.2). This splitting becomes negligible in the $\lambda \to k_B\mathcal{T}$ limit, as implied in Figure 5.1. The reorientation of the nuclei associated with this 2λ-shift *increases* the effective dielectric constant of the system from ϵ_∞ before nuclear reorganization, where the only contribution to the effective dielectric constant is the "infinitely fast" rearrangement of bound electrons, to the higher polarized solvent value ϵ_s. Thus the charing energy (U) contribution to the separation between sequential filled donor states, or conversely two sequential empty acceptor states, is dictated by ϵ_s as given by equation (5.8) and illustrated in Figure 5.7a. Whereas the charging energy contribution to the separation between the acceptor state of level ε_{N+1} and the donor state of level ε_N is given by $U_\infty = U + 2\lambda$ (also illustrated Figure 5.7a), which can also be obtained by setting $\epsilon_s = \epsilon_\infty$ in equation (5.8) in the classical limit.[1,4,60] Moving forward in this way, the third reduction can take place into a new kinetic energy level with further rise of η by $\delta\varepsilon_{N+2}^T + U$ (Figure 5.2).

Based on this formulation, the current response for $\lambda = 0.25$ eV is presented in Figure 5.7b for different scan rates. The plots show that the entire peak spectrum shifts uniformly

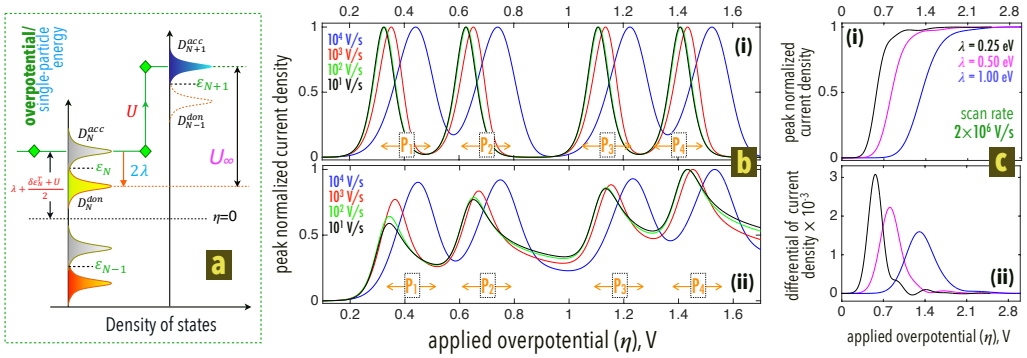

Figure 5.7: Normalized current density (j) profiles representing four ET to (13,13) CNTs in System 1 (b[i]) and 2 (b[ii]) at different scan rates for $\lambda = 0.25$ eV. Part (a) shows the energetics involved in the first two transfer events (based on Figure 5.2). The current spectra shifts with the scan rate, but the peak spacings consistently represent the electroactive energetics. The potentials of the first peaks do not correlate with $(\delta\varepsilon_N^T + U)/2 + \lambda$. To obtain this, we employ ultrafast scan rates (∼MV/s) which produces a plateaued current response (c[i]) due to suppressed interfacial kinetics. The peak potential of the derivative (c[ii]) of this current profile corresponds to $(\delta\varepsilon_N^T + U)/2 + \lambda$. Moreover, λ is extractable from these peaks via its standard deviation $(2\lambda k_B \mathcal{T})^{1/2}$.[1]

towards higher overpotential as the scan rate is increased. It preserves the expected features such as U, $\delta\varepsilon_{N+1}^T$ etc contained in the peak-to-peak separations (compare Figures 5.7b and 5.6b). However, it becomes challenging to utilize the first current peak ($P1$) to predict the first kinetic level via $\delta\varepsilon_N^T/2$, which is needed to build the energy level structure near ε_F. A possible remedy is to employ ultrafast scan rates (∼MV/s) in voltammetry that can identify[118] an effective acceptor level. In this regime, the interfacial kinetics are heavily suppressed as the time allowed for the redox processes is very limited. This causes the resulting current peaks to broaden towards infinity and gives rise to a plateaued current profile[14,118]. These current profiles are shown in Figure 5.7c[i] for various λ values. The half-maximum of such a plateauing current profile (or alternately, the peak of the derivative of this profile as in Figure 5.7c[ii]) represents the effective position of an electroactive single-particle state[118] via λ, which in the present case is expected to coincide with $(\delta\varepsilon_N^T + U)/2 +$

λ. The half-maximum of each current profile in Figure 5.7c[i] shows a very good match to the expected values. Moreover, the peak width pertaining to the derivative of this profile (Figure 5.7c[ii]) represents the reorganization energy[1] λ via its standard deviation $(2\lambda k_B \mathcal{T})^{1/2}$. These energetics can be coupled with those from Figure 5.7b to build the electronic structure of the investigated redox system. The required ultrafast scan rate to see such plateaued profiles is typically a function of the coupling $|M|$ of the interface[118]. The upper bound of the currently achievable scan rates lies in the range of MV/s[13,102] - which allows systems with $|M|$ up to 10^{-5} eV to be characterized via the ultrafast voltammetric methods[118].

The calculated electronic structure (as in Figure 5.4) and the corresponding peak spacings in a voltammetry measurement will likely be modified by the presence of functional groups on CNTs. In such cases, the proposed method may prove to be a promising spectroscopic technique to explore the impact of a functional group on the energy level configuration of pristine CNTs or any redox-active species in question. This can be achieved by comparing the multiple ET voltammograms of pristine and functionalized CNTs in an identical electrolyte. Such an examination of functional groups might open up new possibilities that include voltammetric characterization or "sensing" of functional groups.

It is also probably that unintentional defects, such as carbon vacancies in this model system, could introduce a variance in the voltammetric peak spacing when averaged over all possible defect sites across an ensemble of reactants. The impact of unintentional defects on the electronic structure should be pursued in future work, but based on similar results for graphene quantum dots[135] and fullerenes[132] we do not expect it to be a major limitation for the proposed technique.

5.3.5 Energy dispersion via voltammetry

From the above results, we can now see that the electron kinetic (ε^T) and Coulombic (U) information contained in voltammetry can be extracted for outer-sphere reactants of all length scales. This is revealed by a continuous increase in both contributions (as in Figure 5.5) with decreasing reactant size, which effectively connects Coulomb blockade electrochemistry with redox electrochemistry. This connection gives rise to a continuum in ET behaviour which represents changes in both ε^T and U (as well as λ) with system size. Though this physics is general, in our model CNT system the quantization trend in Figure 5.5 arises due finite size sampling of the infinite length CNT Brillouin zone (as in a "particle-in-a-box"). Thus a correlation can be made between the redox levels as a function of the system size and the bulk energy dispersion relation of the infinite system. To see this, let us explore how the extracted electron kinetic energy varies as a function of length L for our (13,13) armchair CNTs using LSV. This would require the identification of the lowest unoccupied level ε_N^T above ε_F (sitting between HOMO and LUMO level) using the first two peak potentials for a series of nanotube lengths.

For metallic lengths of these tubes ($3\xi_z + 1 = L/2b$ as shown in Figure 5.8), the lowest sub-band energy $\varepsilon^T = 0$ quantizes the infinite length Brillouin zone at one of the Dirac points $(0, \pm 2\pi/3b)$. Note, b is the spacing between two CNT atomic rows our model (13,13) unit cell direction (see Figure 5.6 and appendix). The lowest energy values for semiconducting tubes ($\varepsilon^T > 0$) however, quantizes the Brillouin zone at k points that lie before and after the Dirac point for tube lengths corresponding to $3\xi_z + 2 = L/2b$ and $3\xi_z + 3 = L/2b$, respectively. These minimum energies for different semiconducting lengths can be obtained by analyzing voltammetric peaks using the method suggested in Figure 5.7. The collected voltammetric energies can be correlated with the corresponding quantized k points via the $L/2b$ values of the tubes under investigation. The details of this evaluation

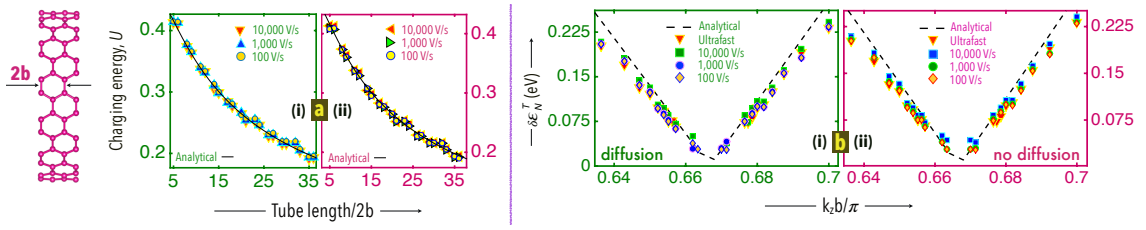

Figure 5.8: ε^T *vs* k relations (b) developed for (13,13) nanotube from the first two peaks in simulated voltammograms under both System 1(b[ii]) and 2 (b[i]). The values at different scan rates show good match with the analytical ε^T *vs* k dispersion. For both systems, the U extracted from simulated voltammograms (a) also agrees well with equation 5.8.

are included in the appendix. Repeating this process for a series of armchair tube lengths should provide a correlation between the bulk electron kinetic energy dispersion structure for a given (n_a, n_a) armchair nanotube and the finite length electronic structure.

This framework was implemented for various (13,13) semiconducting lengths up to 72 unit cells (∼17.6 nm) contained in both System 1 and 2. The resulting electronic structure dispersion is presented in Figure 5.8 along with the calculated U values as a function of L. The charging energies obtained by the difference between the first two peaks are in very good agreement with the U values calculated via equation 5.8. This comparison is shown in Figure 5.8a. Figure 5.8b presents the electron kinetic energy (ε^T) dispersions for the (13,13) tube in System 1 and 2. These electrochemically obtained data points show a slight mismatch with the analytical trend (black broken line) in both systems. This deviation can be attributed to abrupt boundary quantization at small lengths for the TB method utilized and will likely increase further in actual measurements of this nature, but the general physical principles of quantization remain regardless. For long tubes, the mismatch declines, causing the data points near the bulk Dirac point to correspond better with the analytical results. For short tubes and thus far from the bulk Dirac point, the numerical calculations show more pronounced boundary effects which is reflected via the deviation of electrochemically derived energies from the analytical profiles in Figure 5.8b.

These outcomes reveal the potential application of voltammetry for the general electronic characterization of solvated nanomaterials such as CNTs and its general connection to electronic structure theory. While the model CNT based system in our analysis captures the discussed underlying possibilities, the ubiquity in both quantization of electronic structure and the interaction during Coulomb charging should allow the vast range of nano and molecular materials to be analyzed via this proposed technique. A successful implementation relies upon the analysis and correlation of voltammetric spectra with the continuum of changes in $\delta\varepsilon^T$ and U from the Coulomb blockade to the redox charging regime, as well as understanding the role of reorganization and scan rates on measured single-particle energies and peak positions. It is also important to emphasize again that the assumed level filling sequence may not hold when the ε_F is situated between donor/acceptor levels (at $\eta = 0$), rather than a HOMO-LUMO gap as is assumed here.

5.4 Conclusion

To summarize, we have presented a general theoretical framework for characterizing the electronic structure of solvated species via voltammetry. This framework was presented in the context of a model solvated "particle-in-a-box" system participating in outer-sphere electron transfer reactions, consisting of a finite length armchair CNTs. The energy dependence of interfacial charge transfer as a function of size was shown to primarily arise from: (1) electron kinetic energy cost ($\delta\varepsilon^T$) of the model system; and (2) the single electron charging cost U obtained through a dimensionality relation; as well as (3) the reorganization energy λ. In voltammetric studies, these energies play a crucial role in determining the extent of separation between spectra peaks. The peak separations were formally related in this work to both electronic structure quantization ($\delta\varepsilon^T$) and the Coulomb charging cost

(U) for single electron transfer; which are typically understood [128–130] to be distinctly representative of the redox charging regime at molecular dimensions and the Coulomb charging regime at large nanoscale dimensions, respectively. However, this work argues that the two energies ($\delta\varepsilon^T$ and U) are quantitatively significant across all nano dimensions. The continuum of these contributions coupled with a Stoke's shift via nuclear reorganization, leads to a correlation between the nanomaterial electronic structure and voltammetric spectra, which should allow one to extract the electron kinetic level spacings ($\delta\varepsilon^T$) and the Coulomb charging energy (U) with respect to particle dimensionality. This opens up the possibility of the electronic structure characterization of solvated nanomaterials using voltammetry techniques. Given the prevalence of voltammetry across vast and diverse fields in chemistry, the suggested techniques could further establish voltammetry as a quantitative electronic structure characterization tool for solvated systems. Based on the wide accessibility of voltammetric techniques, the obtained electronic structure and its evolution in the presence of attached functional groups can be employed to study various outer-sphere applications such sensors, organic-radical devices (including batteries), and molecular electronics. [17,27,136,146,151] Lastly, our work draws parallels with solid-state Coulomb blockade spectroscopy in the shell-filling limit. [158,159] As a future venture, it would be interesting to make a deeper connection between steady-sate Coulomb blockade transport theory [151] and transient Coulomb blockade phenomena within voltammetry – which demands the use of a reactant's excitation spectra rather than the ground state scenario considered here. Future work should also explore the application of first-principles methods for solvated electronic structure prediction using this voltammetric approach, cognizant of the challenges posed by the system size and exchange-correlation errors. [162]

CHAPTER 6
Conclusion and future work

6.1 Conclusion

To conclude, this work has been dedicated to analyzing the connection between system energetics and electrochemical process variables *i.e.* applied scan rate in outer-sphere electron transfer regime. The aim was to understand the nature and characteristics of a voltammetric response that results from a typical faradaic processes at an interface.

To this end, the work began with an elaborate analysis of Marcus-Gerischer heterogenous rate picture. This picture suggests that the heterogenous rate constant initially increases with overpotential (η), only to become independent of it at high applied voltages ($|\eta| \gg 0$). The distribution of rate constants in energy depends on the probability density functions via reorganization energy λ. Here in this heterogenous limit unlike some homogenous cases, the Marcus inversion region at high overpotentials does not occur.

This rate constant picture as a function of applied η suggests that if the scan rate is slower than a given limit set by the coupling between metal and redox state, then the reaction is likely to be kinetically dominated – to such an extent that the majority of transfer events can take place at energies below the active redox level. By raising the scan rate, the electrochemistry was shown to be suppressed which leads to plateaued current profiles that emulate the effective Marcus-Gerischer rate constant distribution. From such a profile λ was extracted. Within this picture, the coupling strength $|M|$ between metal and a redox group via monolayer was also extracted by utilizing the amount of reactant

conversion at different scan rates. Calculations show a consistent pattern in the extent of conversion with applied scan rates.

In the ultrafast regime, non-faradaic transport demands attention as it can cause high charging current. This is closely connected to the extent of potential screening at a metal-liquid interface. Proper screening of interfacial potential was shown to be essential to conserve the energetic positions of electroactive states. This is achieved by drift and diffusion of supporting ions in electrolyte over time. On the one hand, the transport of ions screens the interface potential, while on the other hand it gives rise to the charging current that decays exponentially in time. In the simulation, both faradaic and charging currents were monitored, and the total current was only collected when the desired degree of screening (or a desired decay in the associated charging current) was obtained. The time to arrive at this point is largely determined by the diffusivity of supporting ions.

Simulation also predicted that the nature of charging current can vary with different extent of partial surface coverage by monolayers. Intuitively, lower surface coverage is expected to provide faster screening via facile population of supporting ions. However, computations in this work suggests that this may not always be the case. Results show that with higher surface coverage, the RC time constant of charging current during screening goes down with a pattern in time, as opposed to a consistent RC decay time constant calculated for more open surfaces. With the use of high diffusivity electrolyte such as aqueous solution of ionic compounds *e.g.* NaCl, KCl etc, calculations suggest that the charging current can decay to an acceptable range within the timescale of $\sim$1 to 3 nanoseconds per $\sim$ 0.01 V of overpotential step. This acceptable charging decay limit can allow the detection of characterizable faradaic response under scan rates as high as MV/s. Although the associated screening gets weaker along the applied overpotential, the deviation is considerable

only at high overpotentials, where it may not influence the determination of reorganization energy and coupling strength.

Finally, these findings were combined together in a voltammetric formulation to extract the key energetics *i.e.* electron-kinetic energy level ε^T, Coulomb charing energy U and reorganization energy λ of a solvated molecule or nanoparticle. The localized nature of a typical single-particle level in vacuum within a very narrow range of energy can produce scan rate independent current response under applied potential. However, in a solvated environment scan rate dependence is inevitable due to the broadening of single particle levels via λ. Simulation of successive electron transfer events showed that, this scan rate dependences can cause a uniform shift of the resulting current spectrum in overpotential, which importantly, can preserve the peak-to-peak separation energies.

Given the equilibrium electrochemical potential μ_{eq} of redox-active particle to be straddling HOMO and LUMO levels, and considering spin degeneracy of single-particle levels, each pair of current peaks from the beginning are calculated to be separated by the true U of the system. Similarly, the separation between two successive pairs give the energy difference between two successive single-particle states. While simulation predicts that the scan rate dependence of voltammogram does not violate these particular principles, it does pose a considerable challenge on correlating the very first peak to LUMO or HOMO levels with respect to μ_{eq}. Here the first peak could not be referenced against the zero overpotential due to shifts in its position with scan rates. To resolve this, the effective position of LUMO or HOMO were calculated to be identifiable via ultrafast scan rates on the basis of the method described in Chapter 3. By combining low and ultrafast scan rates in this way, the electronic structure of a model redox-active system was calculated. Repeating this method for various particle dimensions revealed the possibility of extracting the energy dispersion

of that redox-active particle system.

6.2 Future work

More sophisticated calculation and direct comparison to experiments. The present work was mainly focused on establishing the theoretical principles regarding a possible connection between system energetics and the associated voltammetric current. To validate the proposed model, an experimental voltammogram or the electronic structure/energetics derived from it need to be compared with known energetic contributions of a system. The evolution of current peaks toward the proposed plateaued response has already been observed[13,14] in monolayer mediated transport, while quantized charging was found to occur in many particle systems[128,132,133,135] over a range of dimensions. However, to the best of our knowledge, a direct connection is yet to be established between the redox-electrochemical response of a solvated particle systems and its energetics.

The calculations shown here were limited to exploring 1D systems only. Most experiments are likely to address nanoparticle systems beyond 1D dimension. If the current profiles in a voltammogram are the target of comparison, then before any electrochemical simulation, the initial electron-kinetic level structure of the target nanoparticle would best be resolved with atomistic calculation as opposed to the TB method utilized in this work. This can offer better accuracy and flexibility than those provided by the TB method, and in turn may increase the possibility towards a stronger correlation with experimental data.

The determination of reorganization energy of a given solvent or a redox-particle via first-principle methods can also be a matter of significant interest. While this can be challenging, recent reports have shown great possibilities in reorganization energy determination via DFT calculations.[166–168] Such results can be compared with that extracted from voltammetric experiments on the basis of the method suggested here. Similarly, one

may extract and compare the electron-kinetic levels and Coulomb charging energies as well. Any mismatch with its theoretical analogue can be further investigated for latent energetic contributions, possibly via the presence of unintentional elements and surface defects.

Detecting effects of functionalized groups on current response. In many cases, typical Carbon based structures in the form of nanotubes or as 2D sheet of graphene, or in caged configurations such as various fullerenes are functionalized with electron donating and/or accepting groups. These variations can modify the chemical characteristics of base matrix. The impact of such a functional groups, would likely be to change either the quantization or charging energy. Experimentally, by comparing a near pristine CNT ensemble electrochemical results with those that are intentionally functionalized one may be able to gauge the effect of such functional groups on the solvated electronic structure of CNTs. Such an examination of functional groups might open up new possibilities that include voltammetric characterization or "sensing" of functional groups.

Long range electron transfer. Finally, the calculations can be extended into double-contact molecular electronic systems. The work in this thesis mainly focused on single contact configurations. However, a redox active molecule can connect two metallic contacts via bridging monolayers. Here, the efficiency of electron transfer can largely be determined by electrochemical gating with the supporting ions in solution. These device systems can also be extended to include multiple redox-centers in series where an electron travels over a longer distance between two metal contacts. It could be interesting to check the role of such long range transfer events on the ultimate efficiency of faradaic current. In organic radical batteries, hopping is the understood mechanism of electron transport among redox centres within an electrolyte. Therefore a combined rate constant picture based on interfacial and hopping transfer would certainly be beneficial towards the design of novel device systems.

Bibliography

[1] Bard, A. J.; Faulkner, L. R. *Electrochemical Methods: Fundamentals and Applications*, 2nd ed.; John Wiley and Sons, Inc, 2001.

[2] Landau, L. Zur Theorie der Energieubertragung. II. *Phyz. Soviet Union* **1932**, *2*, 46–51.

[3] Zener, C. Dissociation of Excited Diatomic Molecules by External Perturbations. *Proc. Royal. Soc. London* **1933**, *A140*, 660–668.

[4] Schmickler, W.; Santos, E. *Interfacial Electrochemistry*, 2nd ed.; Springer, 2010.

[5] Miller, J. R.; Calcaterra, L. T.; Closs, G. L. Intramolecular Long-Distance Electron Transfer in Radical Anions. The Effects of Free Energy and Solvent on the Reaction Rates. *J. Am. Chem. Soc.* **1984**, *106*, 3047–3049.

[6] Kissinger, P. T.; Heineman, W. R. Cyclic voltammetry. *J. Chem. Educ.* **1983**, *60*, 702.

[7] Bevan, K. H.; Hossain, M. S.; Iqbal, A.; Wang, Z. Exploring Bridges between Quantum Transport and Electrochemistry. I. *J. Phys. Chem. C* **2016**, *120*, 179–187.

[8] Weber, K.; Creager, S. E. Voltammetry of Redox-Active Groups Irreversibly Adsorbed onto Electrodes. Treatment Using the Marcus Relation between Rate and Overpotential. *Anal. Chem.* **1994**, *66*, 3164–3172.

[9] Tender, L.; Carter, M. T.; Murray, R. W. Cyclic Voltammetric Analysis of Ferrocene Alkanethiol Monolayer Electrode Kinetics Based on Marcus Theory. *Anal. Chem.* **1994**, *66*, 3173–3181.

[10] Napper, A. M.; Liu, H.; Waldeck, D. H. The Nature of Electronic Coupling between Ferrocene and Gold through Alkanethiolate Monolayers on Electrodes: The Importance of Chain Composition, Interchain Coupling, and Quantum Interference. *J. Phys. Chem. B* **2001**, *105*, 7699–7707.

[11] Howell, J. O.; Wightman, R. M. Ultrafast Voltammetry and Voltammetry in Highly Resistive Solutions with Microvoltammetric Electrodes. *Anal. Chem.* **1984**, *56*, 524–529.

[12] Hung, M.-K.; Wang, Y.-H.; Lin, C.-H.; Lin, H.-C.; Lee, J.-T. Synthesis and Electrochemical Behaviour of Nitroxide Polymer Brush Thin-Film Electrodes for Organic Radical Batteries. *J. Mater. Chem.* **2012**, *22*, 1570–1577.

[13] Amatore, C.; Maisonhaute, E.; Schöllhorn, B.; Wadhawan, J. Ultrafast Voltammetry for Probing Interfacial Electron Transfer in Molecular Wires. *ChemPhysChem* **2007**, *8*, 1321–1329.

[14] Amatore, C.; Maisonhaute, E.; Nierengarten, J. F.; Schöllhorn, B. Direct Monitoring of Ultrafast Redox Commutation at the Nanosecond and Nanometer Scales by Ultrafast Voltammetry: From Molecular Wires to Cation Releasing Systems. *Israel J. Chem.* **2008**, *48*, 203–214.

[15] Madhiri, N.; Finklea, H. O. Potential-, pH-, and Isotope-Dependence of Proton-Coupled Electron Transfer of an Osmium Aquo Complex Attached to an Electrode. *Langmuir* **2006**, *22*, 10643–10651.

[16] Fortgang, P.; Amatore, C.; Maisonhaute, E.; Schöllhorn, B. Microchip for Ultrafast Voltammetry. *Electrochem. Commun.* **2010**, *12*, 897–900.

[17] Heath, J. R. Molecular Electronics. *Annu. Rev. Mater. Res.* **2009**, *39*, 1–23.

[18] Osorio, H. M.; Catarelli, S.; Cea, P.; Gluyas, J. B. G.; Hartl, F.; Higgins, S. J.; Leary, E.; Low, P. J.; Martín, S.; Nichols, R. J.; Tory, J.; Ulstrup, J.; Vezzoli, A.; Milan, D. C.; Zeng, Q. Electrochemical Single-Molecule Transistors with Optimized Gate Coupling. *J. Am. Chem. Soc.* **2015**, *137*, 14319–14328.

[19] Nakahara, K.; Oyaizu, K.; Nishide, H. Electrolyte Anion-Assisted Charge Transportation in Poly(oxoammonium Cation/Nitroxyl Radical) Redox Gels. *J. Mater. Chem.* **2012**, *22*, 13669–13673.

[20] Oyaizu, K.; Nishide, H. Radical Polymers for Organic Electronic Devices: A Radical Departure from Conjugated Polymers? *Adv. Mater.* **2009**, *21*, 2339–2344.

[21] Kim, J.-K.; Cheruvally, G.; Ahn, J.-H.; Seo, Y.-G.; Choi, D. S.; Lee, S.-H.; Song, C. E. Organic Radical Battery with PTMA Cathode: Effect of PTMA Content on Electrochemical Properties. *J. Ind. Eng. Chem.* **2008**, *14*, 371–376.

[22] Gao, X.-P.; Yang, H.-X. Multi-Electron Reaction Materials for High Energy Density Batteries. *Energy Environ. Sci.* **2010**, *3*, 174–189.

[23] Casado, N.; Hernández, G.; Sardon, H.; Mecerreyes, D. Current Trends in Redox Polymers for Energy and Medicine. *Prog. Polym. Sci.* **2016**, *52*, 107–135.

[24] Zhang, J.; Chi, Q.; Albrecht, T.; Kuznetsov, A. M.; Grubb, M.; Hansen, A. G.; Wackerbarth, H.; Welinder, A. C.; Ulstrup, J. Electrochemistry and Bioelectrochemistry Towards The Single-Molecule Level: Theoretical Notions and Systems. *Electrochim. Acta* **2005**, *50*, 3143–3159.

[25] Migliore, A.; Schiff, P.; Nitzan, A. On The Relationship between Molecular State and Single Electron Pictures in Simple Electrochemical Junctions. *Phys. Chem. Chem. Phys.* **2012**, *14*, 13746–13753.

[26] Blumberger, J.; Tateyama, Y.; Sprik, M. Ab Initio Molecular Dynamics Simulation of Redox Reactions in Solution. *Comput. Phys. Commun.* **2005**, *169*, 256–261.

[27] Hossain, M. S.; Iqbal, A.; Bevan, K. H. Interfacial Screening in Ultrafast Voltammetry: A Theoretical Study of Redox-Active Monolayers. *Anal. Chem.* **2016**, *88*, 9062–9070.

[28] Sun, Y.-P.; Fu, K.; Lin, Y.; Huang, W. Functionalized Carbon Nanotubes: Properties and Applications. *Acc. Chem. Res* **2002**, *35*, 1096–1104.

[29] Balasubramanian, K.; Burghard, M. Chemically Functionalized Carbon Nanotubes. *Small* **2005**, *1*, 180–192.

[30] Liu, D.; Zhu, W.; Trottier, J.; Gagnon, C.; Barray, F.; Guerfi, A.; Mauger, A.; Groult, H.; Julien, C. M.; Goodenough, J. B.; Zaghib, K. Spinel Materials for High-Voltage Cathodes in Li-Ion Batteries. *RSC Adv.* **2014**, *4*, 154–167.

[31] Zaghib, K.; Guerfi, A.; Hovington, P.; Vijh, A.; Trudeau, M.; Mauger, A.; Goodenough, J. B.; Julien, C. M. Review and Analysis of Nanostructured Olivine-Based Lithium Recheargeable Batteries: Status and Trends. *J. Power Sources* **2013**, *232*, 357–369.

[32] Huang, Q.; Cosimbescu, L.; Koech, P.; Choi, D.; Lemmon, J. P. Composite Organic Radicaleinorganic Hybrid Cathode for Lithium-Ion Batteries. *J. Power Sources* **2013**, *233*, 69–73.

[33] Huang, Q.; Choi, D.; Cosimbescu, L.; Lemmon, J. P. Multi-Electron Rdox Reaction of An Organic Radical Cathode Induced by A Mesopore Carbon Network with Nitroxide Polymers. *Phys. Chem. Chem. Phys.* **2013**, *15*, 20921–20928.

[34] Vlad, A.; Singh, N.; Rolland, J.; Melinte, S.; Ajayan, P. M.; Gohy, J. F. Hybrid Supercapacitor-Battery Materials for Fast Electrochemical Charge Storage. *Sci. Rep.* **2014**, *4*, 4315(1–7).

[35] Yamamoto, K.; Iriyama, Y.; Asaka, T.; Hirayama, T.; Fujita, H.; Fisher, C.; Nonaka, K.; Sugita, Y.; Ogumi, Z. Dynamic Visualization of the Electric Potential in an All-Solid-State Rechargeable Lithium Battery. *Angew. Chem. Int. Ed.* **2010**, *49*, 4414–4417.

[36] Butler, J. A. V. Studies in Heterogeneous Equilibria. Part II. - The kinetic Interpretation of the Nernst Theory of Electromotive Force. *Trans. Faraday Soc.* **1924**, *19*, 729–733.

[37] Erdey-Gruz, T.; Volmer, M. Zur Theorie der Wasserstoffüberspannung. *Z. Phys. Chem.* **1930**, *150(A)*, 203–213.

[38] Mohilner, D. M.; Delahay, P. Current-Potential Characteristics for Electrode Processes with Specific Adsorption of Reactant and/or Product. *J. Phys. Chem.* **1963**, *67*, 588–591.

[39] Erdey-Gruz, T. *Kinetics of Electrode Processes*; Wiley Interscience, New York, 1972.

[40] Bockris, J. O.; Reddy, A. K. N. *Modern Electrochemistry*; Plenum: New York, 1970.

[41] Fermi, E. *Nuclear Physics*; University of Chicago Press, Chicago., 1950.

[42] Marcus, R. A. On the Theory of OxidationReduction Reactions Involving Electron Transfer. I. *J. Chem. Phys.* **1956**, *24*, 966–978.

[43] Marcus, R. A. Electron Transfer at Electrodes and in Solution: Comparison of Theory and Experiment. *Electrochim. Acta* **1968**, *13*, 995–1004.

[44] Hush, N. S. Adiabatic Rate Processes at Electrodes. I. Energy–Charge Relationships. *J. Chem. Phys.* **1958**, *28*, 962–972.

[45] Hush, N. S. Homogeneous and heterogeneous optical and thermal electron transfer. *Electrochim. Acta* **1968**, *13*, 1005–1023.

[46] Chidsey, C. E. Free Energy and Temperature Dependence of Electron Transfer at the Metal-Electrolyte Interface. *Science* **1991**, *251*, 919–922.

[47] Levich, V. G. *Advances in Electrochemistry and Electrochemical Engineering*; New York: Interscience, 1966; Vol. 4; pp 249–371.

[48] Dogonadze, R. R. *Reactions of Molecules at Electrodes*; Wiley Inter science, New York, 1971; Chapter 3.

[49] Gerischer, H. Über den Ablauf von Redoxreaktionen an Metallen und an Halbleitern. I. Allgemeines zum Elektronenübergang Zwischen Einem Festkörper und einem Redoxelektrolyten. *Z. Physik Chem. N.F.* **1960**, *26*, 223–247.

[50] Gerischer, H. Über den Ablauf von Redoxreaktionen an Metallen und an Halbleitern. II. Metall-Elektroden. *Z. Physik. Chem. N.F.* **1960**, *26*, 325–338.

[51] Gerischer, H. Über den Ablauf von Redoxreaktionen an Metallen und an Halbleitern. III. Halbleiterelektroden. *Z. Physik. Chem. N.F.* **1961**, *27*, 48–79.

[52] Schmickler, W. *Interfacial Electrochemistry*, 1st ed.; Oxford University Press, New York, 1996.

[53] Gerischer, H. *Physical Chemistry: An Advanced Treatise*; H. Eyring, D. Hen derson, and W. Jost, Eds., Academic, New York, 1970; Vol. 9A.

[54] Papaconstantopoulos, D. A. *Handbook of the Band Structure of Elemental Solids*, 2nd ed.; Springer, 2015.

[55] Finklea, H. O.; Hanshew, D. D. Electron-Transfer Kinetics in Organized Thiol Monolayers with Attached Pentaammine(Pyridine)Ruthenium Redox Centers. *J. Am. Chem. Soc.* **1992**, *114*, 3173–3181.

[56] Finklea, H. O.; Liu, L.; Ravenscroft, M. S.; Punturi, S. Multiple Electron Tunneling Paths across Self-Assembled Monolayers of Alkanethiols with Attached Ruthenium(II/III) Redox Centers. *J. Phys. Chem.* **1996**, *100*, 18852–18858.

[57] Creager, S.; Yu, C. J.; Bamdad, C.; O'Connor, S.; MacLean, T.; Lam, E.; Chong, Y.; Olsen, G. T.; Luo, J.; Gozin, M.; et al., Electron Transfer at Electrodes through Conjugated "Molecular Wire" Bridges. *J. Am. Chem. Soc.* **1999**, *121*, 1059–1064.

[58] Ravenscroft, M. S.; Finklea, H. O. Kinetics of Electron Transfer to Attached Redox Centers on Gold Electrodes in Nonaqueous Electrolytes. *J. Phys. Chem.* **1994**, *98*, 3843–3850.

[59] Stähler, J.; Meyer, M.; Zhu, X. Y.; Bovensiepen, U.; Wolf, M. Dynamics of Electron Transfer at Polar Molecule–Metal Interfaces: The Role of Thermally Activated Tunnelling. *New J. Phys.* **2007**, *9*, 394–394.

[60] Marcus, R. A. Tutorial on Rate Constants and Reorganization Energies. *J. Electroanal. Chem.* **2000**, *483*, 2–6.

[61] Datta, S. *Quantum Transport: Atom to Transistor*; Cambridge University Press, 2005.

[62] Datta, S. *Electronic Transport in Mesoscopic Systems*; Cambridge University Press, 1997.

[63] Bevan, K. H.; Zahid, F.; Kienle, D.; Guo, H. First-Principles Analysis of the STM Image Heights of Styrene on Si(100). *Phys. Rev. B* **2007**, *76*, 045325(1–10).

[64] Datta, S. *Lessons from Nanoelectronics: A New Perspective on Transport*; World Scientific, 2012; Vol. 1.

[65] Amatore, C.; Maisonhaute, E.; Simonneau, G. Ultrafast Cyclic Voltammetry: Performing in the Few Megavolts per Second Range without Ohmic Drop. *Electrochem. Commun.* **2000**, *2*, 81–84.

[66] Nishide, H.; Oyaizu, K. Toward Flexible Batteries. *Science* **2008**, *319*, 737–738.

[67] Nishide, H.; Iwasa, S.; Pu, Y.-J.; Suga, T.; Nakahara, K.; Satoh, M. Organic Radical Battery: Nitroxide Polymers as A Cathode-Active Material. *Electrochim. Acta* **2004**, *50*, 827–831.

[68] Nakahara, K.; Oyaizu, K.; Nishide, H. Organic Radical Battery: Approaching Practical Use. *Chem. Lett.* **2011**, *40*, 222–227.

[69] Liang, Y.; Tao, Z.; Chen, J. Organic Electrode Materials for Rechargeable Lithium Batteries. *Abbreviation Title Adv. Energy Mater.* **2012**, *2*, 742–769.

[70] Tomlinson, E. P.; Hay, M. E.; Boudouris, B. W. Radical Polymers and Their Application to Organic Electronic Devices. *Macromolecules* **2014**, *47*, 6145–6158.

[71] Casalini, S.; Bortolotti, C. A.; Leonardi, F.; Biscarini, F. Self-Assembled Monolayers in Organic Electronics. *Chem. Soc. Rev.* **2017**, *46*, 40–71.

[72] Grieshaber, D.; MacKenzie, R.; Vörös, J.; Reimhult, E. Electrochemical Biosensors - Sensor Principles and Architectures. *Sensors* **2008**, *8*, 1400–1458.

[73] Gooding, J. J.; Mearns, F.; Yang, W.; Liu, J. Self-Assembled Monolayers into the 21st Century: Recent Advances and Applications. *Electroanalysis* **2003**, *15*, 81–96.

[74] Turyan, I.; Mandler, D. Self-Assembled Monolayers in Electroanalytical Chemistry: Application of Omega-Mercaptocarboxylic Acid Monolayers for Electrochemical Determination of Ultralow Levels of Cadmium (II). *Anal. Chem.* **1994**, *66*, 58–63.

[75] Eckermann, A. L.; Feld, D. J.; Shaw, J. A.; Meade, T. J. Electrochemistry of Redox-Active Self-Assembled Monolayers. *Coord. Chem. Rev.* **2010**, *254*, 1769–1802.

[76] Howell, J. O.; Wightman, R. M. Ultrafast Voltammetry of Anthracene and 9,l0-Diphenylanthracene. *J. Phys. Chem.* **1984**, *88*, 3915–3918.

[77] Gavaghan, D. J.; Bond, A. M. A Complete Numerical Simulation of The Techniques of Alternating Current Linear Sweep and Cyclic Voltammetry: Analysis of A Reversible Process by Conventional and Fast Fourier Transform Methods. *J. Electroanal. Chem.* **2000**, *480*, 133–149.

[78] Creager, S. E.; Wooster, T. T. A New Way of Using ac Voltammetry To Study Redox Kinetics in Electroactive Monolayers. *Anal. Chem.* **1998**, *70*, 4257–4263.

[79] Kiani, A.; Alpuche-Aviles, M. A.; Eggers, P. K.; Jones, M.; Gooding, J. J.; Paddon-Row, M. N.; Bard, A. J. Scanning Electrochemical Microscopy. 59. Effect of Defects and Structure on Electron Transfer through Self-Assembled Monolayers. *Langmuir*

2008, *24*, 2841–2849.

[80] Yamada, H.; Ogata, M.; Koike, T. Scanning Electrochemical Microscope Observation of Defects in a Hexadecanethiol Monolayer on Gold with Shear Force-Based TipSubstrate Positioning. *Langmuir* **2006**, *22*, 7923–7927.

[81] Finklea, H. O.; Ravenscroft, M. S.; Snider, D. A. Electrolyte and Temperature Effects on Long Range Electron Transfer Across Self-Assembled Monolayers. *Langmuir* **1993**, *9*, 223–227.

[82] Amatore, C.; Maisonhaute, E. When Voltammetry Reaches Nanoseconds. *Anal. Chem.* **2005**, *77*, 303 A–311 A.

[83] Nishide, H.; Suga, T. Organic Radical Battery. *Interface* **2005**, *14*, 32–38.

[84] Fortgang, P.; Maisonhaute, E.; Amatore, C.; Delavaux-Nicot, B.; Iehl, J.; Nierengarten, J. F. Molecular Motion Inside an Adsorbed [5:1] Fullerene Hexaadduct Observed by Ultrafast Cyclic Voltammetry. *Angew. Chem., Int. Ed.* **2011**, *50*, 2364–2367.

[85] Visions for a Molecular Future. *Nat. Nanotechnol.* **2013**, *8*, 385–389.

[86] Willner, I.; Heleg-Shabtai, V.; Blonder, R.; Katz, E.; Tao, G.; Bückmann, A. F.; Heller, A. Electrical Wiring of Glucose Oxidase by Reconstitution of FAD-Modified Monolayers Assembled onto Au-Electrodes. *J. Am. Chem. Soc.* **1996**, *118*, 10321–10322.

[87] Vericat, C.; Vela, M. E.; Benitez, G.; Carro, P.; Salvarezza, R. C. Self-Assembled Monolayers of Thiols and Dithiols on Gold: New Challenges for A Well-Known System. *Chem. Soc. Rev.* **2010**, *39*, 1805–1834.

[88] Marcus, R. A. Reorganization Free Energy for Electron Transfers at Liquid-Liquid and Dielectric Semiconductor-Liquid Interfaces. *J. Phys. Chem.* **1990**, *94*, 1050–1055.

[89] Marcus, R. A. Electron Transfer Reactions in Chemistry. Theory and Experiment. *Rev. Mod. Phys.* **1993**, *65*, 599–610.

[90] Barbara, P. F.; Meyer, T. J.; Ratner, M. A. Contemporary Issues in Electron Transfer Research. *J. Phys. Chem.* **1996**, *100*, 13148–13168.

[91] McMahon, D. P.; Troisi, A. Evaluation of the External Reorganization Energy of Polyacenes. *J. Phys. Chem. Lett.* **2010**, *1*, 941–946.

[92] Ghosh, S.; Horvath, S.; Soudackov, A. V.; Hammes-Schiffer, S. Electrochemical Solvent Reorganization Energies in the Framework of the Polarizable Continuum Model. *J. Chem. Theory Comput.* **2014**, *10*, 2091–2102.

[93] Kurnikov, I. V.; Zusman, L. D.; Kurnikova, M. G.; Farid, R. S.; Beratan, D. N. Structural Fluctuations, Spin, Reorganization Energy, and Tunneling Energy Control of Intramolecular Electron Transfer: The Surprising Case of Electron Transfer in a d8 - d8 Bimetallic System. *J. Am. Chem. Soc.* **1997**, *119*, 5690–5700.

[94] Vath, P.; Zimmt, M. B. A Spectroscopic Study of Solvent Reorganization Energy: Dependence on Temperature, Charge Transfer Distance, and the Type of SoluteSolvent Interactions. *J. Phys. Chem. A* **2000**, *104*, 2626–2633.

[95] Reynolds, L.; Gardecki, J. A.; Frankland, S. J. V.; Horng, M. L.; Maroncelli, M. Dipole Solvation in Nondipolar Solvents: Experimental Sudies of Reorganization Energies and Solvation Dynamics. *J. Phys. Chem.* **1996**, *100*, 10337–10354.

[96] Grampp, G.; Rauhut, G. Experimental and Theoretical Estimations of the Solvent Independence of the Electronic Coupling Matrix Element for an Organic Homogeneous Electron Self-Exchange Reaction. *J. Phys. Chem.* **1995**, *99*, 1815–1817.

[97] Bullock, J. P.; Mashkina, E.; Bond, A. M. Activation Parameters Derived From a Temperature Dependent Large Amplitude ac Voltammetric Study of the Electrode Kinetics of the Cp2M0/+ Redox Couples (M = Fe, Co) at a Glassy Carbon Electrode. *J. Phys. Chem. A* **2011**, *115*, 6493–6502.

[98] Costentin, C.; Louault, C.; Robert, M.; Roge, V.; Saveant, J. M. Reorganization Energy and Pre-Exponential Factor from Temperature-Dependent Experiments in Electron Transfer Reactions. A Typical Example: the Reduction of Tert-Nitrobutane. *Phys. Chem. Chem. Phys.* **2012**, *14*, 1581–1584.

[99] Finckh, P.; Heitele, H.; Volk, M.; Michel-Beyerle, M. E. Electron Donor/Acceptor Interaction and Reorganization Parameters from Temperature-Dependent Intramolecular Electron-Transfer Rates. *J. Phys. Chem.* **1988**, *92*, 6584–6590.

[100] Aoudia, M.; Guliaev, A. B.; Leontis, N. B.; Rodgers, M. A. J. Self-Assembled Complexes of Oligopeptides and Metalloporphyrins: Measurements of The Reorganization and Electronic Interaction Energies for Photoinduced Electron-Transfer Reactions. *Biophys. Chem.* **2000**, *83*, 121–140.

[101] Bergfield, J. P.; Ratner, M. A. Forty Years of Molecular Electronics: Non-Equilibrium Heat and Charge Transport at the Nanoscale. *Phys. Status Solidi B* **2013**, *250*, 2249–2266.

[102] Mallon, C.; Keyes, T. E.; Forster, R. J. Ultrafast Electrochemical Techniques. *Encyc. of Anal. Chem.* **2013**, 1–15.

[103] Amatore, C.; Maisonhaute, E.; Simonneau, G. Ohmic Drop Compensation in Cyclic Voltammetry at Scan Rates in the Megavolt per Second Range: Access to Nanometric Diffusion Layers via Transient Electrochemistry. *J. Electroanal. Chem.* **2000**, *486*, 141–155.

[104] Feynman, R. P. *QED: The Strange Theory of Light and Matter*; Princeton University Press, 2006.

[105] Heitele, H. Dynamic Solvent Effects on Electron-Transfer Reactions. *Angew. Chem. Int. Ed.* **1993**, *32*, 359–377.

[106] Robinson, D. B.; Chidsey, C. E. D. Submicrosecond Electron Transfer to Monolayer-Bound Redox Species on Gold Electrodes at Large Overpotentials. *J. Phys. Chem. B* **2002**, *106*, 10706–10713.

[107] Finklea, H. O.; Madhiri, N. Reorganization Energies of TEMPO/TEMPO+ in Water. *J. Electroanal. Chem.* **2008**, *621*, 129–133.

[108] Bond, A.; Fleischmann, M.; Robinson, J. Electrochemistry in Organic Solvents without Supporting Electrolyte Using Platinum Microelectrodes. *J. Elecanal. Chem. and*

Interfac. Electrochem. **1984**, *168*, 299 – 312.

[109] Heath, J. R.; Ratner, M. A. Molecular Electronics. *Physics Today* **2003**, *56*, 43–49.

[110] Bakker, E.; Telting-Diaz, M. Electrochemical Sensors. *Anal. Chem.* **2002**, *74*, 2781–2800.

[111] Paleček, E.; Tkáč, J.; Bartošík, M.; Bertók, T.; Ostatná, V.; Paleček, J. Electrochemistry of Nonconjugated Proteins and Glycoproteins. Toward Sensors for Biomedicine and Glycomics. *Chem. Rev.* **2015**, *115*, 2045–2108.

[112] Migliore, A.; Naaman, R.; Beratan, D. N. Sensing of Molecules Using Quantum Dynamics. *Proc. Natl. Acad. Sci.* **2015**, *112*, E2419–E2428.

[113] Miller, J. R.; Burke, A. F. Electrochemical Capacitors: Challenges and Opportunities for Real-World Applications. *Electrochem. Soc. Interface* **2008**, *17*, 53–57.

[114] Imada, Y.; Nakano, H.; Furukawa, K.; Kishi, R.; Nakano, M.; Maruyama, H.; Nakamoto, M.; Sekiguchi, A.; Ogawa, M.; Ohta, T.; Yamamoto, Y. Isolation of Hypervalent Group-16 Radicals and Their Application in Organic-Radical Batteries. *J. Am. Chem. Soc.* **2016**, *138*, 479–482.

[115] Zaghib, K.; Guerfi, A.; Hovington, P.; Vijh, A.; Trudeau, M.; Mauger, A.; Goodenough, J. B.; Julien, C. M. Review and Analysis of Nanostructured Olivine-Based Lithium Recheargeable Batteries: Status and Trends. *J. Power Sources* **2013**, *232*, 357–369.

[116] Léger, C.; Bertrand, P. Direct Electrochemistry of Redox Enzymes as a Tool for Mechanistic Studies. *Chem. Rev.* **2008**, *108*, 2379–2438.

[117] Migliore, A.; Nitzan, A. Irreversibility in Redox Molecular Conduction: Single Versus Double Metal-Molecule Interfaces. *Electrochim. Acta* **2015**, *160*, 363 – 375.

[118] Hossain, M. S.; Bevan, K. H. Exploring Bridges between Quantum Transport and Electrochemistry. II. A Theoretical Study of Redox-Active Monolayers. *J. Phys. Chem. C* **2016**, *120*, 188–194.

[119] Gummel, H. K. A Self-Consistent Iterative Scheme for One-Dimensional Steady State Transistor Calculations. *IEEE Trans. Electron Devices* **1964**, *11*, 455–465.

[120] Watkins, J. J.; White, H. S. The Role of the Electrical Double Layer and Ion Pairing on the Electrochemical Oxidation of Hexachloroiridate(III) at Pt Electrodes of Nanometer Dimensions. *Langmuir* **2004**, *20*, 5474–5483.

[121] Wang, H.; Pilon, L. Accurate Simulations of Electric Double Layer Capacitance of Ultramicroelectrodes. *J. Phys. Chem. C* **2011**, *115*, 16711–16719.

[122] He, R.; Chen, S.; Yang, F.; ; Wu, B. Dynamic Diffuse Double-Layer Model for the Electrochemistry of Nanometer-Sized Electrodes. *J. Phys. Chem. B* **2006**, *110*, 3262–3270.

[123] Janek, R. P.; Fawcett, W. R.; Ulman, A. Impedance Spectroscopy of Self-Assembled Monolayers on Au(111): Evidence for Complex Double-Layer Structure in Aqueous NaClO4 at the Potential of Zero Charge. *J. Phys. Chem. B* **1997**, *101*, 8550–8558.

[124] Creager, S. E.; Rowe, G. K. Solvent and Double-Layer Effects on Redox Reactions in Self-Assembled Monolayers of Ferrocenyl—Alkanethiolates on Gold. *J. Electroanal.*

Chem. **1997**, *420*, 291–299.

[125] Courant, R.; Friedrichs, K.; Lewy, H. On the Partial Difference Equations of Mathematical Physics. *IBM J. Res. Dev* **1967**, *11*, 215–234.

[126] Marcus, R. A. Chemical and Electrochemical Electron-Transfer Theory. *Annu. Rev. Phys. Chem* **1964**, *15*, 155–196.

[127] Honeychurch, M. J. Effect of Electron-Transfer Rate and Reorganization Energy on the Cyclic Voltammetric Response of Redox Adsorbates. *Langmuir* **1999**, *15*, 5158–5163.

[128] Chen, S.; Ingram, R. S.; Hostetler, M. J.; Pietron, J. J.; Murray, R. W.; Schaaff, T. G.; Khoury, J. T.; Alvarez, M. M.; Whetten, R. L. Gold Nanoelectrodes of Varied Size: Transition to Molecule-Like Charging. *Science* **1998**, *280*, 2098–2101.

[129] Chen, S.; Murray, R. W.; Feldberg, S. W. Quantized Capacitance Charging of Monolayer-Protected Au Clusters. *J. Phys. Chem. B* **1998**, *102*, 9898–9907.

[130] Quinn, B. M.; Liljeroth, P.; Ruiz, V.; Laaksonen, T.; Kontturi, K. Electrochemical Resolution of 15 Oxidation States for Monolayer Protected Gold Nanoparticles. *J. Am. Chem. Soc.* **2003**, *125*, 6644–6645.

[131] Hicks, J. F.; Miles, D. T.; Murray, R. W. Quantized Double-Layer Charging of Highly Monodisperse Metal Nanoparticles. *J. Am. Chem. Soc.* **2002**, *124*, 13322–13328.

[132] Xie, Q.; Perez-Cordero, E.; Echegoyen, L. Electrochemical Detection of C606- and C706-: Enhanced Stability of Fullerides in Solution. *J. Am. Chem. Soc.* **1992**, *114*, 3978–3980.

[133] Xie, Q.; Arias, F.; Echegoyen, L. Electrochemically-Reversible, Single-Electron Oxidation of C60 and C70. *J. Am. Chem. Soc.* **1993**, *115*, 9818–9819.

[134] Echegoyen, L.; Echegoyen, L. E. Electrochemistry of Fullerenes and Their Derivatives. *Acc. Chem. Res* **1998**, *31*, 593–601.

[135] Shinde, D. B.; Pillai, V. K. Electrochemical Resolution of Multiple Redox Events for Graphene Quantum Dots. *Angew. Chem. Int. Ed.* **2013**, *52*, 2482–2485.

[136] Ingole, P. P.; Markad, G. B.; Saraf, D.; Tatikondewar, L.; Nene, O.; Kshirsagar, A.; Haram, S. K. Band Gap Bowing at Nanoscale: Investigation of CdSxSe1–x Alloy Quantum Dots through Cyclic Voltammetry and Density Functional Theory. *J. Phys. Chem. C* **2013**, *117*, 7376–7383.

[137] Ingram, R. S.; Hostetler, M. J.; Murray, R. W.; Schaaff, T. G.; Khoury, J. T.; Whetten, R. L.; Bigioni, T. P.; Guthrie, D. K.; First, P. N. 28 kDa Alkanethiolate-Protected Au Clusters Give Analogous Solution Electrochemistry and STM Coulomb Staircases. *J. Am. Chem. Soc.* **1997**, *119*, 9279–9280.

[138] Guo, L.; Leobandung, E.; Chou, S. Y. A Silicon Single-Electron Transistor Memory Operating at Room Temperature. *Science* **1997**, *275*, 649–651.

[139] Fan, F.-R. F.; Bard, A. J. An Electrochemical Coulomb Staircase: Detection of Single Electron-Transfer Events at Nanometer Electrodes. *Science* **1997**, *277*, 1791.

[140] Musumeci, C.; Liscio, A.; Palermo, V.; Samorì, P. Electronic Characterization of Supramolecular Materials at the Nanoscale by Conductive Atomic Force And Kelvin

Probe Force Microscopies. *Mater. Today* **2014**, *17*, 504–517.

[141] Ellis, J. L.; Hickstein, D. D.; Xiong, W.; Dollar, F.; Palm, B. B.; Keister, K. E.; Dorney, K. M.; Ding, C.; Fan, T.; Wilker, M. B.; et. al., Materials Properties and Solvated Electron Dynamics of Isolated Nanoparticles and Nanodroplets Probed with Ultrafast Extreme Ultraviolet Beams. *J. Phys. Chem. Lett.* **2016**, *7*, 609–615.

[142] Damascelli, A. Probing the Electronic Structure of Complex Systems by ARPES. *Phys. Scr.* **2004**, *T109*, 61–74.

[143] Santra, B.; Shneider, M. N.; Car, R. In situ Characterization of Nanoparticles Using Rayleigh Scattering. *Sci. Rep.* **2017**, *7*, 40230.

[144] Brown, M. A.; Seidel, R.; Thurmer, S.; Faubel, M.; Hemminger, J. C.; van Bokhoven, J. A.; Winter, B.; Sterrer, M. Electronic Structure of Sub-10 nm Colloidal Silica Nanoparticles Measured by In-situ Photoelectron Spectroscopy at the Aqueous-Solid Interface. *Phys. Chem. Chem. Phys.* **2011**, *13*, 12720–12723.

[145] Zabet-Khosousi, A.; Dhirani, A. A. Charge Transport in Nanoparticle Assemblies. *Chem. Rev.* **2008**, *108*, 4072–4124.

[146] Bueno, P. R.; Feliciano, G. T.; Davis, J. J. Capacitance Spectroscopy and Density Functional Theory. *Phys. Chem. Chem. Phys.* **2015**, *17*, 9375.

[147] Evans, D. H. One-Electron and Two-Electron Transfers in Electrochemistry and Homogeneous Solution Reactions. *Chem. Rev.* **2008**, *108*, 2113–2144.

[148] Ellis, J. L.; Hickstein, D. D.; Schnitzenbaumer, K. J.; Wilker, M. B.; Palm, B. B.; Jimenez, J. L.; Dukovic, G.; Kapteyn, H. C.; Murnane, M. M.; Xiong, W. Solvents Effects on Charge Transfer from Quantum Dots. *J. Am. Chem. Soc.* **2015**, *137*, 3759–3762.

[149] Shakourian-Fard, M.; Kamath, G.; Sankaranarayanan, S. K. R. S. Electronic Structure Insights into the Solvation of Magnesium Ions with Cyclic and Acyclic Carbonates. *ChemPhysChem* **2015**, *16*, 3607–3617.

[150] Szabo, A.; Ostlund, N. S. *Modern Quantum Chemistry: Introduction to Advanced Electronic Structure Theory*, 1st ed.; Dover Publications, 1996.

[151] Muralidharan, B.; Ghosh, A. W.; Pati, S. K.; Datta, S. Theory of High Bias Coulomb Blockade in Ultrashort Molecules. *IEEE Trans. Nanotechnol.* **2007**, *6*, 536–544.

[152] Hopfield, J. J. Electron Transfer Between Biological Molecules by Thermally Activated Tunneling. *Proc. Natl. Acad. Sci.* **1974**, *71*, 3640–3644.

[153] Redi, M.; Hopfield, J. J. Theory of Thermal and Photoassisted Electron Tunneling. *J. Chem. Phys.* **1980**, *72*, 6651–6660.

[154] Bevan, K. H. Electron Transfer from the Perspective of Electron Transmission: Biased Non-Adiabatic Intermolecular Reactions in the Single-Particle Picture. *J. Chem. Phys.* **2017**, *146*, 134106.

[155] Nitzan, A. A Relationship between Electron-Transfer Rates and Molecular Conduction. *J. Phys. Chem. A* **2001**, *105*, 2677–2679.

[156] Memming, R. *Semiconductor Electrochemistry*, 1st ed.; WILEY-VCH Verlag, 2007.

[157] Pietron, J. J.; Hicks, J. F.; Murray, R. W. Using Electrons Stored on Quantized Capacitors in Electron Transfer Reactions. *J. Am. Chem. Soc.* **1999**, *121*, 5565–5570.

[158] Bakkers, E. P. A. M.; Hens, Z.; Zunger, A.; Franceschetti, A.; Kouwenhoven, L. P.; Gurevich, L.; Vanmaekelbergh, D. Shell-Tunneling Spectroscopy of the Single-Particle Energy Levels of Insulating Quantum Dots. *Nano Letters* **2001**, *1*, 551–556.

[159] Miller, O. D.; Muralidharan, B.; Kapur, N.; Ghosh, A. W. Rectification by Charging: Contact-Induced Current Asymmetry in Molecular Conductors. *Phys. Rev. B* **2008**, *77*, 125427.

[160] Nakada, K.; Fujita, M.; Dresselhaus, G.; Dresselhaus, M. S. Edge State in Graphene Ribbons: Nanometer Size Effect and Edge Shape Dependence. *Phys. Rev. B* **1996**, *54*, 17954–17961.

[161] Michaud-Rioux, V.; Zhang, L.; Guo, H. RESCU: A Real Space Electronic Structure Method. *J. Comput. Phys.* **2016**, *307*, 593–613.

[162] Cohen, A. J.; Mori-Sanchez, P.; Yang, W. Insights into Current Limitations of Density Functional Theory. *Science* **2008**, *321*, 792–794.

[163] Johnson, E. R.; Otero-de-la Roza, A.; Dale, S. G. Extreme Density-Driven Delocalization Error for a Model Solvated-Electron System. *J. Chem. Phys.* **2013**, *139*, 184116.

[164] Dickinson, E. J. F.; Limon-Petersen, J. G.; Rees, N. V.; Compton, R. G. How Much Supporting Electrolyte Is Required to Make a Cyclic Voltammetry Experiment Quantitatively "Diffusional"? A Theoretical and Experimental Investigation. *J. Phys. Chem. C* **2009**, *113*, 11157–11171.

[165] Rochefort, A.; Salahub, D. R.; Avouris, P. Effects of Finite Length on the Electronic Structure of Carbon Nanotubes. *J. Phys. Chem. B* **1999**, *103*, 641–646.

[166] Ren, H.-S.; Ming, M.-J.; Ma, J.-Y.; Li, X.-Y. Theoretical Calculation of Reorganization Energy for Electron Self-Exchange Reaction by Constrained Density Functional Theory and Constrained Equilibrium Thermodynamics. *J. Phys. Chem. A* **2013**, *117*, 8017–8025.

[167] Buda, M. On Calculating Reorganization Energies for Electrochemical Reactions Using Density Functional Theory and Continuum Solvation Models. *Electrochim. Acta* **2013**, *113*, 536–549.

[168] Senevirathna, W.; Daddario, C. M.; Sauve, G. Density Functional Theory Study Predicts Low Reorganization Energies for Azadipyrromethene-Based Metal Complexes. *J. Phys. Chem. Lett.* **2014**, *5*, 935–941.

Appendix

Calculation of molecular structure of Carbon nanotubes

A1 Kinetic energy levels ($\delta\varepsilon^T$) of model armchair CNT system.

The CNT unit cell was defined by a single column of carbon atoms arranged in an armchair configuration connected periodically at the ends. This configuration is illustrated in Figure A1 as ribbons by the the pink box, which become an armchair nanoring when periodic boundary conditions are enforced. This unit nanoring cell, which can be repeated in space to generate a nanotube, was represented by a matrix α in the calculation. The interaction between the neighbouring unit rings in a tube was captured via the coupling matrix β_a. These two matrices, as shown in Figure A1 were used to build the hamiltonian H for a finite armchair CNT whose kinetic eigenvalues, obtained via solving Schrodinger's equation

$$\varepsilon^T\psi = H\psi \tag{A1}$$

serve as the corresponding kinetic energy levels of that particular system. Here, $\varepsilon^T = \{\varepsilon_1^T, \varepsilon_2^T, ..., \varepsilon_N^T, \varepsilon_{N-1}^T, \varepsilon_{N+1}^T, ..., \varepsilon_{\mathcal{N}}^T\}$ has all the kinetic energies and ψ contains the corresponding wavefunctions. The total number of carbon atoms in a finite tube is $\mathcal{N}$ such that H is an $\mathcal{N} \times \mathcal{N}$ matrix. This gives us the kinetic energy level structure of a CNT that contains critical information, which contributes to the position of the current peaks during voltammetric characterization. We note, that although the tight-binding (TB) method is not self-consistent by nature, implementation of a first-principles self-consistent method to solve the large CNTs considered in this work would require a significant amount of computational resources. Moreover, we intend to demonstrate a general connection between the voltammetric output and the particle energetics, for which the inherent degree of accuracy

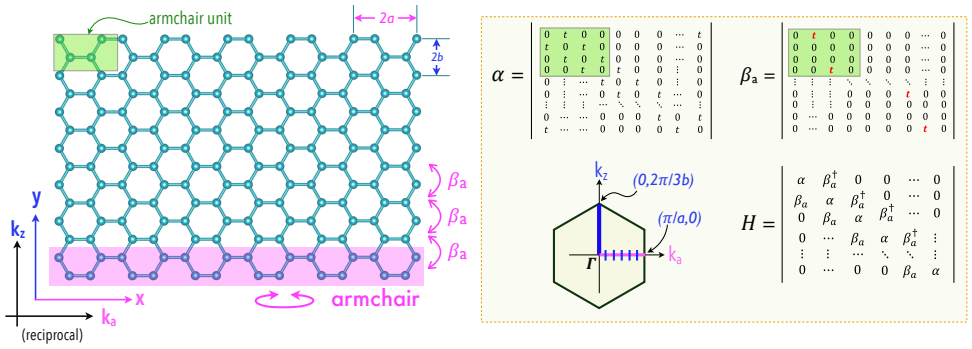

Figure A1: A sheet of Graphene, which can be rolled up along the x-direction to form an armchair nanotube. The green box encloses the smallest repeatable unit required to construct these nanotubes, where $a = 2.13$ Å, $b = 1.229$ Å. The unit cell in the form of a nanoring can be shaped by periodically connecting the armchair ribbon unit shown in the pink box. This nanoring builds the unit cell matrix for the tight-binding calculations. To form a nanotube, the nanoring is repeated along the y direction, which requires the neighboring unit rings to be connected via a coupling matrix. This coupling matrix β_a and the unit nanoring matrix α representing an armchair tube are shown on the right. These matrices form the system Hamiltonian H. The interaction energy t was assumed to be -3.0 eV. The Brillouin zone on the right indicates sampled allowed values in the armchair (k_a) direction for finite nanotube dimensions.

of the TB method should suffice. The energy levels, representing a finite system are in principle a quantized subset of the energies obtained for the same tube of infinite length. This parent set forms the energy dispersion along the tube length with a fixed radius, which can be achieved via the general expression

$$\varepsilon^T(k) = \alpha + \beta e^{ikp} + \beta^\dagger e^{-ikp} \tag{A2}$$

where $p = 2b$ is the spacing between neighbouring armchair unit cells, as shown in Figure A1. The wave vector is given by k such that for an armchair tube $k \equiv k_z = n_z/N_z p$ where $n_z = 0, 1, 2, ..., N_z$; N_z being the number of armchair unit cells (rings) repeating along the k_z direction. Beside the infinite case, equation A2 was used to examine the finite cases as well by restricting N_z in accordance with the dimensions of the respective finite systems.

This allows us to compare the analytical results with the discrete energy eigenvalues obtained via equation A1, which is discussed in detail in the next section.

A2 Comparing electronic structures: analytical vs numerical.

Beside the numerical calculations via the TB method, we utilized equation A2 (above) to extract the electron kinetic energy dispersions for both infinite and finite nanotubes. This allows us to compare the energy levels obtained via the TB method with analytical solutions obtained via quantization of the Brillouin zone (BZ). The first comparison is presented in Figure A2 for the model (13,13) armchair nanotube. The dispersions in part (a) show that the allowed energies obtained through analytical quantization of the BZ at three different finite tube lengths (L = [14 15 16] $\times$ 2b) are all subsets of the energy continuum generated by the infinite (13,13) nanotube. Two of these finite tubes are semiconducting [14 (red) and 15 (blue) unit cells] while the third one (16 unit cells) is metallic.

Since the states near the Fermi level ε_F are of the greatest interest with respect to electrochemical spectra, we isolate the dispersions for the 15 (semiconducting) and 16 (metallic) unit cell long tubes and compare the respective electronic structures near ε_F with those produced via the TB method for identical armchair geometries. Part (b) of Figure A2 shows this contrast for the 15 unit cell long tube where we see a close match between the energies derived analytically (b[i]) and numerically (b[ii]). A similar outcome follows with the 16 unit long, metallic tube in Figure A2(c), where the analytical (c[i]) and numerical (c[ii]) results display a satisfactory match. The slight mismatch here arises from the boundary condition imposed on electrons by finite CNTs. This imbalance, as shown in Chapter 5, translate into the electrochemically extracted energy dispersion profiles (see Figure 5.8b). This picture suggests that the TB derived electron kinetic energies for the

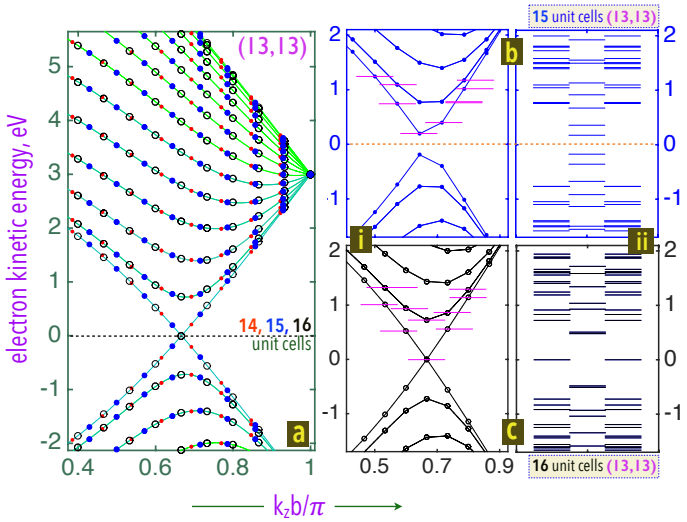

Figure A2: Comparison between the analytically and numerically derived energy states for armchair nanotubes. equation 9 was implemented for 14,15,16 unit cells and infinitely long (13,13) tubes generating the dispersions in part (a). The sampled, allowed values for a semiconducting (15 unit cells long) and a metallic (16 unit cells long) tube were isolated in part (b[i]) and (c[i]) respectively. The allowed states here, highlighted with red lines were compared with the respective TB derived energy levels in part (b[ii]) and (c[ii]) for the same geometries.

finite armchair tube lengths are likely to be quantized constituents of the continuous electron kinetic energy spectrum of an infinitely long nanotube.

A3 Reversal of electronic structure in finite nanotubes.

Typically infinite armchair tubes appear to be metallic at all tube lengths. However, finite tubes are predicted in Figure 5.4 to be of mixed semiconducting and metallic characters. This shift in armchair CNT's electronic structure for finite tubes can be attributed to the quantization of the 2D Brillouin zone of the CNTs along both the armchair (k_a) and zigzag (k_z) directions (Figure A1). To understand this, let us consider armchair nanotubes with a constant radius. On the one hand, the fixed number of armchair units (shown in

the green box in Figure A1) within the unit nano-ring cell specifies the number and positions of the allowed k values along the k_a direction in the BZ. These allowed values can be obtained via $k_a = \xi_a(2\pi/2an_a)$, where ξ_a is an integer, n_a is the armchair chiral index as in (n_a, n_a). One of these allowed points always conform with the $\Gamma(0,0)$ point irrespective of the assumed tube radius and thus passes through the Dirac point $(0,2\pi/3b)$ in the BZ. The allowed k values in the k_z direction on the other hand, are determined by the tube length which is a variable in this analysis and depends on the number of unit armchair nanorings. The neighboring rings in the tube are spaced by the unit vector of length $2b$ along the y (zigzag) direction, which gives the corresponding allowed values via $k_z = \xi_z(2\pi/2bn_z)$. Here, ξ_z is the integer defined above, n_z is the zigzag chiral index utilized in this context to specify the length of the armchair nanotube. Just as before, one of these allowed values through $\{\xi_z\}$ conforms with the Dirac point when $|n_z|/3 \equiv (\xi_z - 1)/3 = 1$. Lengths that satisfy this condition display metallic property, otherwise the nanotube is semiconducting. This interpretation compliments the results shown in Figure 5.4 for finite armchair tubes.

A4 Extraction of energy dispersion

As highlighted in the manuscript, the extraction requires the identification of the lowest unoccupied level ε_N^T above ε_F using the first two peak potentials for a series of nanotube lengths. A change in the length of the (13,13) nanotube would correspond to a change in the number of allowed k points along the k_z direction via $k_z = n_z L = n_z\pi/2bN_z$, where $2b$ is the distance between the neighbouring armchair nanoring units (Figure 5.8). For a given length to be metallic, one of the allowed values must coincide with the Dirac point at $k_z = 2\pi/3b$, which requires satisfying the condition $n_z/N_z = 4/3$. At this point $(0, 2\pi/3b)$, the subband energy is going to be zero. In the context of the nano-ring based unit cell representation, we already established that a metallic tube will consist of unit

rings, where ξ_z is an integer. For example, when the number of unit cells in (13,13) CNTs are 4, 7, 10, 13, ... etc., then $\varepsilon^T(2\pi/3b) = 0$ and the tubes will be metallic. Thus, tubes with L corresponding to $3\xi_z + 2$ and $3\xi_z + 3$are semiconducting. Since The k values for the semiconducting lengths do not coincide with the Dirac point, the lowest energy above $\varepsilon^T = 0$ can be expected to lie at the k points immediately neighboring the Dirac point. This neighboring k point lies above $k_z = 2\pi/3b$ for $L/2b = 3\xi_z+2$ and below $k_z = 2\pi/3b$ for $L/2b = 3\xi_z+3$. Hence the immediately neighboring k values corresponding to the minimum energies for $L/2b$ = 5, 8, 11, 14, ... etc occur at $k_z = 3\pi/4b, 5\pi/7b, 7\pi/10b, 9\pi/13b, ...$ etc respectively, all of which lie on the right-hand side of the Dirac point . Similarly, for etc. the minimum energy should appear at etc respectively, which lies on the left of $2\pi/3b$. The minimum energies were collected via voltammetric simulations based on methods discussed in Chapter 5 and then matched with the corresponding k points immediately neighboring the Dirac point.